Rational Design of Graphene-Based Architectures for High-Performance Lithium-Ion Battery Anodes

by

Huan Wang

B.S., Beijing University of Chemical Technology, 2008
M.S., Beijing University of Chemical Technology, 2011

AN ABSTRACT OF A DISSERTATION

submitted in partial fulfillment of the requirements for the degree

DOCTOR OF PHILOSOPHY

Department of Chemical Engineering
College of Engineering

KANSAS STATE UNIVERSITY
Manhattan, Kansas

2018

Abstract

Advances in synthesis and processing of nanocarbon materials, particularly graphene, have presented the opportunity to design novel Li-ion battery (LIB) anode materials that can meet the power requirements of next-generation power devices. This thesis presents three studies on electrochemical behavior of three-dimensional (3D) nanostructured anode materials formed by pure graphene sheets and graphene sheets coupled with conversion active materials (metal oxides). In the first project, a microgel-templated approach for fabrication of 3D macro/mesoporous reduced graphene oxide (RGO) anode is discussed. The mesoporous 3D structure provides a large specific surface area, while the macropores also shorten the transport length of Li ions. The second project involves the use of a novel magnetic field-induced method for fabrication of wrinkled Fe_3O_4@RGO anode materials. The applied magnetic field improves the interfacial contact between the anode and current collector and increases the stacking density of the active material. The magnetic field treatment facilitates the kinetics of Li ions and electrons and improves electrode durability and the surface area of the active material. In the third project, poly (methacrylic acid) (PMAA)-induced self-assembly process was used to design super-mesoporous Fe_3O_4@RGO anode materials and their electrochemical performance as anode materials is also investigated. To establish correlations between electrode properties (morphological and chemical) and LIB performance, a variety of techniques were used to characterize the samples. The significant improvement in LIB performance of the 3D anodes mentioned above is largely attributed to the unique properties of graphene and the resulting 3D architecture.

Rational Design of Graphene-Based Architectures for High-Performance Lithium-Ion Battery Anodes

by

Huan Wang

B.S., Beijing University of Chemical Technology, 2008
M.S., Beijing University of Chemical Technology, 2011

A DISSERTATION

submitted in partial fulfillment of the requirements for the degree

DOCTOR OF PHILOSOPHY

Department of Chemical Engineering
College of Engineering

KANSAS STATE UNIVERSITY
Manhattan, Kansas

2018

Approved by:

Major Professor
Placidus B. Amama

Copyright

Abstract

Advances in synthesis and processing of nanocarbon materials, particularly graphene, have presented the opportunity to design novel Li-ion battery (LIB) anode materials that can meet the power requirements of next-generation power devices. This thesis presents three studies on electrochemical behavior of three-dimensional (3D) nanostructured anode materials formed by pure graphene sheets and graphene sheets coupled with conversion active materials (metal oxides). In the first project, a microgel-templated approach for fabrication of 3D macro/mesoporous reduced graphene oxide (RGO) anode is discussed. The mesoporous 3D structure provides a large specific surface area, while the macropores also shorten the transport length of Li ions. The second project involves the use of a novel magnetic field-induced method for fabrication of wrinkled Fe_3O_4@RGO anode materials. The applied magnetic field improves the interfacial contact between the anode and current collector and increases the stacking density of the active material. The magnetic field treatment facilitates the kinetics of Li ions and electrons and improves electrode durability and the surface area of the active material. In the third project, poly (methacrylic acid) (PMAA)-induced self-assembly process was used to design super-mesoporous Fe_3O_4@RGO anode materials and their electrochemical performance as anode materials is also investigated. To establish correlations between electrode properties (morphological and chemical) and LIB performance, a variety of techniques were used to characterize the samples. The significant improvement in LIB performance of the 3D anodes mentioned above is largely attributed to the unique properties of graphene and the resulting 3D architecture.

Table of Contents

List of Figures ix
List of Tables xiv
Acknowledgements xv
Dedication xvi
Chapter 1 - Introduction 1
1.1 Review of Current Commercial Lithium-Ion Battery Technology 1
1.2 Motivation for Designing 3D Graphene-Based Anode Architectures for Lithium-Ion Batteries 4
1.2.1 Sheets-Like Graphene-Based Anodes 9
1.2.2 Core–Shell Graphene-Based Anodes 14
1.2.3 Foam-Like Graphene-Based Anodes 15
1.3 Perspective 17
Chapter 2 - Microgel-Assisted Assembly of Hierarchical Porous Reduced Graphene Oxide for High-Performance Lithium-Ion Battery Anodes 19
2.1 Introduction 19
2.2 Experimental Section 20
2.2.1 Synthesis of GO-NH_2/NMP Dispersion 20
2.2.2 Synthesis of Cross-Linked Poly (Methyl Methacrylate-co-Glycidyl Methacrylateco-Butyl Acrylate) [P (MMA-GMA-BA)] Polymer Spheres 21
2.2.3 Synthesis of 3D Hierarchical Porous/Wrinkled RGO Anodes 21
2.2.4 Structural and Chemical Characterization 23
2.2.5 Electrochemical Measurements 24
2.3 Results and Discussion 25
2.3.1 Fabrication of Porous/Wrinkled RGO Anode 25
2.3.2 Emulsion Polymerization Process of PS 26
2.3.3 Swelling-Shrinking Process of PS 30
2.3.4 Characterization of GO and GO-NH_2 33
2.3.5 Size Control of PS and GO-NH_2 37
2.3.6 Surface Morphology for GO@PS with/without Swelling-Shrinking Process 40

2.4 Electrochemical Properties of Porous/Wrinkled RGO Anode 46
2.5 Conclusion 53
Chapter 3 - Magnetic Field-Induced Fabrication of Fe_3O_4/Graphene Nanocomposites for Enhanced Electrode Performance in Lithium-Ion Batteries 54
3.1 Introduction 54
3.2 Experimental Section 56
3.2.1 Synthesis of Fe_3O_4/GO Nanocomposites 56
3.2.2 Preparation of Fe_3O_4–Citric Acid/GO Ethanol Dispersion 56
3.2.3 Preparation of Wrinkled Fe_3O_4/RGO Anodes 56
3.2.4 Materials Characterization 57
3.2.5 Electrochemical Measurements 58
3.3 Results and Discussion 58
3.3.1 Motivation of Align/Wrinkle Fe_3O_4/RGO Nanosheets 58
3.3.2 Chemical Characterization of Fe_3O_4/RGO 60
3.3.3 Morphology of Fe_3O_4/RGO Anode 64
3.3.4 Electrochemical Characterization of Fe_3O_4/RGO Anodes 68
3.4 Conclusion 73
Chapter 4 - PMAA-Induced Self-Assembly of Mesoporous Fe_3O_4@Graphene and Its Application in Lithium-Ion Batteries 74
4.1 Introduction 74
4.2 Experimental Section 76
4.2.1 Synthesis of PMAA 76
4.2.2 Preparation of Fe_3O_4@GO-PMAA Aqueous Solution 77
4.2.3 Self-Assembly of Porous Fe_3O_4@RGO Anodes 77
4.2.4 Materials Characterization 78
4.2.5 Electrochemical Measurements 79
4.3 Results and Discussions 79
4.3.1 pH-response of Fe_3O_4@GO-PMAA in Aqueous Dispersion 79
4.3.2 Chemical and Structure Characterization of Fe_3O_4@RGO Anode 88
4.3.3 Electrochemical Performance of Fe_3O_4@RGO Anode 93
4.4 Conclusions 96

Chapter 5 - Concluding Remarks 97
References 99
Appendix A - Supporting Results 123

List of Figures

Figure 1.1 Schematic illustration of a common LIB. Source: http//www.greencarcongress.com.. 2
Figure 1.2 Capacity and electrochemical potential of common cathodes and anodes materials for LIBs. Reprinted by permission from B. J. Landi, M. J. Ganter, C. D. Cress, R. A. DiLeo, R. P. Raffaelle, *Journal of Energy & Environmental Science*, 2009, 2, 638-654. Copyright 2009 Royal Society of Chemistry. 4
Figure 1.3 (a) Schematic representation of the synthesis of 3D Co_3O_4/CoO/graphene nanocomposite. (b) FESEM images of Co_3O_4/CoO/graphene nanocomposite and (c) pure Co_3O_4 nanoparticles. 11
Figure 1.4 Scanning electron microscopic images showing the morphology of (a) pure VAGN , (b) Sn@GS-VAGN, and (c) the rate capability of Sn@GS-VAGN. 12
Figure 1.5 Schematic illustration of the preparation of CuO nanosheets/graphene paper with SEM image and cycle performance. 13
Figure 1.6 (a) Schematic representation of synthesis process of sandwich-type Co_3S_4 porous nanosheets and graphene sheets (Co_3S_4-PNS/GS) via freeze drying and subsequent hydrazine treatment. (b) LIB performance of Co_3S_4-PNS/GS: rate capability at different current densities from 0.5 to 20 A/g, and (c) cycling performance and corresponding Coulombic efficiency at 0.5 A/g. 14
Figure 1.7 (a) 3D Fe_3O_4/graphene foam with low magnification SEM image, (b) high magnification image, (c) cycle performance at 6C and 10C rate, and (d) rate capability at different C-rates from 1C to 60C. 17
Figure 2.1 (a) Schematic illustration of swelling and shrinking process of cross-linked PS in NMP and distilled water, respectively. (b) Schematic illustration of the synthesis of a porous/wrinkled RGO structure: (1) Ring-opening reaction and charge attraction between GO-NH_2 and PS microgel in NMP; (2) shrinking of GO@microgel to wrinkled GO@shrunk PS in water; (3) removal of PS by annealing treatment at 600 °C for 3 hours. 23
Figure 2.2 Component of a common half-cell. 25
Figure 2.3 Schematic illustration of common mechanism of emulsion polymerization. 28
Figure 2.4 Molecular structures of monomers used for synthesis of cross-linked P (MMA-GMA-BA) spheres and the molecular structure of P (MMA-GMA-BA) spheres. 29

Figure 2.5 FT-IR spectrum of as-synthesized P (MMA-GMA-BA) spheres (0.1wt% DVB)..... 30
Figure 2.6 Picture of PS /NMP dispersions (0.02g/ml) for PS synthesized with 0, 0.1, and 0.5 wt% DVB shown as sample A1, A2, and A3, respectively. 32
Figure 2.7 (a) Correlation function G^2 (t) measured by DLS on the diluted PS/water dispersion at 25 ˚C (b) Correlation function G^2 (t) measured by DLS on the diluted microgel/NMP dispersion at 25 ˚C..... 33
Figure 2.8 Functionalization of graphene surface by Hummer's method[96]. Reprinted by permisssion from M.H. Jin, H.K. Jeong, T.H. Kim, K. P. So, Y. Cui, W. J. Yu, E. J. Ra and Y. H. Lee, *Journal of Physics D : Applied Physics*, 2010,43 (27), 275402..... 34
Figure 2.9 Introduction of NH_2 group on GO surface via reaction with ammonia solution[97]. Source from Ossila Ltd. 34
Figure 2.10 Raman spectra of GO and GO-NH_2 35
Figure 2.11 (a) XPS survey spectra of GO-NH_2 and GO; (b) C 1s XPS spectra of GO–NH_2 and GO; (c) N 1s XPS spectrum of GO-NH_2; and (d) N 1s XPS spectrum of GO–NH_2 before and after ion exchange. 37
Figure 2.12 SEM image of GO-NH_2 flakes. 39
Figure 2.13 Particle size distribution of as-synthesized PS (0.1 wt% DVB)..... 39
Figure 2.14 (a) SEM image of as-synthesized PS (0.1wt% DVB); (b) and (d) SEM and TEM images of GO wrapped as-synthesized PS (0.1wt% DVB) with smooth GO surfaces, respectively; and (c) and (e) SEM and TEM images of wrinkled GO@shrunk PS with wrinkled GO surfaces, respectively. 41
Figure 2.15 (a) Low-magnification SEM image of porous/wrinkled RGO after annealing treatment; the inset shows an image of wrinkled GO@shrunk PS before annealing treatment (scale bar =150 nm). (b) Low-magnification SEM image of stacked RGO sheets. 42
Figure 2.16 Weight loss vs. temperature curve by TGA analysis of cross-linked P (MMA-GMA-BA) microspheres (0.1wt%DVB). 42
Figure 2.17 Nitrogen adsorption-desorption isotherms of porous/wrinkled RGO and stacked RGO. 44
Figure 2.18 Pore size distribution modeled by non-local DFT (NLDFT) method for porous/wrinkled RGO and stacked RGO. 45
Figure 2.19 XRD patterns of stacked RGO and porous/wrinkled RGO. 46

Figure 2.20 (a) Cyclic voltammograms (CV) of porous/wrinkled RGO. (b) Galvanostatic charge-discharge profiles of porous/wrinkled RGO at a current rate of 0.2C. (c) Cycle performance and Coulombic efficiency of porous/wrinkled RGO at a current rate of 0.2C. (d) Rate capability of porous/wrinkled RGO cycled at different current rates (2C, 4C, 10C, 20C, 30C, and 2C). 48
Figure 2.21 (a) Comparison of cycle performance of porous/wrinkled RGO and stacked RGO cycled at a current rate of 4C. (b) Comparison of rate capability of porous/wrinkled RGO and stacked RGO cycled at different current rates (0.2C, 0.5C, 2C, 4C, 10C, and 0.2C). ... 49
Figure 3.1 Schematic illustration of synthesis of wrinkled Fe_3O_4/RGO anode *via* magnetic field-assisted process followed by annealing in argon. (a) Deposition of Fe_3O_4–citric acid/GO ethanol solution on copper foil by dip coating. (b) Annealing of the wrinkled Fe_3O_4–citric acid/GO anode on copper foil at 550 °C in argon for 2 hours. 57
Figure 3.2 Reduced diffusion distance for Li ions in align/wrinkle Fe_3O_4/RGO nanosheets[134]. Reformed by permission from J. Billaud, F. Bouville, T. Magrini, C. Villevieille, A. R. Studart, *Nature Energy*, 2016, 1, 16097. Copyright 2016 Springer Nature. 60
Figure 3.3 (a) XRD patterns of RGO, pure Fe_3O_4 nanoparticles, and as-synthesized Fe_3O_4/RGO nanocomposite. (b) Raman spectra of GO, RGO and Fe_3O_4/RGO nanocomposite. (c) XPS survey scan of Fe_3O_4–RGO nanocomposite. (d) TGA curve of Fe_3O_4/RGO nanocomposite under airflow at a temperature ramp of 5 °C min^{-1}. 62
Figure 3.4 Energy dispersive X-ray pattern of Fe_3O_4/RGO nanocomposite. 63
Figure 3.5 High-resolution XPS spectra of Fe 2p (a) and C 1s (b) for wrinkled and unwrinkled Fe_3O_4/RGO anodes and their related curve fitted components..... 64
Figure 3.6 SEM images of wrinkled and unwrinkled Fe_3O_4/RGO anodes. (a and b) Low- and high-magnification images of U-Fe_3O_4/RGO anodes synthesized without magnetic field treatment. (c and d) Low- and high- magnification images of W-Fe_3O_4/RGO anodes subjected to magnetic field and centrifugation treatments during synthesis (centrifugation at 6000 rpm for 15 min). (e and f) Low- and high- magnification images of W-Fe_3O_4/RGO anodes exposed to magnetic field without centrifugation. 66
Figure 3.7 SEM images of Fe_3O_4/RGO anode materials: (a) synthesized without exposure to magnetic field; (b) synthesized with exposure to magnetic field and centrifugation

treatment; and (c) synthesized with exposure to magnetic field without centrifugation treatment. 67
Figure 3.8 TEM images of Fe_3O_4/RGO. (a) Low-magnification image showing Fe_3O_4 nanoparticles. (b) Fe_3O_4 nanoparticles in contact with RGO. (c and d) High-resolution images of Fe_3O_4 nanoparticles. 68
Figure 3.9 (a) Cyclic voltammograms for the first 4 cycles of W-Fe_3O_4/RGO anode at a scan rate of 0.1 mV s−1 in the potential window of 3.0–0.001 V (vs. Li/Li^+). (b) Selected discharge–charge profiles (1st, 2nd, 3rd, 50th, and 100th cycle) of W-Fe_3O_4/RGO anode at a cycling rate of 0.2C. (c) Cycling performances of RGO and W-Fe_3O_4/RGO anodes at 0.2C. The coulombic efficiency of W-Fe_3O_4/RGO anode is also displayed (blue curve). (d) Cycling performance of W-Fe_3O_4/RGO and U-Fe_3O_4/RGO anodes at different cycling rates of 0.2C, 0.5C, 1C, 5C and 10C with a cutoff voltage window of 3.0–0.001 V. (e) Selected discharge–charge profiles (1st, 2nd, 3rd, 50th, and 100th cycle) of W-Fe_3O_4/RGO and U-Fe_3O_4/RGO anodes at a cycling rate of 2C. (f) Cycling performance of W-Fe_3O_4/RGO and U-Fe_3O_4/RGO anodes at a cycling rate of 2C with a cutoff voltage window of 3.0–0.001 V. 70
Figure 4.1 Illustration of self-assembly of crumpled Fe_3O_4/RGO anodes via adjusting pH of dispersion. 78
Figure 4.2 Structural difference between citric acid and PMAA. 82
Figure 4.3 Schematic illustration of the effect of pH on the chain conformations of PMAA. 82
Figure 4.4 Pictures of PMAA aqueous solution and Fe_3O_4@GO-PMAA aqueous suspensions with 1.2 mg/ml and 4.8 mg/ml PMAA at different pH levels. 84
Figure 4.5 UV-Vis spectra of Fe_3O_4@GO-PMAA aqueous suspensions with 1.2 mg/ml and 4.8 mg/ml PMAA at varying pH levels. 86
Figure 4.6 Particle effective diameter of Fe_3O_4@GO-PMAA aqueous suspensions with 1.2 mg/ml and 4.8 mg/ml PMAA at different pH levels. 87
Figure 4.7 Viscosity as a function of shear rate for Fe_3O_4@GO-PMAA aqueous suspensions with 1.2 mg/ml and 4.8 mg/ml PMAA at different pH levels 87
Figure 4.8 XRD pattern of Fe_3O_4@RGO 90
Figure 4.9 Raman spectrum of Fe_3O_4@RGO. 90
Figure 4.10 SEM images of (a) and (c) PMAA-induced porous Fe_3O_4@RGO; (b) and (d) citric acid-assisted stacked Fe_3O_4@RGO 91

Figure 4.11 Nitrogen adsorption-desorption isotherms (a) and pore size distribution (b) of PMAA induced porous Fe_3O_4@RGO. 92
Figure 4.12 TGA curve of Fe_3O_4@RGO acquired with a temperature ramp of 5 °C min^{-1}. 93
Figure 4.13 (a) Selected discharge–charge profiles (1st, 2nd, 3rd, 4th, and 200th cycles) of PMAA-stablized Fe_3O_4/RGO anode, (b) citric acid-stabilized Fe_3O_4@RGO anode at a current density of 2 A/g in the potential window of 3.0–0.002 V (*vs.* Li/Li^+), (c) Cycling performance of PMAA induced Fe_3O_4/RGO anode and (d) citric acid stabilized Fe_3O_4@RGO anode at different cycling rates of 0.5 A/g, 1 A/g, 2 A/g, 5 A/g and 10 A/g with a cutoff voltage window of 3.0–0.002 V. 95
Figure A.1 (a) and (b) SEM images of as-synthesized PS (0.1wt% DVB). 123
Figure A.2 SEM images of polymer spheres of different sizes ajusted by (a) 0.012, (b) 0.002 and (c) 0.0003 g/ml NaCl, respectively. 124
Figure A.3 (a) and (b) TEM images of GO wrapped as-synthesized PS (0.1wt% DVB) with smooth GO surfaces. 124
Figure A.4 (a) and (b) TEM images of wrinkled GO@shrunk PS with wrinkled GO surfaces. 125
Figure A.5 FTIR spectra of as-synthesized PMAA. 125
Figure A.6 TGA curve of PMAA under N_2 flow at a temperature ramp of 5 °C min^{-1}. 126
Figure A.7 SEM images of porous Fe_3O_4@RGO anodes. 126

List of Tables

Table 1.1 Comparison of characteristics of four common cathode materials. 3
Table 1.2 Comparison of characteristics of various anode materials[17]. Adapted by permission from W. J. Zhang, *Journal of Power Source*, 2011, 196, 13-24. Copyright 2011 Elsevier. .. 3
Table 1.3 Comparison of properties of carbon anodes materials in various architectures. Adapted by permission from H. Jiang, P. S. Lee, C. Z. Li, *Journal of Energy & Environmental Science*, 2013, 6, 41-53. Copyright 2012 Royal Society of Chemistry. 6
Table 1.4 Comparison of battery performance of graphene-based anodes materials in various architectures 9
Table 2.1 Summary of textural properties of stacked RGO and porous/wrinkled RGO obtained from physisorption. 44
Table 2.2 Comparison of electrode performance of porous/wrinkled RGO in the literature synthesized using a microgel-assisted method and a variety of high-performance carbon, graphene and RGO anodes. 51
Table 3.1 Atomic concentrations of aligned and unaligned Fe_3O_4/RGO nanocomposite from XPS survey scans. 62
Table 3.2 Comparison of cycling performance of Fe_3O_4/nanocarbon anodes synthesized by a magnetic field induced method. 72
Table 4.1 Dispersion state of PMAA aqueous solution and Fe_3O_4@GO-PMAA aqueous suspensions with 1.2 mg/ml and 4.8 mg/ml PMAA at varying pH levels. 83
Table 4.2 Zeta potential of Fe_3O_4@GO-PMAA aqueous suspensions with 1.2 mg/ml and 4.8 mg/ml PMAA at varying pH levels (*concentration was diluted to one-half of original concentration for testing). 83
Table A.1 Comparison of surface area of Fe_3O_4@RGO composites. 127

Acknowledgements

I would like to express my gratitude to my major advisor, Dr. Placidus B. Amama for his continuous support and guidance to my Ph.D. study and research. His expertise, patience, encouragement, and enthusiasm have helped me in surmounting many challenges and difficulties throughout my Ph.D. program. He has provided me with creative ideas toward the completion of the doctoral degree. I could not have accomplished the thesis without his support.

I would like to thank my committee members: Dr. Jennifer L. Anthony, Dr. Bin Liu, Dr. James H. Edgar and Dr. Jun Li for their valuable advice during the preliminary exam, Ph.D. program, and final defense of the thesis. I also would like to express my gratitude to my outside chair, Dr. Matthew J. Berg, for his willingness to participate in the final evaluation of my work.

I would like to thank our group members, especially Xu Li and Haider Almkhelfe, for the discussions about my research.

I am grateful to Dr. Christopher M. Sorensen in Department of Physics for the lab access and the support his student, Raiya Ebini, provided.

I would like to thank Jingyi Xie and Zahraa Alauda in Dr. Hohn's research group. I appreciate the help for materials characterization from them.

I am indebted to the wonderful staff in the Department of Chemical Engineering: Florence Sperman, Karey DeBardeleben, Pat Nelson, Danita Deters, Karen Strathman, Debi Wahl and David Threewit for their assistance and cooperation in events and activities related to my research.

I would like to thank my family for their full love, encouragement and support.

Thanks are due to all the professors and students who were involved in my four and a half years of study and training in Kansas State University.

Dedication

To my parents

Dongxiang Wang

Jinrong Yu

To my parents-in-law

Xinran Xie

Fengying Cao

To my husband, life partner, and best friend

Jingyi Xie

Chapter 1 - Introduction

Chapter 1 is reproduced in part with permission from:

Wang, H.; Li, X.; Baker-Fales, M.; Amama, P. B. 3D Graphene-Based Anode Materials for Li-ion Batteries. *Current Opinion in Chemical Engineering* **2016**, 13, 124-132.

1.1 Review of Current Commercial Lithium-Ion Battery Technology

Lithium-ion batteries (LIBs) hold substantial promise as the next-generation power devices due to their high-energy content, recharge-ability, low self-discharge, high operating voltage, wide temperature window, and no memory effect[1-3]. The huge interest in LIBs is evident from the rise in its global market value that has nearly doubled from $11.6 billion in 2012 to # 22.5 billion in 2016[4] . LIB shows high energy density compared to all types of capacitors and could solve the large energy demands from our daily life. LIB has been widely used for various portable consumer electronics, such as cell phones, computers, GPS, and cameras, and recently also been increasingly being considered for large-scale applications for militaries, large vehicles and aerospace applications.

LIBs are a type of rechargeable batteries in which lithium ions moves between the anode and cathode. A typical LIB design consists of anode, cathode, and membrane separator soaked with liquid electrolyte, as shown in the Figure 1.1. When the battery is discharged, Li ions are extracted from the anode. Then the ions travel through a thin polymer-based membrane separator, and are inserted into the cathode material; at the same time, the electrons flow from anode to cathode through the external circuit. On the other hand, during charging process, Li ions and electrons move along the opposite direction. In general, discharging and charging processes

are reversible, which has contributed to the popularity of LIB and has become a promising technology for daily use and various high-end purposes.

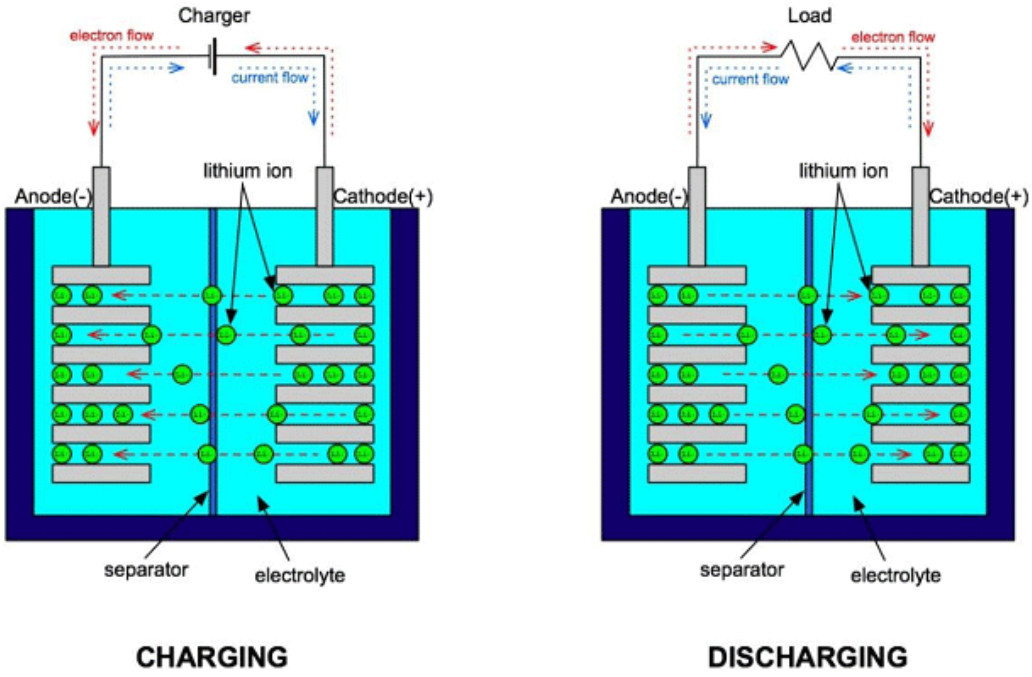

Figure 1.1 Schematic illustration of a common LIB. Source: http//www.greencarcongress.com.

The materials used for the anode and cathode can dramatically affect the LIB's performance. Tables 1.1[5-7] and 1.2[8-14] show the overall properties of commonly used materials for anodes and cathodes in LIBs. Commercially, the most popular material for the anode is graphite. The cathode is generally composed of lithium metal oxide[15], such as $LiCoO_2$, $LiMn_2O_4$, $LiFePO_4$ and $LiNiO_2$, as shown in the Tables 1.1 and 1.2. The reversible oxidation and reduction reactions occurring inside electrode materials account for the energy generated by LIBs. Since the electrochemical potential of cathode materials are much higher than that of anode (Figure 1.2), during discharging process, the cathode materials will be reduced, while the anode materials will be oxidized[16]. Conversely, cathode will be oxidized and the anode will be reduced

when charging the battery. The difference in electrochemical potential between electrode materials is the driving force for those reactions occurring. In the following, an example of typical reactions occurring during charging and discharging in LIBs is presented:

Overall reaction in a Li-ion cell: $6C + LiCoO_2 \leftrightarrow LiC_6 + Li_{0.5}CoO_2$ (1.1)

At the cathode: $LiCoO_2 - Li^+ - e^- \leftrightarrow Li_{0.5}CoO_2 \Rightarrow 143\ mA\ h\ g^{-1}$ (1.2)

At the anode: $6C + Li^+ + e^- \leftrightarrow LiC_6 \Rightarrow 372\ mA\ h\ g^{-1}$ (1.3)

Table 1.1 Comparison of characteristics of four common cathode materials.

	$LiCoO_2$	$LiMn_2O_4$	$LiFePO_4$	$LiNiO_2$
Theoretical Capacity (mA h g^{-1})	274	148	170	274
Operating Voltage (vs. Li/Li^+)	3.9	4.1	3.4	3.8
Density (g cm^{-3})	5.1	0.5	0.23	13
Crystal Structure	Layered	Spinel	Olivine	Layered
Electronic Conductivity (S cm^{-1})	7	430	106	62

Table 1.2 Comparison of characteristics of various anode materials[17]. Adapted by permission from W. J. Zhang, *Journal of Power Source*, 2011, 196, 13-24. Copyright 2011 Elsevier.

Materials	Li	C	$Li_4Ti_5O_{12}$	Si	Sn	Sb	Al
Density (g cm^{-3})	0.53	2.25	3.5	2.33	7.29	6.7	2.7
Lithiated phase	Li	LiC_6	$Li_7Ti_5O_{12}$	$Li_{4.4}Si$	$Li_{4.4}Sn$	Li_3Sb	LiAl
Theoretical specific capacity (mA h g^{-1})	3862	372	175	4200	994	660	993
Theoretical charge density (mA h cm^{-3})	2047	837	613	9786	7246	4422	2681
Volume change (%)	100	12	1	320	260	200	96
Potential vs. Li (~V)	0	0.05	1.6	0.4	0.6	0.9	0.3

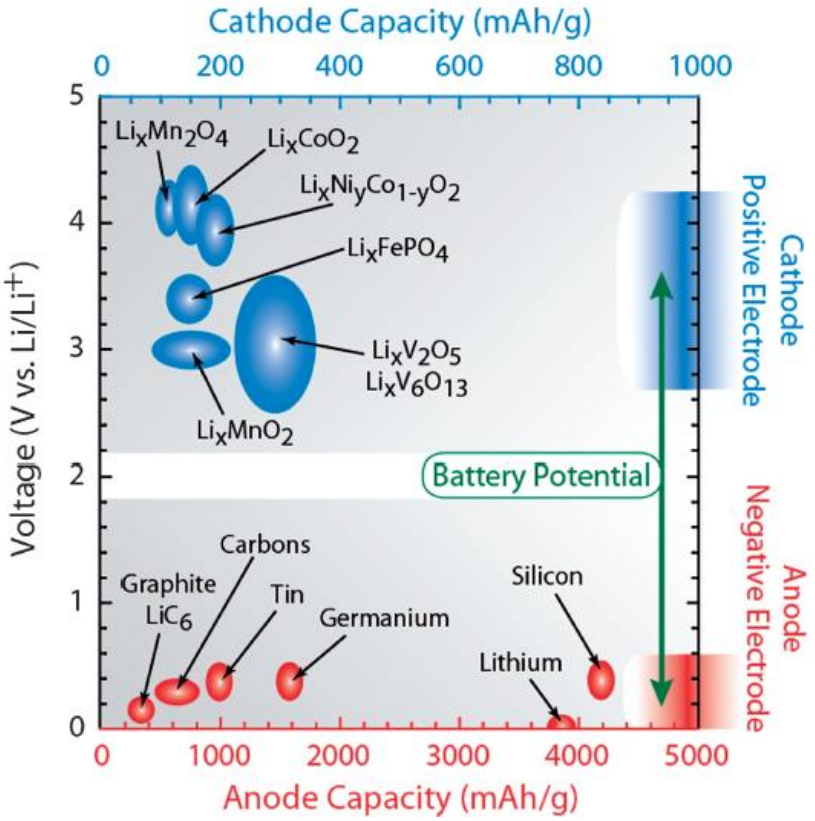

Figure 1.2 Capacity and electrochemical potential of common cathodes and anodes materials for LIBs. Reprinted by permission from B. J. Landi, M. J. Ganter, C. D. Cress, R. A. DiLeo, R. P. Raffaelle, *Journal of Energy & Environmental Science*, 2009, 2, 638-654. Copyright 2009 Royal Society of Chemistry.

1.2 Motivation for Designing 3D Graphene-Based Anode Architectures for Lithium-Ion Batteries

Current LIBs still lack a favorable combination of high rate capability, high reversible capacity, safety, and long cycle life that is required to meet the energy needs of future technologies especially in consumer appliances and the automotive industry. Therefore, there has been a major thrust to improve the properties of the LIB components (electrodes and electrolyte) given the strong dependence of the LIB performance of current commercial LIB technology on these components. Advances in synthesis and processing of nanocarbon materials particularly graphene have presented the opportunity to design novel Li-ion battery (LIB) anode materials

that can meet the power requirements of next-generation power devices. This section presents an overview of recent studies on the electrochemical behavior of three-dimensional (3D) nanostructured anode materials formed by coupling graphene sheets with alloying type active materials (metals or metal oxides). A number of promising 3D graphene-based hybrid anodes ranging from sheet-like, core-shaped, to foam-like morphologies are discussed. The significant improvement realized in the LIB performance of the 3D hybrid anodes is largely attributed to the unique properties of graphene and the resulting 3D architecture.

Graphite, the current state-of-the-art anode material, is plagued by a variety of problems including relatively low theoretical specific capacity (372 mAh/g), inhomogeneity in the structure, tortuous electrolyte diffusion paths, and high electrical and thermal resistances[18-20]. Also, graphite-based anode materials experience capacity deterioration at high cycling rates[21]. It is clear from the literature[22, 23] that the current electrode material and design fundamentally limit the energy stored and the deliverable power per unit area, mass, and volume. The long transport distance and low intrinsic diffusivity of Li ions through the solid electrolyte interface (SEI) both contribute to the power density limitation of in traditional LIBs[22, 24]. Given the dependence of the storage capacity on the charge/discharge rates, research continues to focus on increasing the power density without any tradeoff in attainable storage capacity[25]. Recent efforts to improve the power density of LIBs have focused mainly on the use of nanostructured electrodes with unique architectures to decrease the diffusion distance of Li ions[22, 24]. The characteristic time constant t for ionic diffusion is approximately proportional to the square of the diffusion distance L ($t \approx L^2/D$) where D is the diffusion constant[26, 27]. This means that the use of three-dimensional (3D) nanostructured electrodes with exceptionally short ion and electron transport distance (L) will

result in a significant decrease in the value of t as demonstrated by several studies[20, 28, 29]. Table 1.3 summaries the advantages of 3D electrode compared to other structured electrode[30].

Table 1.3 Comparison of properties of carbon anodes materials in various architectures. Adapted by permission from H. Jiang, P. S. Lee, C. Z. Li, *Journal of Energy & Environmental Science*, 2013, 6, 41-53. Copyright 2012 Royal Society of Chemistry.

	0D carbon onions	1D carbon nanotubes	2D carbon	3D graphene
Structure	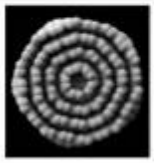	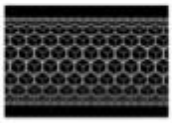	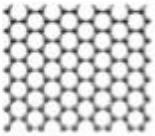	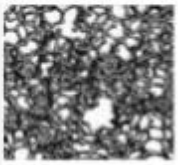
Conductivity	High	High	High	High
Weight Capacitance	Low	Low	Moderate	High
Cost	High	High	Moderate	Moderate
Li-ion flux	Moderate	Moderate	Moderate	High

In addition, a porous 3D nanostructured electrode design is expected to better accommodate the strain accompanying volume changes during cycling, and improved contact area with the electrolyte thereby increasing the Li ion flux across the interface. The search for higher capacity electrode materials have focused on alloying type materials such as metals and metal oxides (Si, Co_3O_4, Fe_3O_4, MoO_2, SnO_2, etc.) due to their significantly higher specific capacities in comparison to graphite. However, the use of these materials as anodes is plagued by poor cycling performances due to their poor conductivity, large volume expansion during cycling, and structural degradation via aggregation or pulverization[31-33]. An effective strategy for resisting the volume expansion of metal or metal oxide anodes during cycling and increasing

their low intrinsic electrical conductivity is to fabricate hybrid anodes by integrating carbon nanomaterial with the active material. The use of graphene, a 2D hexagonal lattice of sp2 carbon atoms[34], for the construction of 3D hybrid anodes is a promising route to alleviate these issues. Graphene has outstanding properties, in terms of electronic conductivity, thermal stability, structural flexibility, and surface area that make it well suited as a building block in 3D architectures. The use of 3D graphene architecture as host of metal/metal oxide active materials in anodes has several advantages[35]. Graphene serves as efficient and reliable conductive channels; graphene nanosheets facilitate charge transfer during the cycling process by forming an electrically conductive network with nanoparticles[33].

3D graphene structures provides void spaces for accommodating the volume expansion that occurs during Li insertion and extraction. The porosity, favorable geometry, and 3D conductive network provide a short path length for Li ion and electron transport that result in high rate capabilities. Pristine graphene exhibit a high reversible capacity of 1264 mAh/g at low current density (50–100 mA/g)[36, 37], therefore, the use of 3D graphene as host could provide additional Li ion storage. The anchoring of the nanoparticles or active materials on the graphene surface prevents agglomeration of the nanoparticles. However, note the high surface area of the 3D graphene host structure leads to excess irreversible capacity due to the increased edge sites that bind strongly to Li and promote decomposition of electrolyte to form the SEI layer[38]. Current strategies to decrease the irreversible capacity include introducing additives to common LiF_6-based electrolytes to enhance the stability of the resulting SEI layer[39], using prelithiated electrode materials to store extra Li ions before 1st cycle[40], and plugging the micropores of electrodes by Li_2CO_3 (the main component of SEI layer) to reduce the surface area of SEI[41]. Another issue with 3D graphene-based structures is the relatively low volumetric capacity due to

the low packing density of active materials in the highly porous host structure. To increase the loading density of active materials, the use of compressible 3D graphene-based aerogel[42] or shrinkable holey graphene-based hydrogel[43] have been explored. In this part, we present works on the electrochemical behavior of 3D nanostructured anode materials formed by graphene-supported alloying type active material. Based on theoretical calculations by Landi et al.[44], dramatic enhancement in LIB performance of over 50% is anticipated for 3D nanocarbon electrodes. In the following, the anode design, synthesis process, and LIB performance of promising 3D graphene-based anode materials are discussed; the hybrid materials can broadly be classified in terms of their structure and composition: sheets-like, core-shell shaped, and foams. A comparison of the electrochemical performance of representative 3D graphene-based anodes is summarized in Table 1.4.

Table 1.4 Comparison of battery performance of graphene-based anodes materials in various architectures

Architectures		Active components	Capacity (mA h g^{-1}) /Cycles	Current density (mA g^{-1})	Voltage window (V)	Ref.
Sheets-like		Co_3O_4, CoO	801.31/30	21.12	0.005-3.0	33
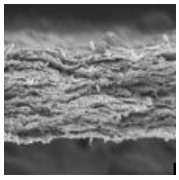 Parallel aligned sheets	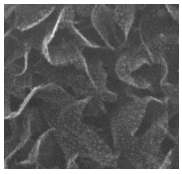 Vertical aligned sheets	CoS_2, CoS, Co_9S_8	954/50	100	0.005-3.0	45
		CuO	736.8/50	67	0.01-3.0	50
		Au, Si	1520/20	200	0.001-3.2	51
		N-doped MnO	722/90	100	0.01-3.0	74
		Sn	1005/130	150	0.001-3.0	49
Core/shell		Si	1335/80	200	0-2.0	54
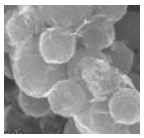	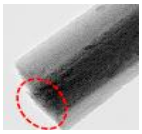	SiO_2	1299.6/25	210	0.01-1.2	55
		TiO_2	153/300	3350	1.0-3.0	56
Foams		MoS_2 (85%)	1200/30	600	0.01-3.0	62
	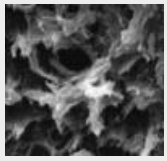	SnO_2	1340/200	500	0.01-3.0	67
		TiO_2	200/50	100	1.0-3.0	65
		Fe_3O_4	1130/200	100	0.001-3.0	73

1.2.1 Sheets-Like Graphene-Based Anodes

The sheet-like shaped graphene-based anodes have become the most common 3D architectures for LIBs. The graphene sheets and the active materials (usually in the form of nanoparticles) are combined, resulting in nanoparticles deposited on the sheets that tangle

together to form unique 3D anode materials. The sheet-like 3D graphene-based anodes are synthesized via either in situ or ex situ assembly of nanomaterials on graphene sheets. A widely used in situ assembly method is hydrothermal process, which yields stronger interactions between the nanoparticle and the graphene sheets. In addition, the synthesized porous 3D nanocomposites are well adapted to accommodate the volume expansion during cycling. As an example, Rai et al.[33] used a urea-assisted auto-combustion method to fabricate Co_3O_4 nanoparticles/graphene nanosheets as shown in Figure 1.3a. The process resulted in a nanocomposite containing 25–50 nm Co_3O_4 and CoO nanoparticles deposited on the graphene nanosheets. The nanocomposite electrode delivered an initial charge capacity of 890 mAh/g and exhibited 90% capacity retention after 30 cycles while the reversible capacity of the pure Co_3O_4 nanoparticles anode fades continuously, showing a capacity retention of only 60% after 30 cycles. The difference in LIB performance is attributed to the 3D porous structure of Co_3O_4/CoO/graphene nanocomposite (Figure 1.3b) and the intimate contact between the nanoparticles and graphene sheets. In the case of the pure Co_3O_4 nanoparticles, there is severe nanoparticle aggregation (Figure 1.3c) that is detrimental to LIB performance. Other studies[32, 35] have observed similar trends: the 3D graphene/metal or metal oxide nanoparticle anodes have consistently shown significantly better LIB performance than the pure nanoparticle anode. 3D graphene-based electrodes involving diverse cobalt sulfide compounds (CoS_2, CoS, Co_9S_8) and Fe_2O_3 synthesized by various hydrothermal methods also have excellent cycling durability and high rate capability[45, 46].

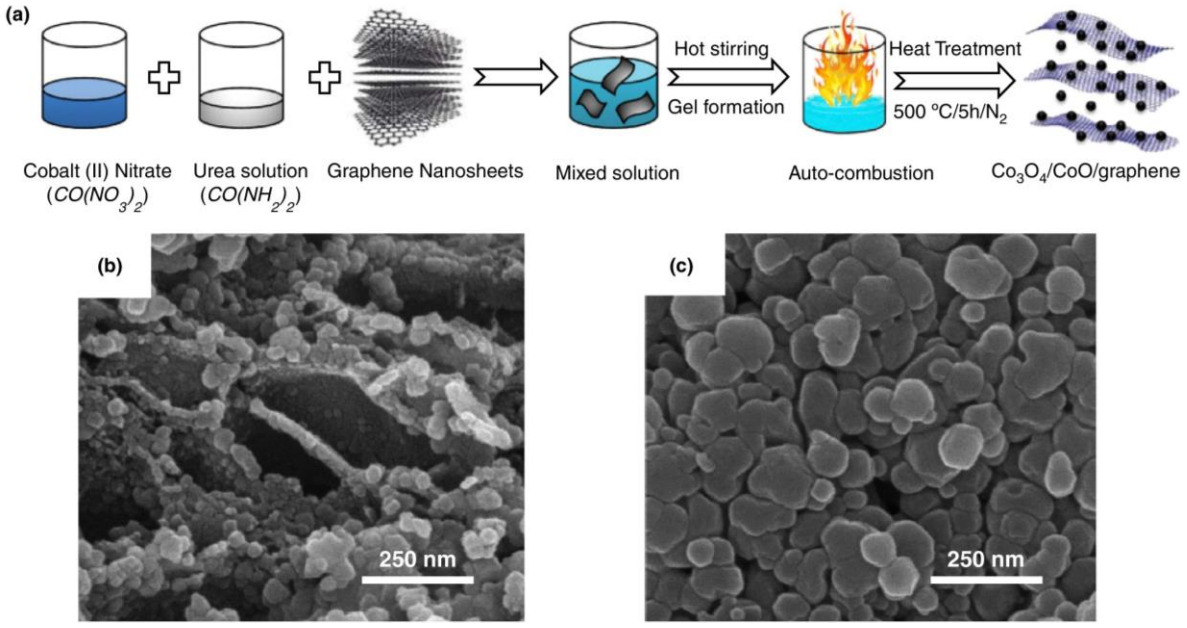

Figure 1.3 (a) Schematic representation of the synthesis of 3D Co_3O_4/CoO/graphene nanocomposite. (b) FESEM images of Co_3O_4/CoO/graphene nanocomposite and (c) pure Co_3O_4 nanoparticles.

Besides parallel graphene-based sheet anodes, vertically aligned graphene sheets on a Cu current collector for LIB anode have been fabricated by microwave plasma-enhanced chemical vapor deposition as shown by Xiao et al.[47]. Owing to the direct transport of electrons and ions from the current collector to the electrolyte along aligned graphene sheets, aligned anodes are expected to exhibit significantly improved rate capability. As examples, after in situ deposition of Si or Sn nanoparticles on the aligned graphene sheets, the resulting anodes exhibited outstanding rate capability and higher specific capacity; Figure 1.4 shows images of pristine vertically aligned graphene (VAGN) and the well-dispersed Sn-encapsulated graphene on VAGN (Sn@GS-VAGN), as well as the excellent rate capability of the Sn@GS-VAGN [48, 49].

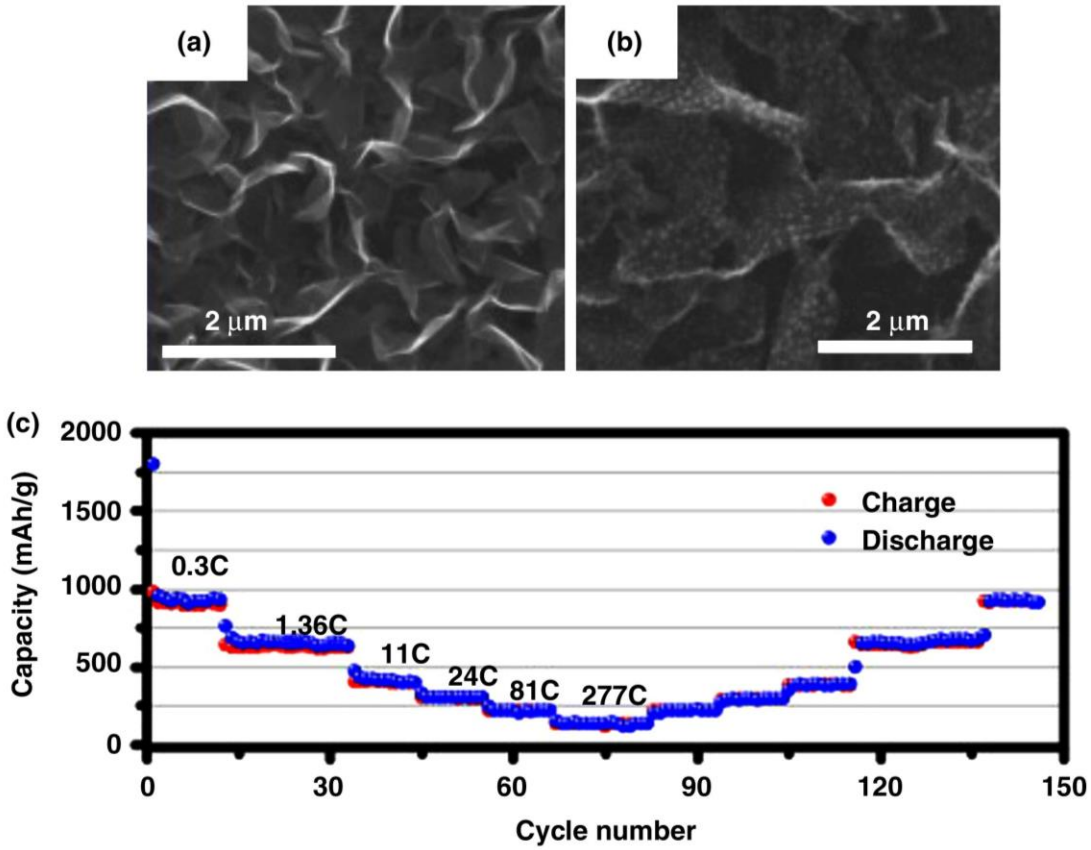

Figure 1.4 Scanning electron microscopic images showing the morphology of (a) pure VAGN , (b) Sn@GS-VAGN, and (c) the rate capability of Sn@GS-VAGN.

A second approach used to synthesize sheet-like 3D graphene-based anodes is ex situ assembly of graphene and metal/metal oxide nanomaterials. This typically involves a two-step process of synthesis of nanoparticles, followed by their deposition on graphene sheets, usually via vacuum filtration. As examples, Liu et al.[50] synthesized a free-standing, binder-free CuO nanosheets/graphene hybrid lamellar paper while Kim et al.[51] synthesized a gold-coated silicon nanowire/graphene (Au-SiNWs/G) hybrid film anode by vacuum filtration using an anodic aluminum oxide membrane. The CuO nanosheets/graphene sample demonstrated excellent cyclic retention with the specific capacity of 736.8 mAh/g after 50 cycles (Figure 1.5). The binder-free Au–SiNWs/G composite with the unique 3D structure showed higher energy density (reversible

capacity of 1520 mAh/g) than the binder-based composites and pure SiNWs. Recent reports on the synthesis of 3D sandwich-type architecture involving graphene have focused on Co-based materials. Du et al.[52] detail a facile and low-cost method to embed Co_3S_4 porous nanosheets in graphene sheets (Co_3S_4-PNS/GS) via freeze drying and subsequent hydrazine treatment (Figure 1.6a). The resulting Co_3S_4- PNS/GS benefits from the synergistic effect of the two components (Figures 1.6b, c), evidenced by the outstanding rate capability and cycling stability (showed a specific capacity of 710 mAh/g after 200 cycles). The improved LIB performance of Co_3S_4-PNS/GS anode is attributed to the enhanced electron and Li ion kinetics, larger surface area, and mechanical flexibility provided by the graphene nanosheets in the composites.

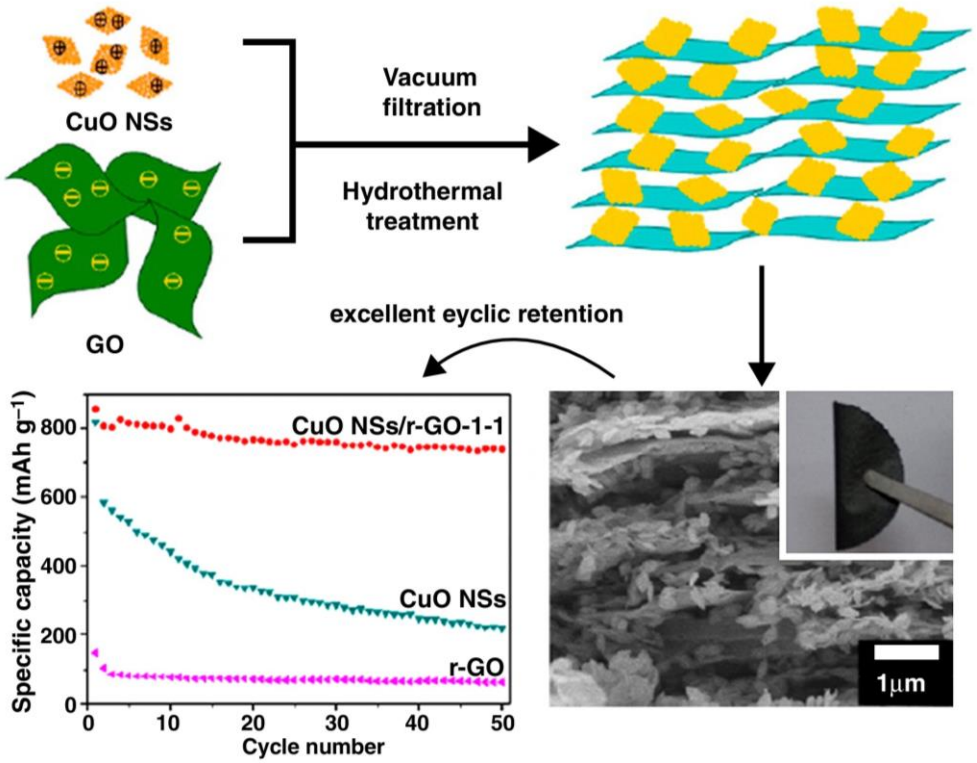

Figure 1.5 Schematic illustration of the preparation of CuO nanosheets/graphene paper with SEM image and cycle performance.

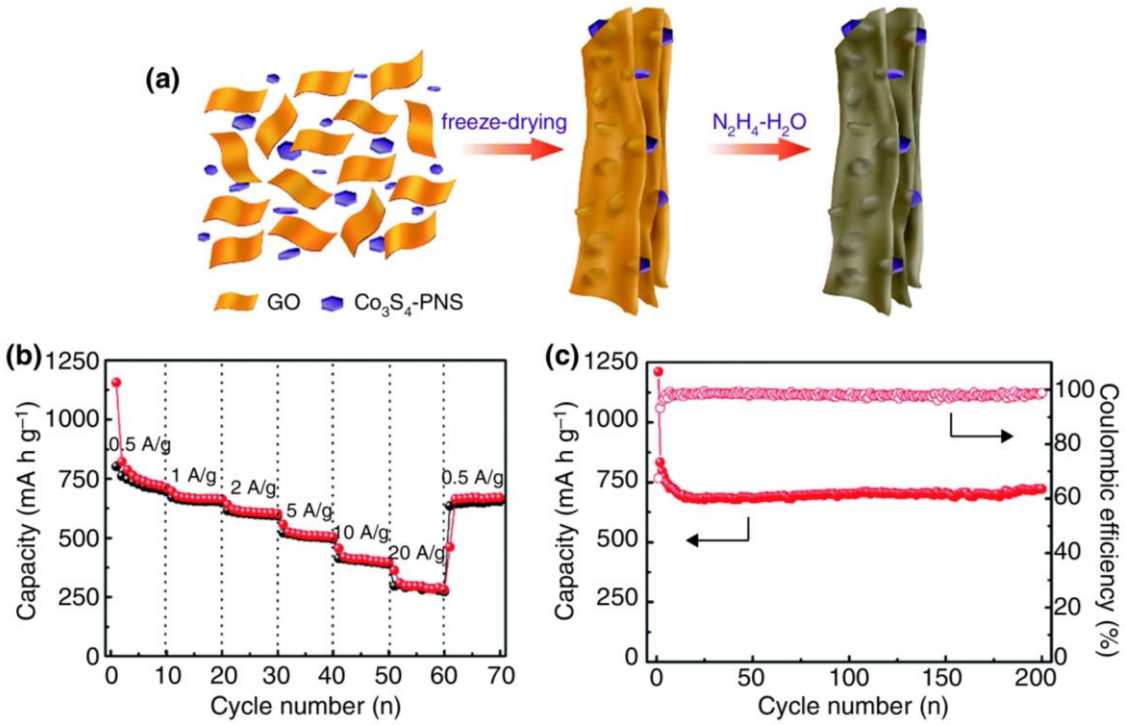

Figure 1.6 (a) Schematic representation of the synthesis process of sandwich-type Co_3S_4 porous nanosheets and graphene sheets (Co_3S_4-PNS/GS) via freeze drying and subsequent hydrazine treatment. (b) LIB performance of Co_3S_4-PNS/GS: rate capability at different current densities from 0.5 to 20 A/g, and (c) cycling performance and corresponding Coulombic efficiency at 0.5 A/g.

1.2.2 Core–Shell Graphene-Based Anodes

An effective strategy for resisting the volume expansion of Si anodes during cycling and improving the low intrinsic electrical conductivity is to integrate carbon nanomaterial with Si nanoparticles. The combination of graphene and Si nanoparticles in a 3D architecture improves the cycling stability of the anodes[53, 54]. For example, Zhu et al.[55] adopted the electrostatic self-assembly method to wrap negatively charged graphene on the positively charged silicon nanowires. The resulting Si–graphene hybrid with a core–shell structure enhances the conductivity of Si nanowires, diffusion of ions and electrons, and the accommodation of the Si expansion during cycling. Another approach that has been used to integrate graphene and Si is layer-by-layer assembly followed by in situ magnesiothermic-reduction. Due to its unique

structural features, the 3D core–shell Si microspheres–graphene network exhibited significantly enhanced LIB performance (specific capacity, cycling stability and rate capability) compared to the bare Si spheres[53]. Electrodes composed of graphene-wrapped active materials have been encapsulated in graphene sheets via several methods. A promising example is graphene nanoscrolls consisting of rolled-up graphene nanosheets with a unique tubular structure, which has been touted as an excellent substrate for electrode active materials, as the tubular cavities can provide pathways for ion transport while the outermost graphitic layer can facilitate efficient electron transport[56, 57]. The nanoscrolls are characterized by scrolled conformation, porous structure, adjustable interlayer distance and ends/edges that are open-ended cylindrical structure[58]. The effective use of graphene-based nanoscroll geometry with TiO_2 (B) nanowires to achieve improved LIB performance has been demonstrated by Li et al.[56].

1.2.3 Foam-Like Graphene-Based Anodes

We note that an advantage of integrating graphene with electrode active materials in composites is that it inhibits the inevitable agglomeration and restacking of graphene sheets due to the strong p–p interactions and van der Waals forces; this problem significantly reduces the specific surface area and lowers the electron and ion transport[59-61].

Recent efforts to exploit the outstanding properties of graphene in LIB anodes have also focused on depositing electrode active materials on 3D graphene foams. Studies[62-65] have shown that 3D graphene aerogel foams can overcome the restacking issue associated with graphene to some extent and provide a porous structure with large surface area and fast electron transport kinetics due to the continuous graphene back-bone. As examples, the synthesis of 3D graphene foams via template-assisted and gel-assisted approaches is discussed. In the case of template-assisted method, 3D graphene is grown on various templates such as polymer microspheres,

carbon skeletons, or metal/metal oxide foams. In Huang's work[66], binder-free MoO_2 nanoparticles were uniformly anchored on the surface of graphene/ Ni foam via a facile CVD process. The enhanced capacity and rate performance of MoO_2/graphene foam compared to bulk MoO_2 and pure graphene foam can be ascribed to the synergistic effect between MoO_2 nanoparticles and graphene layers. For the gel-assisted method, Wang et al.[67] developed a solvothermal-induced self-assembly process for the synthesis of a macroscopic SnO_2/N-doped 3D graphene foam; the electrode exhibited extraordinarily prolonged cycling stability at high current densities. A bottom-up strategy assisted by atomic layer deposition was utilized by Luo et al.[31] to synthesize a 3D graphene foam/Fe_3O_4 composite (Figures 1.7a and b) that exhibited a high reversible capacity and excellent rate capability even at a high C-rate of 60C (Figures1.7c and d). Given the enhancement in cycle life and Li storage capacity observed in N-doped graphene[68], the use of doped graphene in 3D architectures has also been explored. Chemically derived methods [69, 70] and a chemical vapor deposition technique[71] have been developed to produce heteroatom-doped graphene with stable reversible capacity at high discharging and charging rate. The SnO_2/N-doped 3D graphene foam mentioned above is an example of doped 3D graphene-based hybrid anodes. Also, using 7, 7, 8, 8-tetracyanoquinodi-methane as nitrogen precursor, Wang et al.[72] synthesized N-doped graphene-SnO_2 sandwich paper that exhibited very high capacity, high rate capability and outstanding cycling stability. The performance is attributed to several factors including nitrogen doping that creates surface defects, short transport distance of Li ions and electrons, and the huge elastomeric space to accommodate volume changes during cycling. Other 3D N-doped hybrid anodes with high LIB performance that have been reported include Fe_3O_4/N-doped graphene foam and MnO/N-doped graphene nanosheets[73, 74].

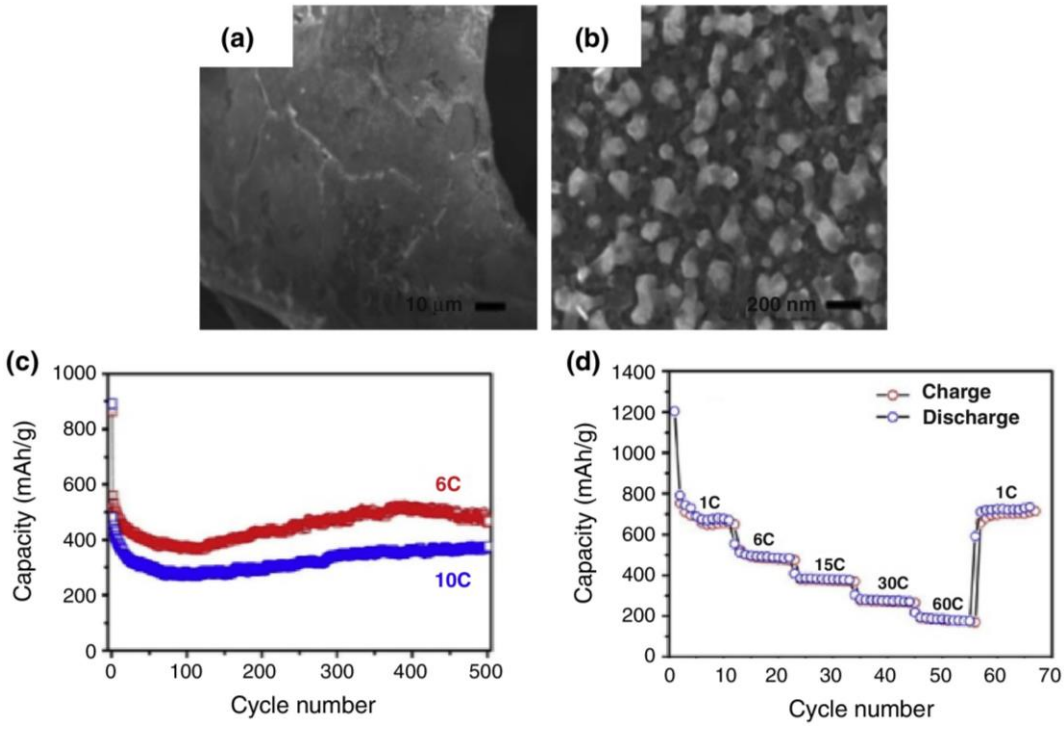

Figure 1.7 (a) 3D Fe_3O_4/graphene foam with low magnification SEM image, (b) high magnification image, (c) cycle performance at 6C and 10C rate, and (d) rate capability at different C-rates from 1C to 60C.

1.3 Perspective

Although 3D nanocarbon-based electrodes hold great promise in improving LIB performance, the challenges associated with their synthesis, dimensional control, and high electrode–electrolyte surface area that induces the high irreversible capacity have continued to hinder their widespread application in LIBs. In addition, there is little mechanistic understanding of the complex interactions within the multicomponent 3D electrode system (current collector, active material, and electrolyte). Consequently, there is currently a complete lack of guidelines for rational design and synthesis of high-performance 3D nanostructured electrodes. The seminal review paper on 3D nanostructured electrodes by Rolison et al.[24] describes the major barrier limiting the innovative synthesis of complex 3D nanostructured electrodes for energy storage and

conversion applications as ‘understanding the physical, chemical, and electrochemical interactions within multicomponent nanoscale systems.’ Future computational and experimental studies are required to illuminate the interrelationships between the properties (structural and chemical) of 3D nanocarbon-based electrodes and the LIB performance. As examples, density functional theory (DFT)-based first principle calculations can be applied to predict delithiated and lithiated phases, average lithium intercalation voltage, charge distribution, phase stability and transformation, and lithium diffusion kinetics[75, 76] while pair distribution function (PDF) analysis is a powerful approach for understanding the local structural changes that occur in the electrode during cycling[77]. Advances in nanocarbon materials particularly carbon nanotubes and graphene have presented the opportunity to design novel energy storage materials that can meet the power requirements of next-generation power devices. However, there are still fundamental challenges in the characterization of the complex 3D morphology. Electron tomography could become a powerful technique for 3D imaging and com-positional mapping of 3D electrodes. The combination of electron tomography and gas physisorption data may yield a complete picture of the aperiodic 3D electrode structure. In this review, we have summarized recent progress in the development of 3D graphene-based hybrid anodes for rechargeable LIBs. A selection of promising anodes with sheet-like, core-shaped or foam morphologies have been discussed. The improved LIB performance observed for the 3D hybrid anodes is attributed to several factors including high Li-ion flux across the interface, short diffusion pathways for both Li ions and electrons, abundant active sites for Li storage, and high freedom for volume change during charging/ discharging.

Chapter 2 - Microgel-Assisted Assembly of Hierarchical Porous Reduced Graphene Oxide for High-Performance Lithium-Ion Battery Anodes

Chapter 2 is reproduced in part with permission from:

Wang H.; Xie J.; Almkhelfe H.; Zane V.; Ebini R.; M. Sorensen C.; and Amama P. B. Microgel-assisted assembly of hierarchical porous reduced graphene oxide for high-performance lithium-ion battery anodes. *Journal of Materials Chemistry A* **2017**, 5, 23228-23237.

2.1 Introduction

A scalable and cost-effective approach for fabricating graphene-based electrode materials involves use of graphene oxide (GO) obtained via direct exfoliation of graphite. However, due to van der Waals interactions and the high aspect ratio of GO sheets, the sheets can easily restack and form a bulk graphite-like structure during conventional synthesis processes[78]. The restacking of graphene sheets results in significant loss of usable Li-insertion sites, and consequently, a decrease in specific capacity and rate capability of the electrode[79]. Therefore, it is necessary to develop synthesis strategies that preserve the interlayer space and Li insertion sites of graphene. A number of studies have been conducted on the assembly of graphene sheets into 3D graphene networks with controlled morphology for accommodating the ubiquitous restacking of graphene sheets[80-82]. Recent reports have shown that graphene with micro/meso/macropores can reduce the Li-ion diffusion distance and provide additional Li-ion storage sites due to the ultra-thin shells and available active edges of pores[80, 83]. Conventional approaches for design of porous graphene structures have taken advantage of sacrificial templates such as salts, inorganic oxides, and

colloidal particles[81, 84, 85]. Besides template-assisted designs, self-assembly strategies (e.g., spray-assisted deep-frying process[82] and "breath figure" method[86]) have also been used to fabricate 3D graphene structures with high surface areas and porosity that support fast Li-ion diffusion. However, controlled synthesis of 3D hierarchical graphene structures with mesopores and macropores as well as unstacked graphene sheets, remains a challenge.

Motivated by strategies discussed above, we demonstrate the synthesis of 3D, hierarchical, porous/wrinkled reduced graphene oxide (RGO) anodes via a microgel-assisted method. The facile and scalable approach (Figure 2.1) involves controlled wrapping of GO sheets on the surface of thermal, degradable polymer sphere (PS) microgels, followed by shrinkage of PS microgels to generate GO wrinkles. To the best of our knowledge, this is the first study that utilizes controlled swelling of PS microgels in an organic solvent and subsequent shrinking in water to produce 3D hierarchical macro/mesoporous RGO. The formed porous/wrinkled RGO, with macropores (diameter ~200 nm) and large amounts of mesopores (diameter ~3.9 nm) in the gap of neighboring RGO wrinkles after removal of PS, not only effectively reduces the Li-ion diffusion resistance inside RGO sheets, but also provides additional accessible sites (on the walls and edges of pores) for Li-ion intercalation. The resulting anode material achieves a high reversible capacity (~720 mAh/g at 0.2C) and high rate capability (~160 mAh/g at 20C). Moreover, the microgel-assisted approach described in this study opens up a promising strategy for controlled fabrication of 3D graphene-based electrodes.

2.2 Experimental Section

2.2.1 Synthesis of GO-NH_2/NMP Dispersion

GO was synthesized from natural flake graphite by the modified Hummers method[87]. A solution of 1mg/mL GO-NH_2 and N-Methyl-2-pyrrolidone (NMP) was prepared by mixing and

stirring an initial mixture of 40 mg of GO and 4 mL 28% ammonium hydroxide solution with 40 mL of NMP solvent at 60 °C for 9 hours.

2.2.2 Synthesis of Cross-Linked Poly (Methyl Methacrylate-co-Glycidyl Methacrylateco-Butyl Acrylate) [P (MMA-GMA-BA)] Polymer Spheres

Four g methyl methacrylate (MMA), 0.8 g glycidyl methacrylate (GMA), 0.2 g butyl acrylate (BA), and 5μL divinylbenzene (DVB) were first emulsified by 0.08 g 2, 2′-azobis (2-methylpropionamidine) dihydrochloride (AIBA) in a 100-mL round-bottom flask with 50 ml of distilled water. The solution was then flushed with nitrogen for 30 min to remove oxygen. The polymerization reaction was carried out for 3 hours in a nitrogen atmosphere at a fixed temperature of 65 °C, while being stirred at 550 rpm. Resulting milky dispersions were filtered and purified by repeated washing with ethanol and distilled water. Finally, cross-linked P (MMA-GMA-BA) polymer spheres were dried in a vacuum oven at 50 °C for 24 hours.

2.2.3 Synthesis of 3D Hierarchical Porous/Wrinkled RGO Anodes

A 0.02 g/mL PS microgel/NMP dispersion was prepared by swelling as-synthesized P (MMA-GMA-BA) polymer spheres in NMP solvent at room temperature. Forty ml of 1 mg/mL GO-NH_2/NMP dispersion was used to wrap 4 ml of the 0.02 g/ml PS microgel/NMP dispersion.

Multiple TEM images (Figure A.4) show that most of the GO sheets wrap around polymer spheres with fewer free GO sheets left. On the basis of TEM data and the stability of GO dispersion even at high centrifugation speed, we assume that the synthesized GO has few layers. Therefore, the mass ratio (m) of PS to GO-NH_2 should be controlled in the lower range, which is about 2.0 (value used in this Chapter). The mass ratio was estimated as follows:

$$V * \rho = m * SA * \delta * \alpha \quad (2.1)$$

where V is volume of PS = ~8780076 nm^3 (DLS diameter = 256 nm); ρ is density of PS = ~1.2 g/cm^3; SA is surface area of PS micro-gel = ~1216768 nm^2 (DLS Diameter = 623nm); δ is thickness of GO = ~ 1-4 nm (number of layers of GO sheets based on TEM images, thickness of single-layer GO = ~0.47-1.4 nm); α is density of GO = ~1.9 g/cm^3.

The wrapping process was then carried out at 60 °C for 8 hours. After wrapping the microgel with GO sheets, the as-synthesized solution was added dropwise to distilled water, resulting in a volumetric ratio of 1:7 for as-synthesized solution and distilled water, respectively; this step was carried out to shrink the volume of GO-encapsulated microgels (GO@microgels) and form wrinkled GO-encapsulated shrunk PS (wrinkled GO@shrunk PS). Porous/wrinkled RGO was obtained by annealing the wrinkled GO@shrunk PS under argon at 600 °C for 3 hours. Final steps for preparing the anode material involved mixing the porous/wrinkled RGO and poly(vinylidene difluoride) (PVDF) binder at a mass ratio of 9:1, respectively. The mixture was then sonicated in NMP and dip-coated onto a copper current collector (9 μm thick) to form a dry layer under vacuum at 100 °C with an estimated mass loading of ~ 1 mg/cm^2.

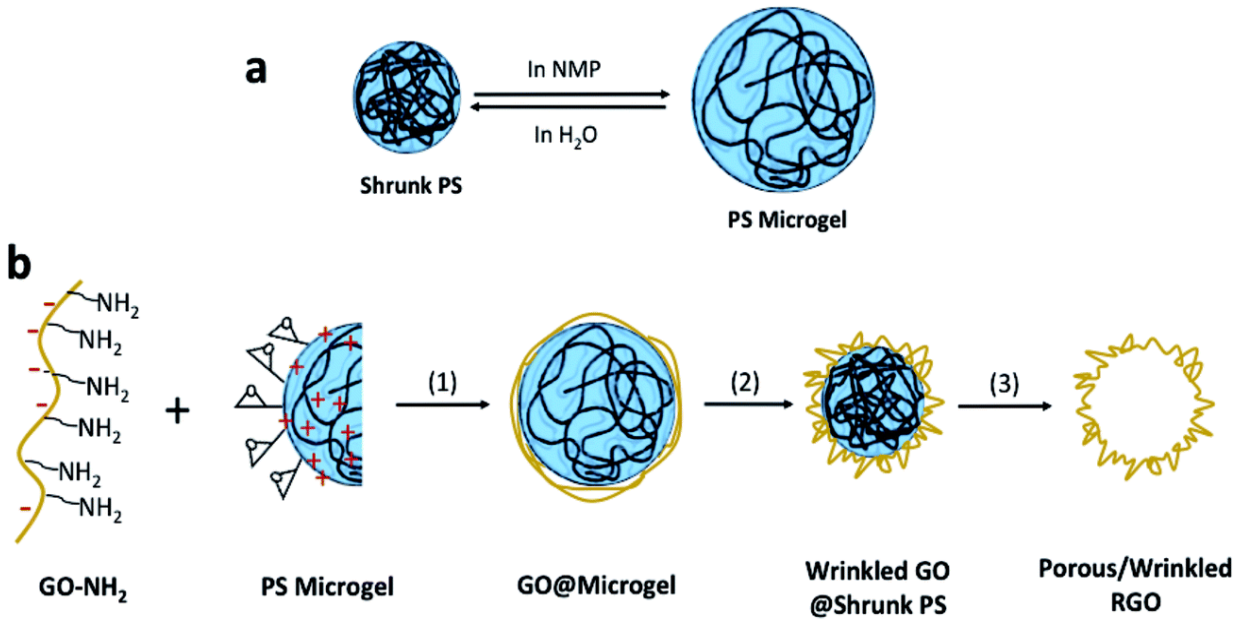

Figure 2.1 (a) Schematic illustration of swelling and shrinking process of cross-linked PS in NMP and distilled water, respectively. (b) Schematic illustration of the synthesis of a porous/wrinkled RGO structure: (1) Ring-opening reaction and charge attraction between GO-NH_2 and PS microgel in NMP; (2) shrinking of GO@microgel to wrinkled GO@shrunk PS in water; (3) removal of PS by annealing treatment at 600 °C for 3 hours.

2.2.4 Structural and Chemical Characterization

The morphological characterization of the samples was conducted using a field emission scanning electron microscope (FESEM, Hitachi S5200) and a transmission electron microscope (TEM, FEI Tecnai F20 XT). For TEM imaging, a small amount of wrinkled GO@shrunk PS sample was dispersed in water via ultrasonication; a drop of the homogeneous suspension was deposited on a holey carbon TEM grid and examined by TEM operating at 200 kV. X-ray photoelectron spectroscopy (XPS) data were obtained using a PerkinElmer PHI 5400 electron spectrometer with an achromatic Al Kα X-ray source (1486.6 eV) operating at 300 W (15 KV and 20 mA). Base pressure of the chamber during measurement was controlled at less than 5×10^{-8} Torr. Before testing the samples, the spectrometer was calibrated by setting the binding energies of Au $4f_{7/2}$ and Cu $2p_{3/2}$ to 84.0 and 932.7 eV, respectively. The analyzer pass energy

was set to 44.8 eV and contact time was 100 ms. For high-resolution measurement of O 1s, N 1s, and C 1s spectra, the analyzer's pass energy was set to 17.9 eV and contact time was 25 ms. All XPS spectra were charge-corrected by referencing to C 1s peak at 284.6 eV. XPS spectra were collected for GO-NH_2 after prolonged (3 days) ion exchange treatment with HCl (pH=1) to replace NH_4^+ with H^+. The GO-NH_2/HCl aqueous solution was repeatedly washed and centrifuged 10 times by distilled water until GO-NH_2 until HCl was completely removed and GO-NH_2 sheets could form a highly stable dispersion in water. Thermogravimetric analysis (TGA) was performed on a TGA-550 analyzer (TA Instruments) under a stream of N_2 flow (100 sccm) with a temperature ramp of 5 °C/min from room temperature to 600 °C.

FTIR spectra were recorded on a Cary 630 Agilent spectrometer at a resolution of 4 cm^{-1}. Raman spectra were obtained using an iHR550 spectrometer at a wavelength of 532 nm. Dynamic light scattering (DLS) was performed at a scattering angle of 90° using a 35mW He-Ne laser and a Langley-Ford correlator. P (MMA-GMA-BA)/NMP dispersion was diluted by NMP and sonicated for 1 hour before DLS measurement. Brunauer-Emmet-Teller (BET) specific surface area was determined from N_2 adsorption by using a Quantachrome (Autosorb-1) instrument at liquid nitrogen temperature.

2.2.5 Electrochemical Measurements

Assembly of the half-cell took place in an argon-filled glovebox with concentrations of moisture and oxygen below 0.5 ppm. A standard sized coin cell (diameter of ~18 mm and height of ~4 mm) was used for electrochemical testing. The composition parts of coin cell were present in the Figure 2.2. The working electrode was produced by coating the mixture of porous/wrinkled RGO and PVDF (10 wt%) binder on a Cu foil current collector. Microporous polypropylene membrane and Li foil were used as the separator and counter electrode,

respectively. The electrolyte used was 1 M LiPF6 solution in an ethylene carbonate (EC)/dimethyl carbonate (DMC)/diethyl carbonate (DEC) mixture (1: 1: 1, in vol%). On a Maccor 4300 electrochemical workstation, cyclic voltammetry (CV) of the cells was performed at 0.1 mv/s in the voltage range of 0.002–3.000 V, while galvanostatic cycling experiments were tested in the voltage range of 0.002 – 3.000 V versus Li^+ /Li at room temperature.

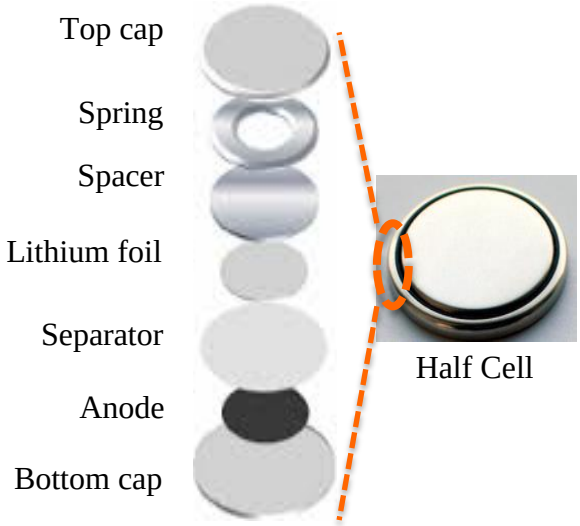

Figure 2.2 Component of a common half-cell. Reproduced with permission from C. R. Birkl, E. McTurk, M. R. Roberts, P. G. Bruce, and D. A. Howey. *J. Electrochem. Soc.*, 162 (12) A2271-A2280. Copyright 2003 The Electrochemical Society.

2.3 Results and Discussion

2.3.1 Fabrication of Porous/Wrinkled RGO Anode

Figure 2.1 illustrates the overall synthetic procedure of hierarchical macro/mesoporous RGO materials. As shown in Figure 2.1a, cross-linked PS swells to microgel in NMP; however, microgel shrinks back to shrunk PS after replacing NMP with distilled water. Solubility of the polymer in solvents plays an important role in formation and shrinking of microgels. In a "good solvent," the polymer chains will adopt a self-avoiding random walk configuration that

maximizes contact with the solvent. However, in a "poor solvent," the polymer chains collapse, forming a dense polymer mass that excludes solvent molecules from their interior. To satisfy the lower free energy at a given temperature, the polymer chains adopt a crumpled spherical state. Figure 2.1b shows the three main synthetic steps for porous/wrinkled RGO anodes. In step (1), PS microgels are encapsulated with a thin layer of smooth GO sheets, possibly due to two reasons. First, the epoxy groups on the surface of PS microgels may undergo ring-opening reaction with NH_2 groups on the surface of GO. Second, electrostatic attraction exists between oxygen functionalities on GO and positive charges on the surface of PS microgels. In step (2), the PS microgels shrink to significantly smaller sizes, due to the precipitation of PS in water, which is accompanied by crumpling of the smooth GO sheets. Consequently, wrinkling of GO sheets perpendicular to the shrunk gel surface are forced to form during shrinkage in water, and large amounts of mesopores are created in the gap of neighboring GO wrinkles. Finally, the PS templates are removed by an annealing treatment to produce 3D, hierarchical, macro/mesoporous RGO materials. While use of PS microgels for template synthesis is not new, to the best of our knowledge, this is the first study that utilizes different solvents to swell and shrink PS microgels wrapped with GO sheets to fabricate macro/mesoporous RGO materials. In principle, 3D properties of the macro/mesoporous RGO materials can be tuned by changing the properties of PS microgels.

2.3.2 Emulsion Polymerization Process of PS

Emulsion polymerization is a type of free-radical polymerization that starts with a monomer, an initiator, and a surfactant in water phase. Monomers are unsaturated, small molecules with active double carbon-carbon bonds. One of the double bonds of initiators can easily crack to form free radicals during reactions initiated by heat or light irradiation. Polymer

chains can be grown by successive addition of the free-radical monomers that serve as building blocks. In our system, AIBA is used as the initiator. In the first step, two radicals were created from even cracking of one AIBA molecule. In the second step, radicals are transferred from AIBA to the monomer units present. Since one end of AIBA radical is positively charged, it can also serve as a surfactant for stabilizing the polymer chains formed in the water phase during emulsion polymerization. Basically, small droplets of monomers (in the oil phase) were formed by an aggressive stirring process in water. The monomers were then attacked by AIBA radicals resulting in a link between the two; meanwhile the growing polymer chains were emulsified by the charge of AIBA to form nano-sized PS in the water. These PS are typically ~220 nm in size as verified by SEM (Figure A1), and are composed of many individual polymer chains. Coagulation of spheres was inhibited due to electrostatic repulsion; the whole process is schematically illustrated in Figure 2.3. The emulsion polymerization was carried out in a batch reactor to ensure that PS were produced at high polymerization rates with high monomer conversion. By contrast, in bulk and solution free-radical polymerization, there is a tradeoff between monomer conversion and polymerization rate.

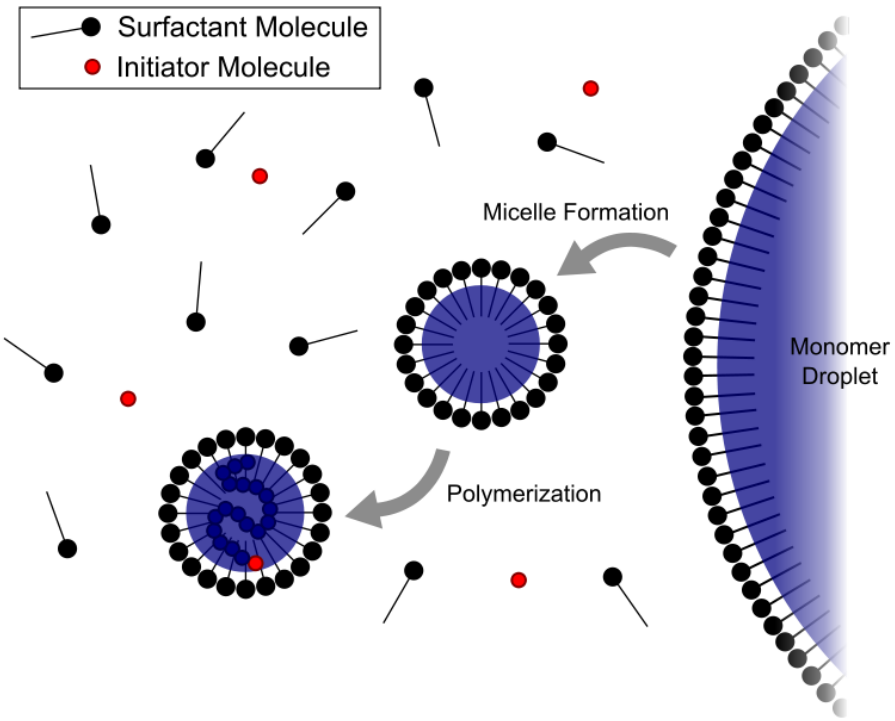

Figure 2.3 Schematic illustration of common mechanism of emulsion polymerization.

Our PS is formed by linking four different types of monomers, namely MMA, GMA, BA, and DVB. MMA is the main monomer on the polymer chain with ~90% content in weight. The epoxy groups on GMA provide the reaction spots with NH_2 groups on GO-NH_2. Unlike hard monomer MMA, BA is a type of soft monomers; therefore, poly (butyl acrylate) (PBA) shows very low glass transition temperature (Tg) of -49 °C, which makes the polymer chains slightly soft and flexible. DVB used in our study serves as a cross-linker since it has an extra carbon-carbon double bond that can link linear polymer chains with other neighboring chains to form a cross-linked 3D network. Thus, our PS shows a cross-linked structure with the degree of crosslinking controlled by adjusting the amount of DVB added. The chemical structure of monomers and cross-linked PS are shown in Figure 2.4.

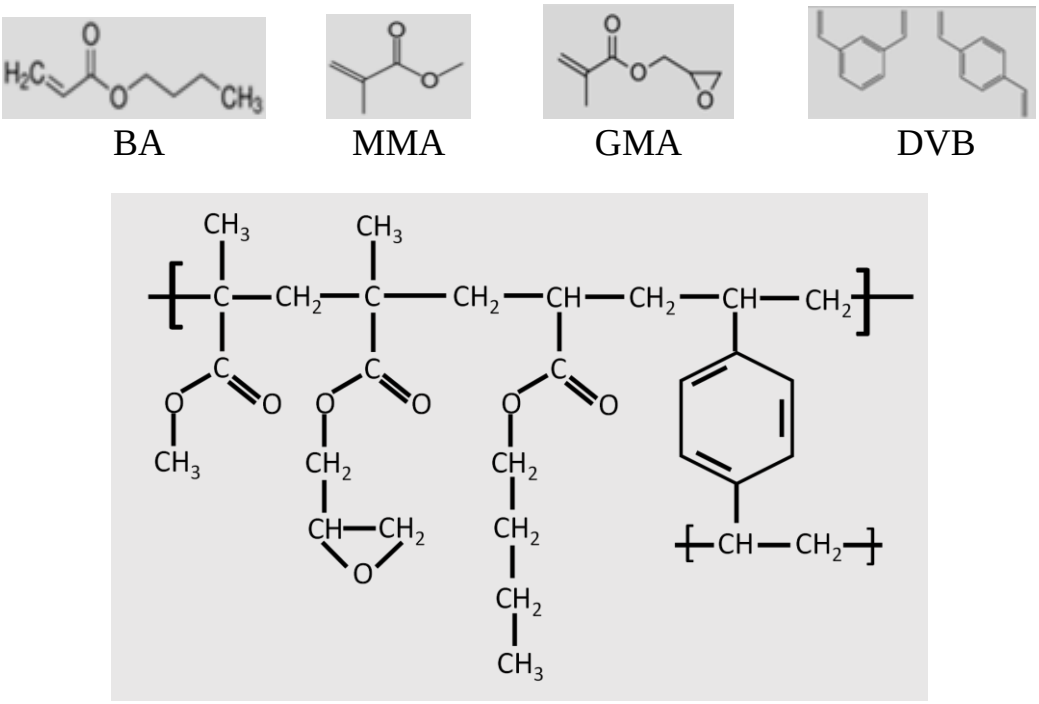

Figure 2.4 Molecular structures of monomers used for synthesis of cross-linked P (MMA-GMA-BA) spheres and the molecular structure of P (MMA-GMA-BA) spheres.

The IR spectrum of as-synthesized P (MMA-GMA-BA) is shown in Figure 2.5. All characteristic IR bands corresponding to poly (methyl methacrylate) (PMMA) segments are identified using data in the literature[88, 89]. Because GMA and BA have similar molecular structures to MMA, most of the characteristic peaks for poly (glycidyl methacrylate) (PGMA) and poly (butyl acrylate) (PBA) segments overlap with the spectrum of PMMA segments[90, 91]. The two bands at 2,997 cm^{-1} and 2,952 cm^{-1} are attributed to the C-H bond stretching vibrations of $-CH_3$ and $-CH_2$ groups, respectively. The strong band at 1730 cm^{-1} shows the presence of the acrylate carboxylic group. Absorption bands from 1395 cm^{-1} to 1450 cm^{-1} originate from $-CH_3$ and $-CH_2$ deformation vibration, while at 1150 cm^{-1}, C-O-C stretching vibration can be observed. The distinct absorption peak at 908 cm^{-1} is attributed to the epoxy group stretching of PGMA[90], confirming successful copolymerization of PGMA. The epoxy groups introduced on the surface

of P (MMA-GMA-BA) spheres are capable of linking with the NH_2 groups on GO sheets via ring-opening reaction.

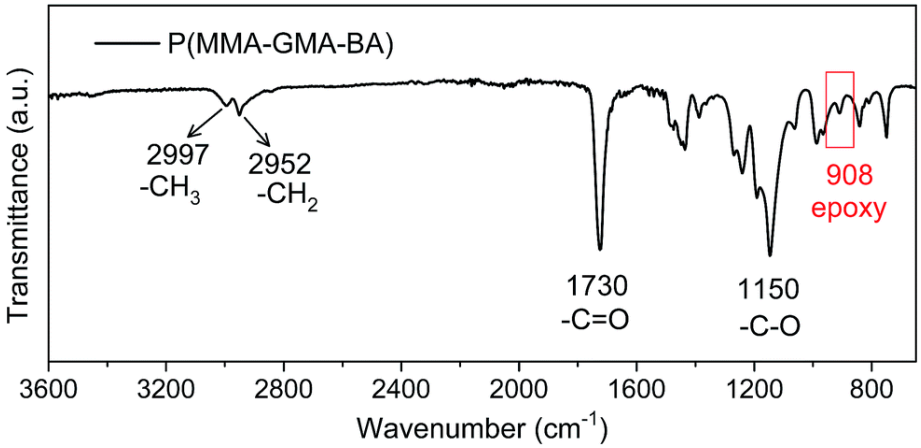

Figure 2.5 FT-IR spectrum of as-synthesized P (MMA-GMA-BA) spheres (0.1wt% DVB).

2.3.3 Swelling-Shrinking Process of PS

PS synthesized with 0, 0.1, and 0.5 wt% DVB, and their corresponding PS/NMP dispersions are labeled as samples A1, A2, and A3 in Figure 2.6, respectively. DVB is an active bifunctional monomer with two C=C double bonds in one molecule, which can link linear polymer chains to form a 3D network structure. As shown in Figure 2.6, uncross-linked PS will dissolve in NMP to form transparent homogenous P (MMA-GMA-BA) solution. In the case of slightly cross-linked PS (0.1% DVB), a translucent dispersion of microgel is observed. The difference in refractive index between microgel and solvent decreases, because a large quantity of solvent molecules are absorbed into the microgel, which may cause the opaque solution of PS to become translucent. For highly cross-linked PS (0.5% DVB), the higher cross-link density limited the swelling of the microgel with less solvent absorbed into it, and as a consequence, the PS (0.5% DVB) microgel remained opaque.

The average size of the PS microgel (0.1wt% DVB) was evaluated using DLS technique. Nanoparticles in suspension undergo random thermal motion (Brownian motion). Smaller particles move faster than the larger ones. In DLS testing, laser was used to hit those particles first, and then scattering laser signal will be recorded. Since those particles undergoing Brownian motion, intensity of the scattered laser fluctuates over time. The distance between the particles in the suspension is also constantly changing with time. There is either constructive or destructive interference of scattered laser between neighboring particles; the recorded information contains the time scale of movement of the particles. The dynamic information of particles is derived from the second order autocorrelation function (G^2 (delay time)) of the intensity trace generated during DLS testing, as shown in Figure 2.7b. By fitting the G^2 (delay time) curve, an average translational diffusion coefficient, D_t, can be calculated. The hydrodynamic size of particles was determined by the Stokes-Einstein equation ($D_h = k_B T/3\pi\eta D_t$) where D_h is the hydrodynamic diameter (or particle size), D_t is the translational diffusion coefficient, k_B is Boltzmann's constant, T is thermodynamic temperature, and η is dynamic viscosity.

The average hydrodynamic diameter of the microgel is 623 nm while that of as-syntheisized PS (0.1 wt% DVB) is 256 nm (Figure 2.7a). Diameters obtained by DLS are usually larger than those observed in SEM or TEM images, because DLS measures the hydrodynamic radius of particles in the large-size end of the size distribution in the laser beam path and the solvent molecules may be clustered around the particle, forming a solvation shell around the sphere.

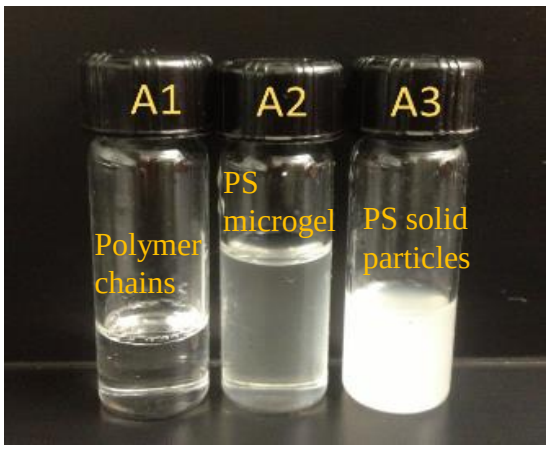

Figure 2.6 Picture of PS /NMP dispersions (0.02g/ml) for PS synthesized with 0, 0.1, and 0.5 wt% DVB shown as sample A1, A2, and A3, respectively.

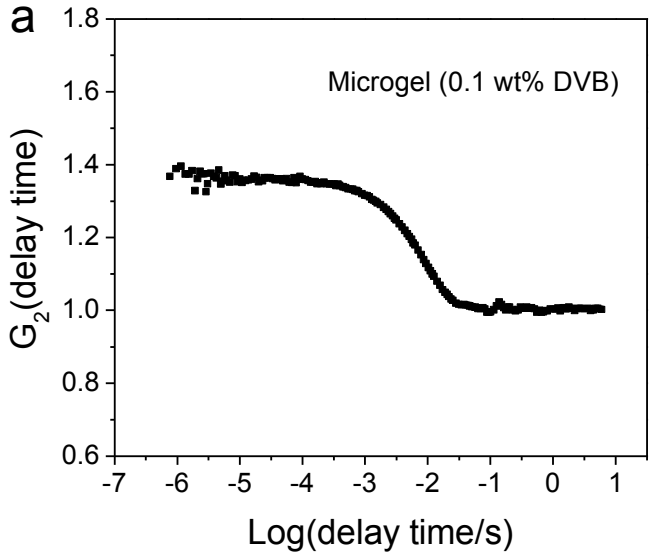

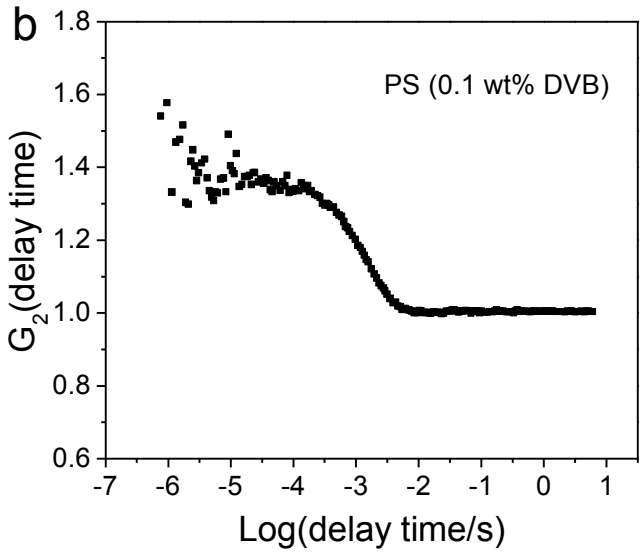

Figure 2.7 (a) Correlation function G^2 (t) measured by DLS on the diluted PS/water dispersion at 25 ˚C (b) Correlation function G^2 (t) measured by DLS on the diluted microgel/NMP dispersion at 25 ˚C.

2.3.4 Characterization of GO and GO-NH_2

Using Hummer's method, functional groups such as COOH, OH and epoxy can be inserted into the graphite interlayer structure, and thus increase the distance between each graphitic layer, which makes the exfoliation of GO sheets directly from graphite possible, as shown in Figure 2.8. The epoxy groups on GO surface reacts with NH_4^+ in ammonia solution, resulting in grafting of NH_2 groups onto GO surface (Figure 2.9). The existence of functional groups results in more disorder in the sp2-graphene structure, which facilitates alloying of lithium ions with GO since lithium ions prefer to insert into defect sites on the GO surface. The Raman spectra of GO and GO-NH_2 in Figure 2.10 show an increase in the intensity ratio of D- and G-bands (I_D/I_G); the I_D/I_G increases from 0.81 for GO to 0.99 for GO-NH_2, most likely indicate the creation of more defect sites due to intercalation of N atoms in the carbon structure of GO[92]. Further comparison of the Raman spectral features reveals the G-band for GO at 1593

cm^{-1} is shifted to 1600 cm^{-1} for GO-NH_2, a phenomenon attributed to the successful amination of GO[93-95].

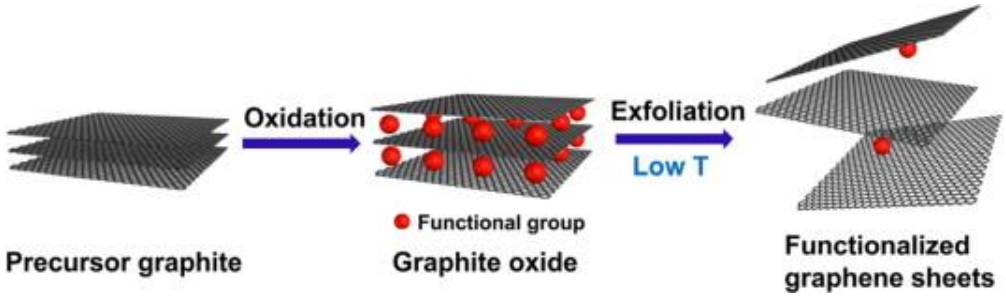

Figure 2.8 Functionalization of graphene surface by Hummer's method[96]. Reprinted by permisssion from M.H. Jin, H.K. Jeong, T.H. Kim, K. P. So, Y. Cui, W. J. Yu, E. J. Ra and Y. H. Lee, *Journal of Physics D : Applied Physics*, 2010,43 (27), 275402.

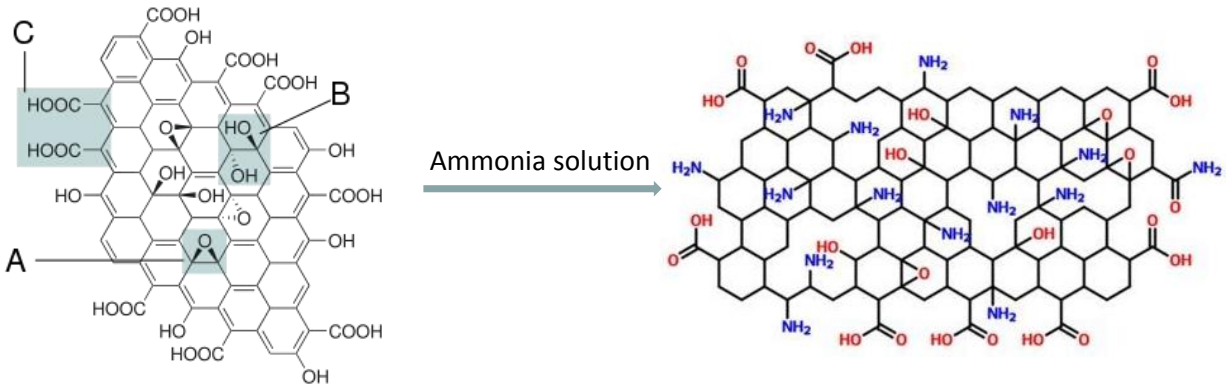

Figure 2.9 Introduction of NH_2 group on GO surface via reaction with ammonia solution[97]. Source from Ossila Ltd.

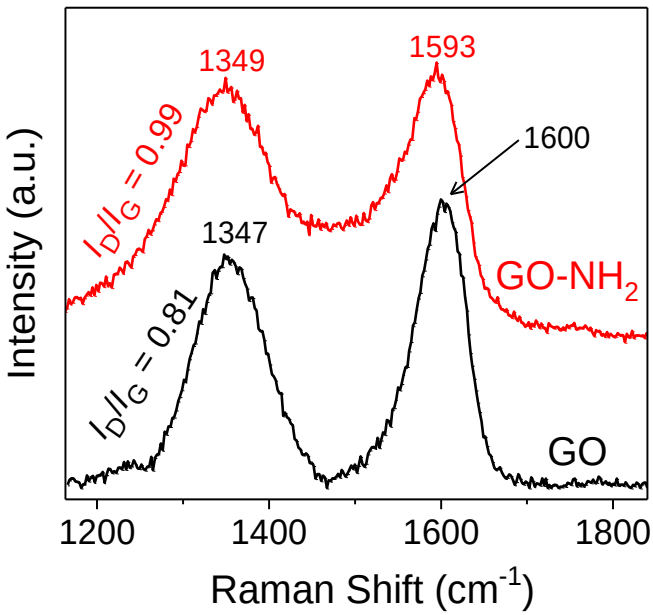

Figure 2.10 Raman spectra of GO and GO-NH$_2$

Incorporation of amino groups onto the GO surface was also probed by XPS. Figure 2.11 shows XPS survey and high-resolution C 1s and N 1s scans of GO and GO-NH$_2$. A distinct signal of N is observed only at a binding energy of 400 eV in the survey scan of GO-NH$_2$ (Figure 2.11a). C 1s XPS spectra show a significant decrease in the C-O bond peak at approximately 286.7 eV after the amination reaction (Figure 2.11b), due to the reduction in the content of oxygen-containing functional groups on GO[98]. The N 1s spectrum (Figure 2.11c) is characterized by a broad peak located at a binding energy of ~400 eV, which is related to the two different nitrogen functionalities including NH_4^+ and NH_2 bonded to GO[99]. To confirm the existence of GO-NH$_2$ bond, XPS spectra were collected for GO-NH$_2$ after ion exchange treatment for three days with HCl (pH=1) to replace NH_4^+ with H^+ . The GO-NH$_2$/HCl aqueous solution was repeatedly washed and centrifuged with distilled water until HCl was completely removed and GO-NH$_2$ sheets could form a highly stable dispersion in water. We emphasize the XPS survey scan of GO-NH$_2$ still showed a distinct N 1s peak after completely removing NH_4^+. Since the

reaction between the ammonia solution and GO was performed under low temperature (~60°C), it is highly unlikely that the doping of N in the carbon-skeleton ring of GO occurred. As shown in Figure 2.11d, the N 1s spectrum can be fitted with two components: first peak component at 399.6 eV that is attributed to C-NH_2 and produced by ring open reaction between epoxy group of GO and ammonia solution, and the second peak at 401.9 eV that is assigned to NH_4^+ that is ionically bonded to COO^- group. As Figure 2.11d shows, the peak intensity of the component associated with NH_4^+ decreases substantially after ion exchange; however, the peak intensity of NH_2 remains almost the same. We therefore conclude that the N in our synthesized GO-NH_2 is in fact covalently bonds to C, as opposed to ionic bonds between NH_4^+ and COO- species. The N content calculated from XPS data is ~4.5 at%, which is expected to provide additional electrochemically active sites on the surface of GO and further increase the Li storage capacity for porous/wrinkled RGO after annealing treatment[94].

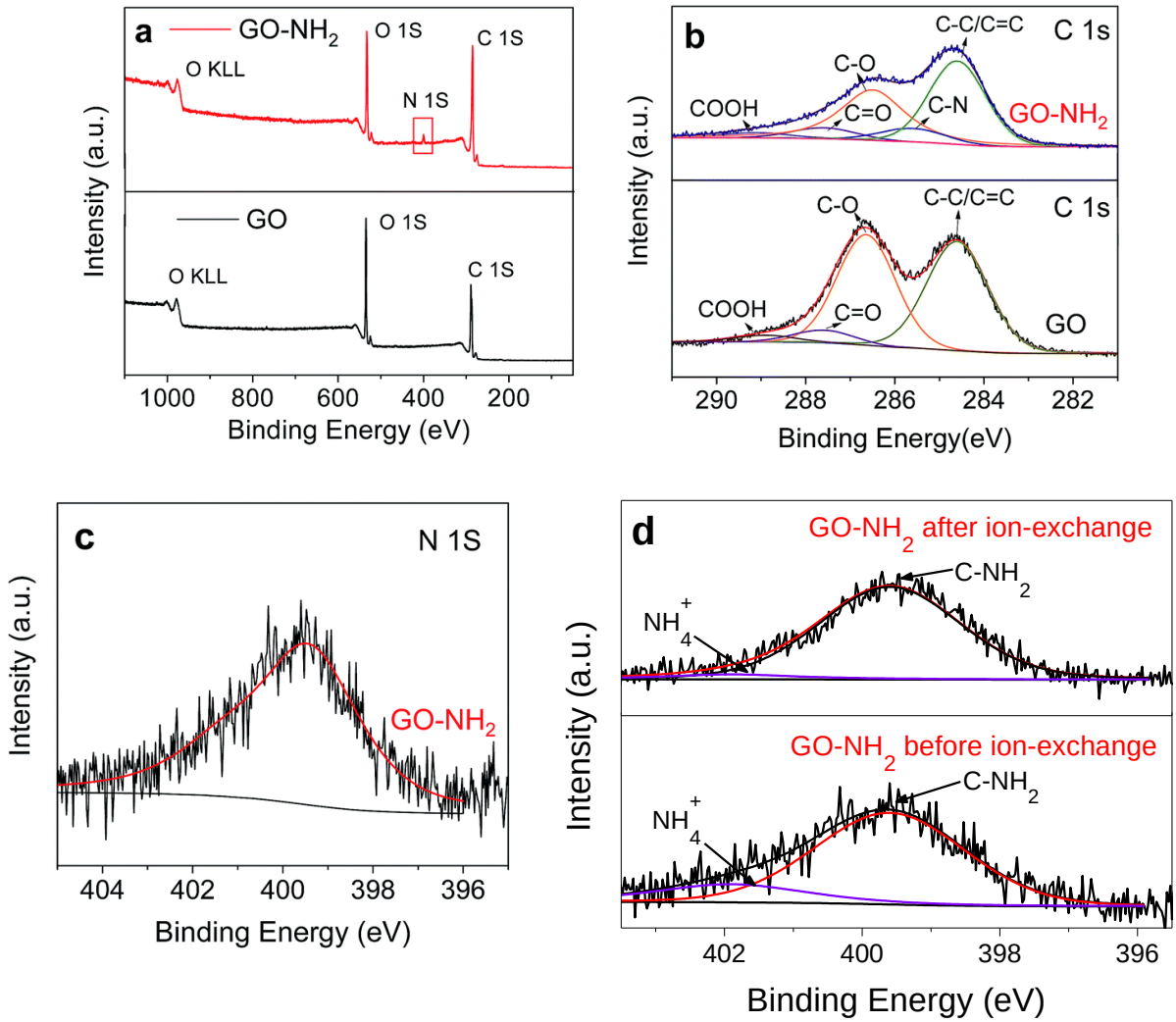

Figure 2.11 (a) XPS survey spectra of GO-NH_2 and GO; (b) C 1s XPS spectra of GO–NH_2 and GO; (c) N 1s XPS spectrum of GO-NH_2; and (d) N 1s XPS spectrum of GO–NH_2 before and after ion exchange.

2.3.5 Size Control of PS and GO-NH_2

As discussed above, GO sheets are produced by oxidizing graphite, a process that requires concentrated acid-treatment and long reaction time. This approach has some drawbacks: the size of the resulting GO sheets is poorly controlled and the process, which usually involves repeated series of oxidation, is dangerous and inefficient. In this case, the size of GO-NH_2 is fixed around 0.2-1.2 μm in length or width with most of the sheets < 550 nm, as shown in Figure

2.12. In comparison, controlling the size of PS is easier as it can be achieved by adjusting the usable amount of charges of AIBA on the spheres. NaCl is used to neutralize the charges of AIBA. To maximize the wrapping effect, we used polymer spheres with average diameter of ~ 220 nm (see size distribution in Figure 2.13) as confirmed by SEM images (Figure A.1). The resulting swollen microgel has an average diameter of ~623 nm as discussed previously. We are currently synthesizing polymer spheres of different sizes. Figure A.2 shows examples of one polymer bulk (NaCl: 0.012 g/ml) and two polymer spheres with diameters of ~970 nm (NaCl: 0.002 g/ml) and ~360 nm (NaCl: 0.0003 g/ml). Adding NaCl into the emulsion system can largely decrease the repelling force between each sphere and thus cause coagulation of spheres (Figure A.2a) and increase volume of spheres (Figure A.2b and c). This result confirms that AIBA behaves not only as an initiator but also as a surfactant for the emulsion polymerization system. Wrapping GO on spheres of different sizes can lead to 3D RGO structures of different porosity via the radius of curvature effect. A major reason the smallest polymer spheres (220 nm) have been used in the current study is based on our hypothesis: the smallest diameter spheres will generate bigger GO wrinkles due to the increased curvature. Note that the size of GO–NH_2 is around 0.2–1.2 μm, which matches well with that of the PS microgel that has a size of 623 nm, and can thus facilitate the assembly of GO on the surface of a microgel.

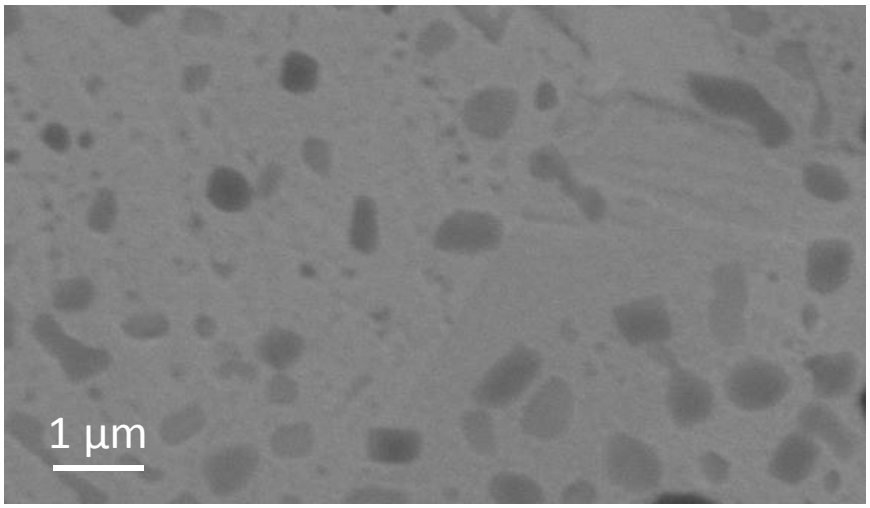

Figure 2.12 SEM image of GO-NH_2 flakes.

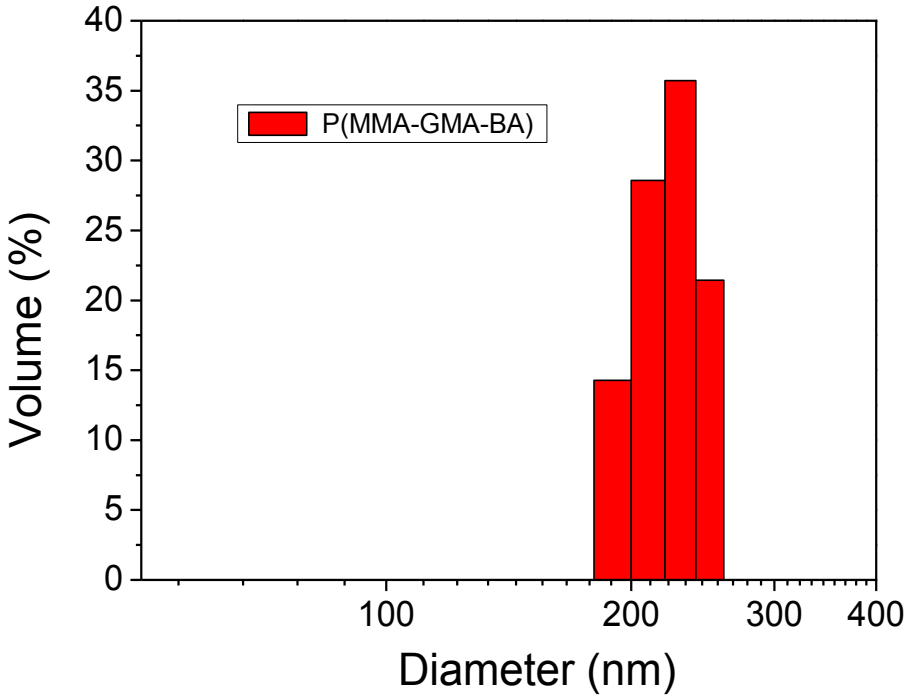

Figure 2.13 Particle size distribution of as-synthesized PS (0.1 wt% DVB)

2.3.6 Surface Morphology for GO@PS with/without Swelling-Shrinking Process

Figure 2.14a shows representative SEM images of the highly uniform, uncoated as-synthesized PS (0.1 wt% DVB) with smooth textures and an average diameter of 220 nm. SEM and TEM images reveal the difference in the surface properties of GO-wrapped as-synthesized PS (Figure 2.14b and d) and wrinkled GO@shrunk PS (Figure 2.14c and e). Figures 2.14b and d indicate the surface of the as-synthesized PS was coated by relatively smooth untextured GO sheets. In contrast, Figures 2.14c and e show more wrinkled and roughened textures associated with the shrinking of GO sheets and are encapsulating the PS microgel in water. Furthermore, from TEM images (Figure A.3 and Figure A.4), thicknesses of GO layers wrapping on as-synthesized PS and shrunk PS fall in the range of 5-12 nm and 42-80 nm, respectively. Such differences indicate the successful formation of GO wrinkles for wrinkled GO@shrunk PS. In particular, the wrinkled GO sheets generate numerous mesopores between the neighboring wrinkles that enhance the surface area.

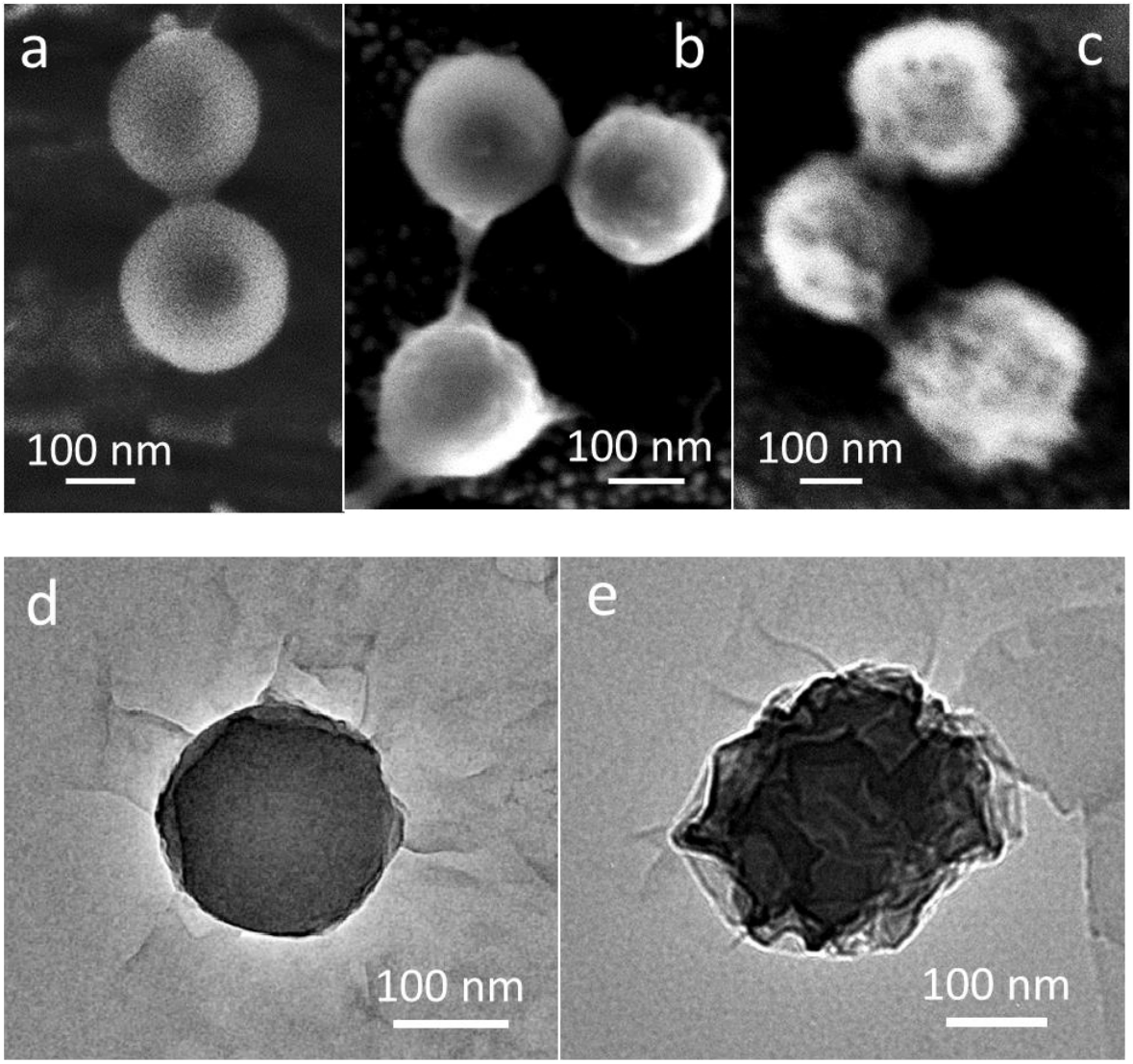

Figure 2.14 (a) SEM image of as-synthesized PS (0.1wt% DVB); (b) and (d) SEM and TEM images of GO wrapped as-synthesized PS (0.1wt% DVB) with smooth GO surfaces, respectively; and (c) and (e) SEM and TEM images of wrinkled GO@shrunk PS with wrinkled GO surfaces, respectively.

As revealed by the SEM images (Figure 2.15a), wrinkled/porous RGO electrodes are characterized by deflated hollow-pore structures with intact and continuous walls after annealing treatment. Thermal stability of the core PS was analyzed by TGA (Figure 2.16) and results reveal that PS starts to degrade at 280 °C and fully decomposes at 430 °C, after ~2.5 hours of annealing in N_2 flow. Average size of the deflated pore structures is approximately 200 nm, which can

provide a suitable contact area with electrolytes and ions. For purpose of comparison, the paper-like stacked RGO material is presented in Figure 2.15b. No obvious macropores (diameter > 50 nm) are observed in the stacked RGO sheets.

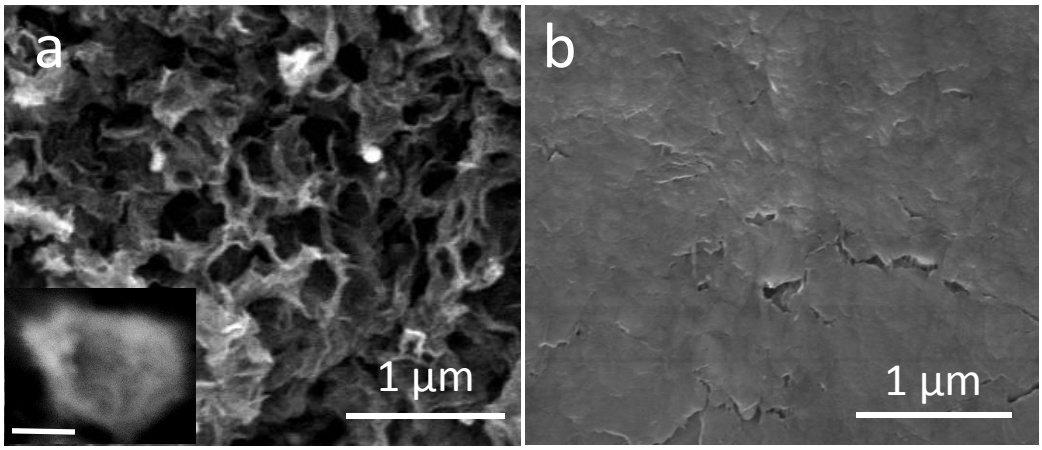

Figure 2.15 (a) Low-magnification SEM image of porous/wrinkled RGO after annealing treatment; the inset shows an image of wrinkled GO@shrunk PS before annealing treatment (scale bar =150 nm). (b) Low-magnification SEM image of stacked RGO sheets.

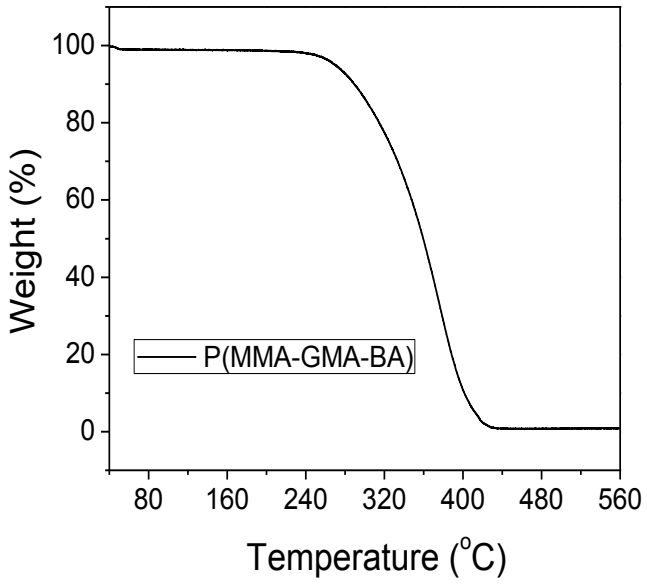

Figure 2.16 Weight loss vs. temperature curve by TGA analysis of cross-linked P (MMA-GMA-BA) microspheres (0.1wt%DVB).

The structural difference was further confirmed by nitrogen adsorption/desorption data of porous/wrinkled RGO and stacked RGO (Figure 2.17). Although the specific surface area of porous/wrinkled RGO is smaller (276 m^2 /g) than that of single-layer graphene sheets (2630 m^2 /g)[100], it is still larger than that of stacked RGO (96 m^2 /g). Note that since electrodes with high surface areas normally induce high irreversible capacities during the first charge/discharge cycle, optimum surface area for a high-performance electrode may be far less than the theoretical surface area of graphene. The porous/wrinkled RGO presents a characteristic type IV isotherm according to the IUPAC classification, with a pronounced hysteresis at P/Po = 0.45 – 0.96, suggesting the existence of high number of mesopores (2–50 nm) in porous/wrinkled RGO sample[101]. Additionally, the hysteresis suggests the occurrence of irreversible chemical adsorption in the mesopores[102], which is usually associated with capillary condensation in the pores.

The average pore diameter of porous/wrinkled RGO is roughly 3.9 nm calculated by the nonlocal density functional theory (NLDFT) method. NLDFT is designed for adsorption and capillary condensation in capillary pores and provides an accurate estimation of the porous structure of nanoporous materials[103]. The PSDs obtained from the NLDFT model confirm that porous/wrinkled RGO has micropores and a higher number of mesopores than stacked RGO. In addition, the higher degree of mesoporosity of porous/wrinkled RGO is supported by the specific surface area data in Table 2.1. Note that the pore volume increased for porous/wrinkled RGO in comparison to stacked RGO (Table 2.1), indicating that swelling/shrinking treatment may in fact be contributing to the observed wrinkling, and thus playing a central role in micro/mesoporosity of porous/wrinkled RGO. As shown in the PSDs (Figure 2.18), stacked RGO shows a sharp peak at 3.9 nm, while after swelling/shrinking treatment, a new peak appears at ~1.9 nm for

porous/wrinkled RGO. The full-width at half-maximum (FWHM) of the peak at 3.9 nm increases due to the peak shoulder at 2.9 nm, suggesting that the mesopores formed by the big ripples on stacked RGO were shifted to smaller wrinkles or smaller micro/mesopores. The mesopores may be generated in the process of thermal treatment of wrinkled GO@shrunk PS by the spaces between RGO nanosheets[80] and wrinkled GO walls of the macropores.

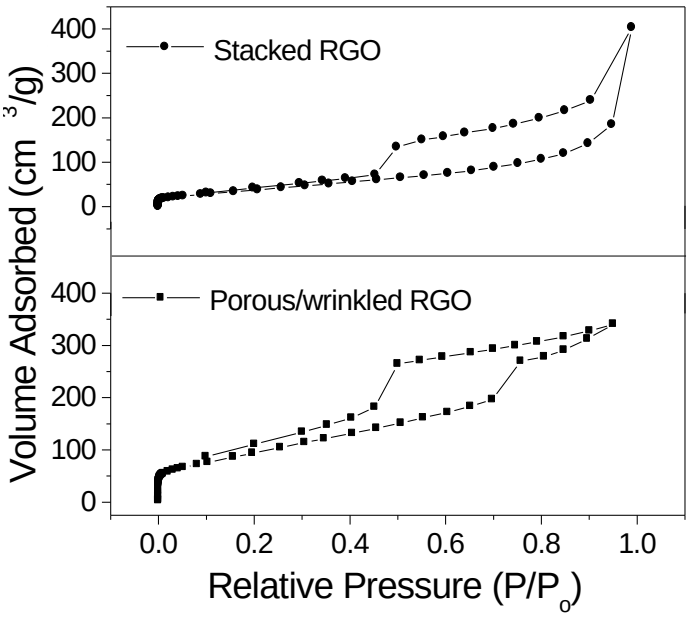

Figure 2.17 Nitrogen adsorption-desorption isotherms of porous/wrinkled RGO and stacked RGO.

Table 2.1 Summary of textural properties of stacked RGO and porous/wrinkled RGO obtained from physisorption.

Sample	Stacked RGO	Porous/wrinkled RGO
SSA, m^2/g	96	276
V (2< pore size <10 nm), cm^3/g	0.27	0.39
V (pore size <2nm), cm^3/g	~0	0.0043

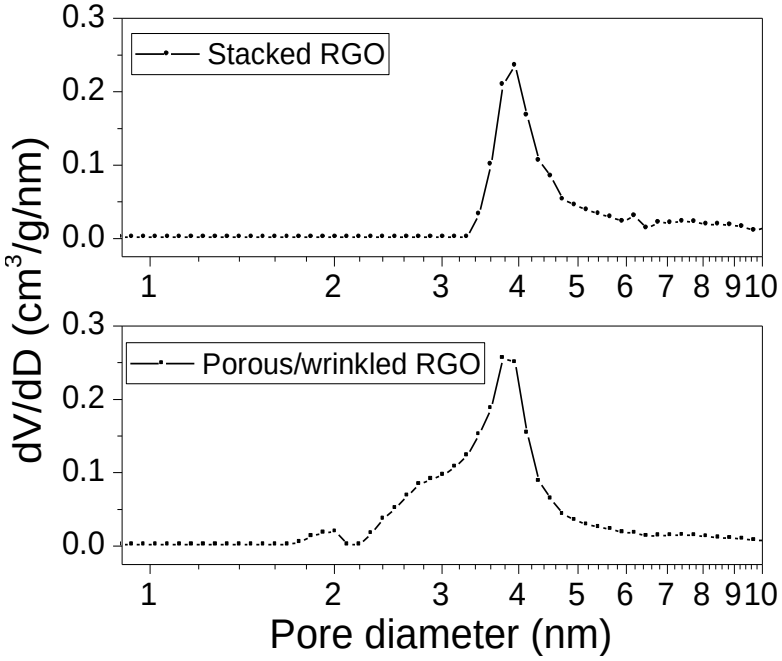

Figure 2.18 Pore size distribution modeled by non-local DFT (NLDFT) method for porous/wrinkled RGO and stacked RGO.

In addition, the difference in microstructure between stacked and wrinkled RGO was investigated by XRD (Figure 2.19). For stacked RGO, the sharp (002) diffraction peak at 2θ of 24.7° suggests the layered RGO sheets formed an organized crystal structure that is analogous to the standard 002 diffraction peak for graphite with a *d*-spacing of 0.336 nm. After swelling/shrinking treatment with PS microgel, porous/wrinkled RGO showed a broad (002) diffraction peak around 2θ of 25.6°, whereas the full-width at half-maximum (FWHM) for stacked RGO and porous RGO were 6.21 and 9.30, respectively. The broadened FWHM indicate that porous/wrinkled RGO are composed of a higher number of smaller wrinkles than stacked RGO. The *d*-spacing at (002) of stacked RGO and porous/wrinkled RGO were 0.348 nm and 0.361 nm, respectively. Coherence length at (002) calculated by momentum transfer of 2θ were 0.924 nm for porous/wrinkled RGO and 1.396 nm for stacked one, corresponds to the number of graphene sheets in the domains. Both *d*-spacing and coherent length reflect smaller wrinkles of

porous/wrinkled RGO that partly inhibits the complete stacking of RGO sheets and thus results in less organized crystal structure than stacked RGO.

The hierarchical porous/wrinkled RGO with macro/mesoporous channels is favorable for fast Li-ion diffusion from different orientations, and is more accessible to Li-ion intercalation / insertion sites created by open pores and wrinkles. We conclude the synthesized wrinkled GO@shrunk PS material has the ability to generate 3D hierarchical architectures that could serve as excellent anode materials in LIBs after the removal of the core PS.

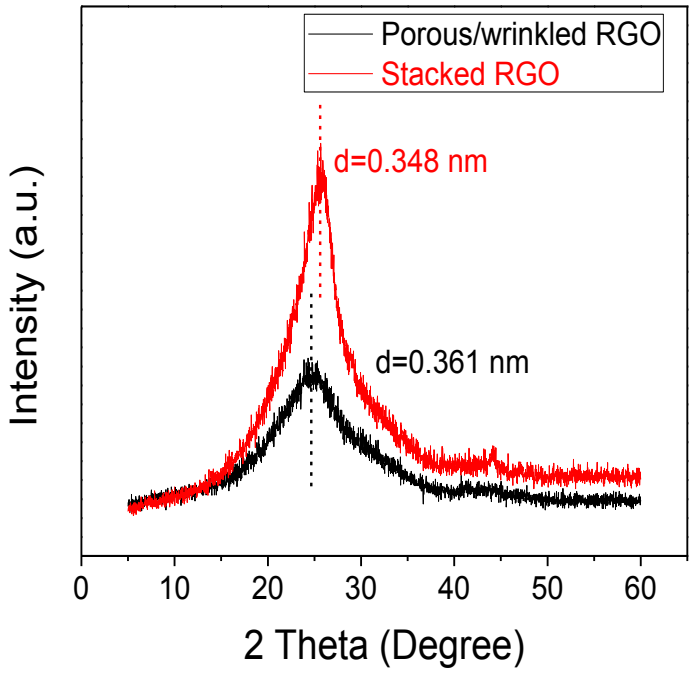

Figure 2.19 XRD patterns of stacked RGO and porous/wrinkled RGO.

2.4 Electrochemical Properties of Porous/Wrinkled RGO Anode

Figure 2.20a shows cyclic voltammetry (CV) curves of porous/wrinkled RGO between 0.002 and 3.000 V at a scanning rate of 0.1 mv/s. The first cycle reduction peak is located at very low potential, ~0.1 V. In subsequent cycles, the CV profiles were almost identical, which

demonstrates structural integrity of the porous/wrinkled RGO electrodes is well maintained during charge-discharge cycles[104]. Figure 2.20b shows typical discharge/charge voltage profiles of porous/wrinkled RGO anodes at the 0.2C rate (1C = 372 mA/g) between 0.002 V and 3.000 V. For the initial discharge curve, the potential drops rapidly and a sloping plateau appears around 0.6 V. The second to fourth dischargecharge curves lack obvious plateaus, which corresponds to various intercalation compounds such as Li_7C_{14} to $Li_{18}C_{24}$, rather than the commonly reported LiC_6 for graphite electrodes[104]. More Li-ions can access defect sites of graphene during cycling[105]; the presence of significant amounts of N-doped defect sites in our synthesized porous/wrinkled RGO anodes is expected to enhance Li intercalation. Cycling performance of the porous/wrinkled RGO anodes, measured at 0.2C for 200 cycles, is shown in Figure 2.20c. The first discharge and charge capacities were 1240 and 750 mAh/g, respectively. After 200 cycles, the reversible capacity was stabilized at approximately 720 mAh/g, delivering almost 100% Coulombic efficiency. The high capacity of the porous/wrinkled RGO is attributed to curled walls and macro/mesopores of RGO structure. A previous study[106] suggested the capacity exhibited below 0.5 V (vs. Li/Li^+) is from Li intercalation into the graphene layers, while the capacity above 0.5 V is ascribed to the Faradic capacitance on the surface or on the edge sites of RGO sheets. Moreover, porous/wrinkled RGO exhibited impressive rate performance (Figure 2.20d)[92, 99, 105, 106]. Even at very high discharge-charge rates (20C and 30C), the anode still delivered ~160 and ~80 mAh/g, respectively. In particular, when the current rate was decreased back to its initial value of 2C after a total of 25 cycles, the reversible capacity was still retained at 490 mAh/g. Successful fabrication of porous/wrinkled RGO for LIB anodes via microgel-assisted assembly is evident from the excellent electrochemical behavior as shown in Figure 2.20.

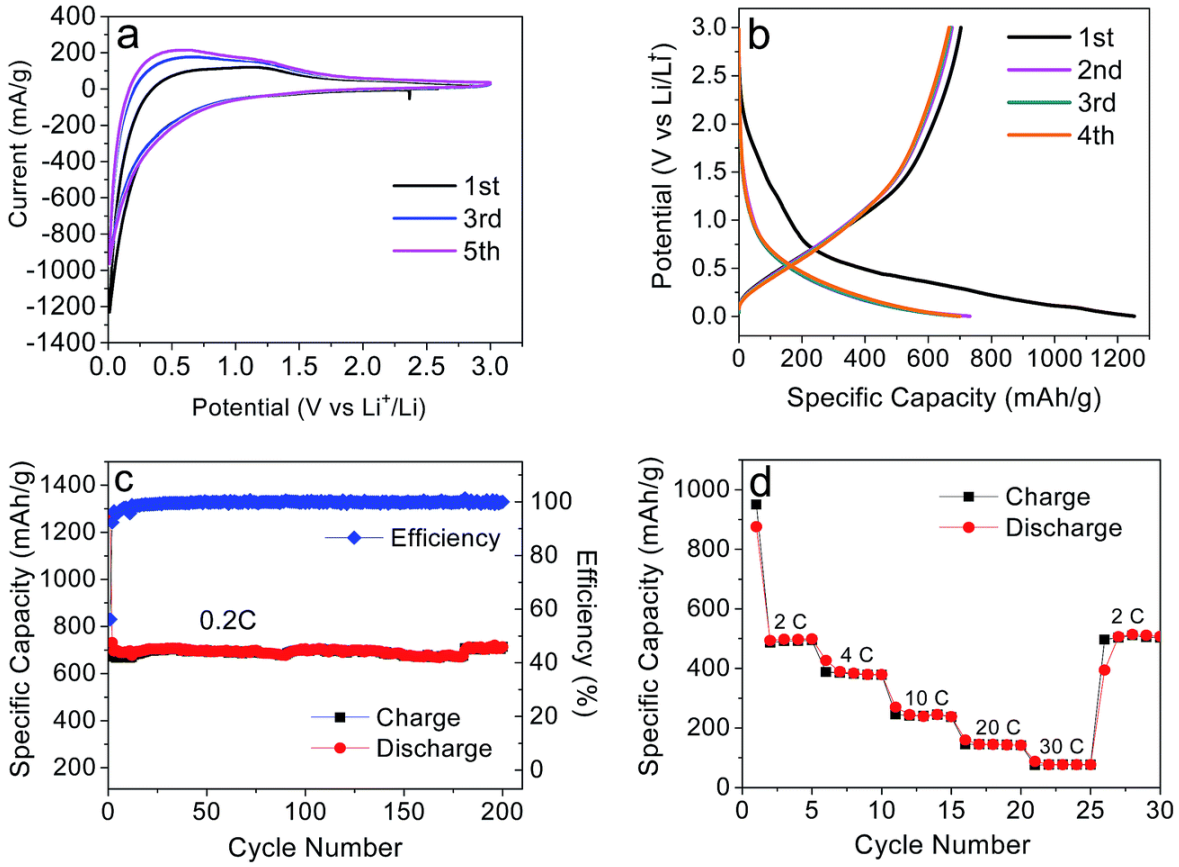

Figure 2.20 (a) Cyclic voltammograms (CV) of porous/wrinkled RGO. (b) Galvanostatic charge-discharge profiles of porous/wrinkled RGO at a current rate of 0.2C. (c) Cycle performance and Coulombic efficiency of porous/wrinkled RGO at a current rate of 0.2C. (d) Rate capability of porous/wrinkled RGO cycled at different current rates (2C, 4C, 10C, 20C, 30C, and 2C).

To highlight the superiority of our unique porous/wrinkled RGO materials, we tested the samples at a current rate of 4C. For comparison, stacked RGO anodes were also investigated under the same conditions and results are presented in Figure 2.21a. Apparently, a porous/wrinkled RGO anode demonstrates a noticeably higher reversible capacity than a stacked RGO anode, with a stable reversible capacity of 400 mAh/g even after 200 cycles. As expected, the porous/wrinkled RGO anode exhibits an extremely durable rate capability, as displayed in Figure 2.21b. In contrast, the stacked RGO anode shows a significantly lower rate capability (Figure 2.21b). The electrode performance (Figure 2.21b) is consistent with the N_2 physisorption

data in Figure 2.17, which shows a lower surface area for stacked RGO in comparison to porous/wrinkled RGO. The low surface area of stacked RGO is expected to result in a decrease in the number of sites for Li-ion insertion and as a consequence, a lower reversible capacity than that of porous/wrinkled RGO. In addition, the pore size distributions (PSDs) of stacked RGO and porous/wrinkled RGO (Figure 2.18), modeled by the DFT method, are in the same mesopore range and centered around 3.9 nm even though, the former lacks macropores and a wrinkled structure. We emphasize the mesopores in stacked RGO exist mainly in the interlayer space formed between RGO sheets in the dense RGO layered structure, and, as revealed by the cycling data in Figure 2.21, do not facilitate high rate capability. On the other hand, in addition to abundant mesopores including smaller pores centered ~2.0 nm (Figure 2.18), presence of abundant macropores in the porous/wrinkled RGO anode has the benefit of facilitating diffusion of electrolyte and Li-ions from macropores to their connected mesopores with shorter transport distance in comparison to a stacked RGO anode.

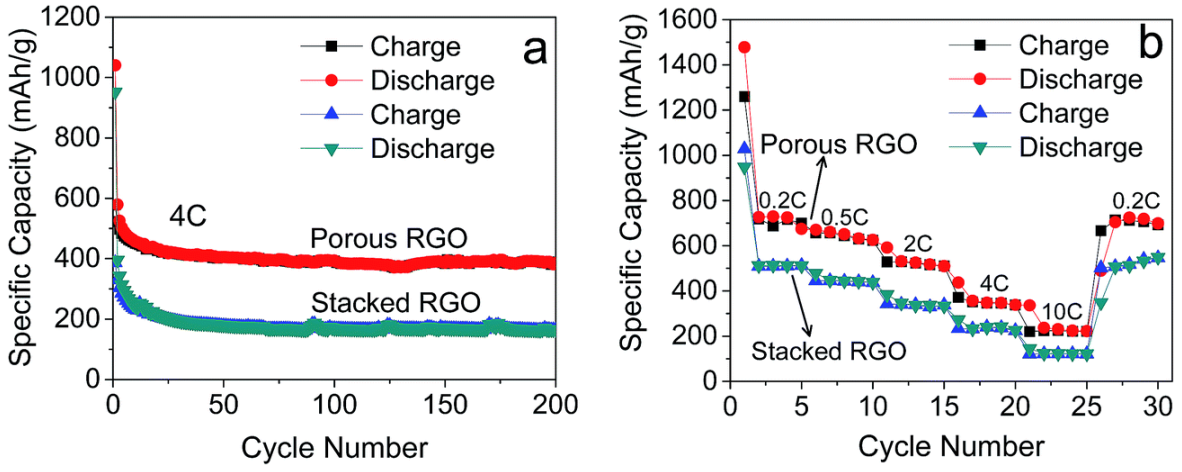

Figure 2.21 (a) Comparison of cycle performance of porous/wrinkled RGO and stacked RGO cycled at a current rate of 4C. (b) Comparison of rate capability of porous/wrinkled RGO and stacked RGO cycled at different current rates (0.2C, 0.5C, 2C, 4C, 10C, and 0.2C).

As shown in Table 2.2, the Li storage capacity of our hierarchical porous/wrinkled RGO is higher than most of the reported high-performance pristine and N-doped RGO anodes with different architectures and shapes[80, 85, 102, 105, 107-121].The reversible capacity at low (0.2C) to high (20C) charge-discharge rates for our porous/wrinkled RGO sample falls at the top of all RGO anodes with only N, S-co-doped graphene, and CVD-grown graphene exhibiting superior performance. The superior performance of N, S-co-doped graphene may be due to the combined doping of RGO with N and S, which is associated with improved electronic conductivity and Li electroactivity[107, 111, 118, 122]. It is possible the Li storage capacity of our electrode can be improved further by increasing the dopant concentration. Our microgel-assisted process has advantages over conventional methods listed in Table 2.2. Chemical composition of our PS template is highly flexible as it is synthesized via co-polymerization of various functional monomers, thus allowing for introduction of different dopants; for example, the pyridine monomer used in this study is a good source for high-concentration doping of N. Although CVD-grown graphene shows superior performance[83], we emphasize that unlike the CVD process, the microgel-assisted assembly process has a higher practical application potential due to the advantages of simplicity, scalability, and low cost. We attribute the improved performance of our porous/wrinkled RGO anode to the mesoporous structure generated by the highly wrinkled RGO and the macropores created after removal of the PS template. In particular, the wrinkled RGO structure provides a high surface area that facilitates rapid charge transfer and minimizes polarization effects. In addition, the macroporous structure is favorable for efficient diffusion of Li ions into deep sites in the bulk RGO. An important distinguishing feature of our wrinkled RGO is that the macropore and highly wrinkled RGO sheet properties can be easily tuned via changing the size of core PS. Further, the void that exists between neighboring

wrinkles of RGO could offer a safe region for depositing active electrode materials (metal or metal oxide) and accommodating the large volume changes that typically occur during cycling.

Table 2.2 Comparison of electrode performance of porous/wrinkled RGO in the literature synthesized using a microgel-assisted method and a variety of high-performance carbon, graphene and RGO anodes.

Shape	Materials / architectures	Preparation methods	Current C-rate (/h) / capacities (mA h/g)				Surface area (m^2/g)	Ref.
Sphere	RGO hollow sphere /wrinkled wall	Swell & shrink of polymer template	0.2/730	2/510	10/260	20/160	276	This work
	RGO hollow sphere / ultrathin shell	SiO_2 template	0.27/650	1.34/434	8.07/287	13.44/249	248.3	80
	C hollow sphere / mesoporous wall	SiO_2 template	0.2/600	1/390	5/270	10/200	970	85
	C sphere @carbon black / core-shell	Spray drying	0.13/450	0.27/410	1.34/350	2.7/300	49	110
	N-riched C sphere	SiO_2\ template & N doping	1.34/542	2.7/410	5.4/293	8.07/215	67.4	111
	N, S co-doped RGO hollow sphere	Nickel foam & sulfonated polymer template	1.34/610	2.7/590	5.4/440	26.9/380	70	118
	C hollow sphere / mesporous wall	SiO_2 template & CVD growth	0.2/268	0.5/225	1/189	10/125	771	120
Sheet	Highly porous graphene	CVD growth	1/707	2/650	5/544	20/203	1654	82

	N-doped graphene	Pyrolysis & MgO template	0.27/655	1.34/300	2.7/259	13.44/150	466	102
	Free standing RGO	Freeze-drying	0.54/600	1.34/540	2.7/500	5.4/450	148	109
	Sandwiched RGO@N-doped C	Pyrolysis	0.54/638	1.34/511	5.4/286	26.9/98	327	112
	Folded RGO	Freeze-drying & thermal reduction	0.54/557	1.34/268	2.7/169	4.03/141	--	113
	Free standing holey RGO	Mechanical cavitation-chemical oxidation	0.27/320	0.67/287	2.7/200	5.4/175	15	114
	Mesoporous graphene / 9nm pores	Monomicelle close-packing assembly	0.27/770	0.54/540	1.34/430	13.44/255	281	115
	C fibers grown on graphene	CVD growth	0.2/420	1/329	5/200	10/189	315	116
	Free standing RGO	Photothermal reduction	1/545	5/375	20/240	--	200-300	119
	Sandwiched RGO@ mesoporous C	Self-assembly	0.2/770	1/540	5/370	20/250	910	121
Gel	RGO@melamine–formaldehyde	Freeze-drying	0.27/672	0.54/560	1.1/460	4.03/317	1170	108
Cloth	N-doped C	Cotton cloth template & CVD growth	2.7/500	5.4/369	13.44/183	26.9/110	1890	107
Sponge	Meso & macroporous C	Polystyrene template via mesophase pitch	0.2/470	1/320	5/200	--	170	117

2.5 Conclusion

Hierarchical porous/wrinkled RGO anodes were successfully synthesized utilizing a unique approach involving swelling and shrinking of a polymer template. Selection of solvents plays a critical role in the synthesis of the 3D hierarchical porous RGO. The GO@microgel was first obtained in the "good solvent" (NMP) and then shrunk in a "poor solvent" (water) to obtain wrinkled GO@shrunk PS. During the shrinking process, the outer surface of GO was wrinkled and roughened, resulting in formation of mesochannels on the wrinkled GO@shrunk PS surfaces. The resulting macro/mesoporous and wrinkled RGO anode materials, obtained after annealing of the polymer spheres provided favorable transport kinetics for both Li ions and electrons. As a result, high reversible capacity and durability (720 mAh g^{-1} at 0.2C current rate after 200 cycles), and high rate capability (~160 mAh/g at 20C) were achieved as electrodes of Li-ion cells. Reversible capacity at low (0.2C)-to-high (20C) charge-discharge rates for our porous/wrinkled RGO sample falls at the top of all RGO anodes. Consequently, it is reasonable to conclude the microgel-assisted method demonstrated in this study has the potential of enabling future design of graphene-based electrodes for various energy storage devices.

Chapter 3 - Magnetic Field-Induced Fabrication of Fe_3O_4/Graphene Nanocomposites for Enhanced Electrode Performance in Lithium-Ion Batteries

Chapter 3 is reproduced in part with permission from:

Wang H.; Xie J.; Follettea M.; Back T. C.; and Amama P. B. Magnetic field-induced fabrication of Fe3O4/graphene nanocomposites for enhanced electrode performance in lithium-ion batteries. *RSC Advances* **2016**, 6, 83117-83125.

3.1 Introduction

Among metal oxide active materials, Fe_3O_4 has attracted significant attention because of its low cost, nontoxicity, high corrosion resistance, and high natural abundance. However, Fe_3O_4-based anode materials usually exhibit rapid capacity fading, poor cyclability and limited rate capability due to their low electrical and ionic conductivity as well as their large volume changes during cycling. The use of graphene as an electrode component to overcome the poor cycling performance of Fe_3O_4 is often plagued by the inevitable tendency of the graphene sheets to restack due to the van der Waals interactions of the sheets especially during conversion from graphene oxide (GO) to reduced graphene oxide (RGO), thus reducing its electrochemically active surface area. To overcome these problems, various strategies have been implemented including optimizing the nanoparticle morphology[123, 124] and combining Fe_3O_4 with a nanocarbon material (carbon nanotubes (CNTs), graphene, carbon shells[31, 125-130], *etc.),* or *via* a "double protection strategy" whereby multiple nanocarbons[131] are used to improve the stability and cycling performance of Fe_3O_4.

The use of magnetic field appears to be an effective approach for fabricating high-performance Fe_3O_4/nanocarbon anodes. Zhang *et al.*[132] demonstrated self-assembly of magnetite hybrid paper at the water–air interface, with the help of an external magnet; the resulting Fe_3O_4/RGO hybrid anode showed high reversible capacity with long cyclability. The alignment of Fe_3O_4nanoparticles along the magnetic field lines has also been used to design Fe_3O_4/nanocarbon materials. Using a magnetic field induced solvothermal method, Wang *et al.*[130] synthesized Fe_3O_4/C composite microrods that delivered a stable discharge capacity of about 400 mA h g^{-1} at a high current density of 1000 mA g^{-1}. However, these methods still require conductive additives and polymer binders to maintain the integrity of anode materials during long cycling, which usually complicates the synthesis process and reduces the anode capacity.

In this study, we demonstrate a simple, facile, and scalable approach to fabricate porous wrinkled Fe_3O_4/RGO anodes (W-Fe_3O_4/RGO) that show high reversible capacity, excellent cyclic stability, and better rate capability in LIBs compared to unwrinkled Fe_3O_4/RGO (U-Fe_3O_4/RGO). The W-Fe_3O_4/RGO anodes were prepared by dip coating of Fe_3O_4/RGO solution on a current collector immediately followed by the application of a strong magnetic field and calcination at 550 °C. The exposure to magnetic field induces alignment and folding of RGO sheets along the magnetic field lines and the formation of a porous 3D structure that promote faster electrons and Li ions transport within the electrode and improve the effective surface area of active materials. The W-Fe_3O_4/RGO nanocomposites show promise in resolving the capacity-fading problem associated with Fe_3O_4-based electrodes. To the best of our knowledge, this is the first report that exploits the magnetic properties of Fe_3O_4 for improving the formation of wrinkled RGO nanosheets by exposure to a supermagnet.

3.2 Experimental Section

3.2.1 Synthesis of Fe_3O_4/GO Nanocomposites

GO was synthesized from natural flake graphite by the modified Hummers method[133]. 200 mg of GO was suspended in 200 mL ultrapure water and then sonicated at room temperature for 2 h to form stable GO dispersions. To decorate Fe_3O_4 nanoparticles uniformly on GO sheets, the Fe_3O_4/GO nanocomposites were prepared by an *in situ* chemical method using as-synthesized GO/water dispersion as the precursor. 259.6 mg $FeCl_2 \cdot 4H_2O$ and 708.4 mg $FeCl_3 \cdot 4H_2O$ were added to GO dispersion (70 mL of 1 mg mL^{-1}) at 80 °C under N_2 atmosphere. The blended solution was then stirred for 10 min, quickly followed by addition of 3 mL of 29 wt% ammonium hydroxide. The pH of the final mixture was controlled in the range of 11–12. The reaction was carried out at 80 °C for 30 min under constant mechanical stirring and N_2 gas flow. The as-prepared Fe_3O_4 dispersions were rinsed extensively with ultrapure water and transferred *in situ* to copious amount of ultrapure water to obtain 1.0 mg mL^{-1} Fe_3O_4/GO dispersion.

3.2.2 Preparation of Fe_3O_4–Citric Acid/GO Ethanol Dispersion

20 mg of citric acid was added to 20 mL of the synthesized Fe_3O_4/GO (1.0 mg mL^{-1}) and sonicated at room temperature for 1 h to form coordinate bonds between Fe_3O_4 and citric acid. The as-prepared Fe_3O_4–citric acid/GO was washed with ethanol and then transferred to 20 mL ethanol to form stable Fe_3O_4–citric acid/GO composites that are dispersed in ethanol.

3.2.3 Preparation of Wrinkled Fe_3O_4/RGO Anodes

A piece of copper current collector (9 μm thick) was placed at the center of a round super strong magnet with a maximum pull force of 590 lbs. The as-prepared Fe_3O_4–citric acid/GO dispersion (3–4 mL) was drop cast on the current collector and dried at room temperature. Thereafter, the dried Fe_3O_4/GO was annealed at 550 °C for 2 hours in argon atmosphere to reduce GO to RGO.

The synthesis steps for the wrinkled Fe_3O_4/RGO are illustrated in Figure 3.1. For the purpose of comparison, the unwrinkled Fe_3O_4/RGO electrode was prepared following the same steps except that the sample was not subjected to the magnetic field treatment step.

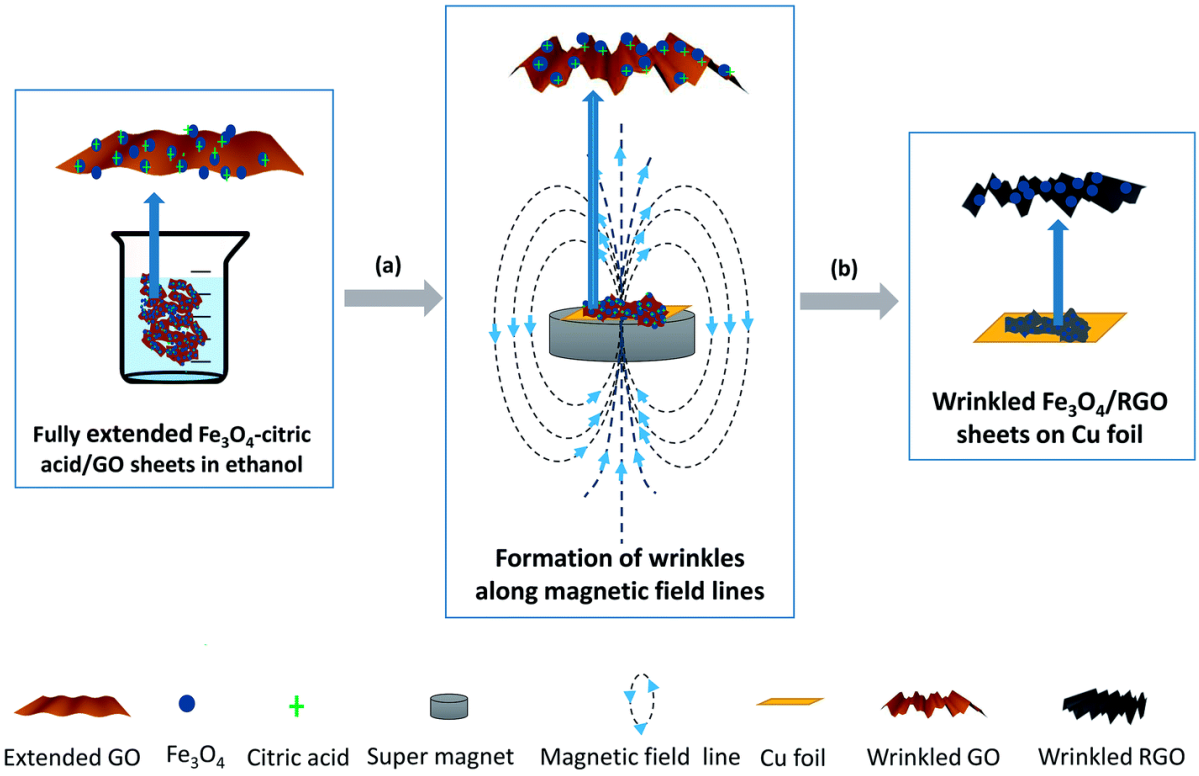

Figure 3.1 Schematic illustration of synthesis of wrinkled Fe_3O_4/RGO anode *via* magnetic field-assisted process followed by annealing in argon. (a) Deposition of Fe_3O_4–citric acid/GO ethanol solution on copper foil by dip coating. (b) Annealing of the wrinkled Fe_3O_4–citric acid/GO anode on copper foil at 550 °C in argon for 2 hours.

3.2.4 Materials Characterization

The XRD patterns were collected on a Rigaku Miniflex II X-ray diffractometer with Cu Kα radiation (λ = 1.5418 Å) at 40 kV and 40 mA. The morphological characterization of the samples was conducted using a field emission scanning electron microscope (FESEM, Hitachi S5200) and a transmission electron microscope (TEM, FEI Talos). During SEM imaging, the sample composition was determined by energy dispersive spectroscopy (EDS). For TEM imaging, a small amount of

Fe_3O_4/RGO sample was dispersed in isopropanol *via* ultrasonication; a drop of the homogeneous suspension was deposited on a holey carbon TEM grid and examined by TEM at 120 and 200 kV. X-ray photoelectron spectroscopy (XPS) measurements were performed on a Kratos Ultra XPS system (Kratos, Kanagawa, Japan) with a monochromatic Al Kα source ($h\nu$ = 1486.6 eV). A charge neutralizer was used to reduce the effect of charging. The analysis of the XPS spectra was performed using Casa XPS software; the least square fitting of the spectra was performed using mixed Gaussian–Lorentzian peak components in the quantification process. Thermogravimetric analysis (TGA) was performed on a Q500 TGA analyzer (TA Instruments) under a stream of air flow (100 sccm) with a temperature ramp of 5 °C min^{-1} from room temperature to 900 °C.

3.2.5 Electrochemical Measurements

The half-cell assembly was carried out in an argon-filled glovebox with concentrations of moisture and oxygen below 50 ppm. The as-prepared wrinkled or unwrinkled Fe_3O_4/GO nanocomposite on the Cu foil current collector was used as anodes for cells. Microporous polypropylene membrane was used as the separator, and Li foil was used as the counter electrode. The electrolyte used was 1 M $LiPF_6$ dissolved in an ethylene carbonate (EC)/dimethyl carbonate (DMC)/diethyl carbonate (DEC) mixture (1 : 1 : 1, in wt%). Galvanostatic cycling experiments of the cells were performed on a Maccor 4300 battery test system in the voltage range of 0.001–3.00 V *versus* Li^+/Li at room temperature.

3.3 Results and Discussion

3.3.1 Motivation of Align/Wrinkle Fe_3O_4/RGO Nanosheets

In most prior studies including those discussed above, graphene layers are deposited perpendicular to the direction of ion and electron transport, which may significantly increase the ion and electron transport distance. In contract, the alignment of graphene layers in the direction

of ion and electron transport, as demonstrated in our study, is expected to dramatically enhance electrode performance. Given the magnetic properties of Fe_3O_4, this chapter explore the possibility of aligning Fe_3O_4/graphene sheets parallel to the direction of ion and electron transport. As mentioned above, tortuosity or diffusion length of Li ions plays a key role in the performance of anodes. Exposure to magnetic field induces alignment and folding of Fe_3O_4 decorated RGO sheets along magnetic field lines and induces the formation of a porous 3D structure; this reduces the transport distance of electrons and Li ions within the electrode and improves the effective surface area of active materials, as shown in the Figure 3.2. In addition, the W-Fe_3O_4/RGO nanocomposites show promise in resolving the capacity-fading problem associated with Fe_3O_4-based electrodes.

The synthetic procedure of W-Fe_3O_4/RGO anode is schematically shown in Figure 3.1. The first step involves *in situ* deposition of Fe_3O_4 nanoparticles on the dispersed GO sheets. The well-dispersed Fe_3O_4/GO sheets in ethanol obtained by adding citric acid was stabilized by the COOH groups of the citric acid coordinated to the Fe_3O_4 nanoparticles. In the second step, dip coating of Fe_3O_4/GO solution on a copper foil current collector and immediate exposure of the coated solution to a strong magnetic field resulted in wrinkled Fe_3O_4/GO sheets on the copper foil. The Fe_3O_4/GO sheets can be dragged up or folded along magnetic field lines as illustrated in Figure 3.2. The magnetic field lines near the top surface of the magnet are vertically oriented, thus the magnetic nature of Fe_3O_4 forces the RGO sheets to form wrinkled structure along the direction of magnetic lines. Following annealing treatment at 550 °C to reduce the GO sheets according to a recipe described in the experimental section, W-Fe_3O_4/RGO anodes are formed.

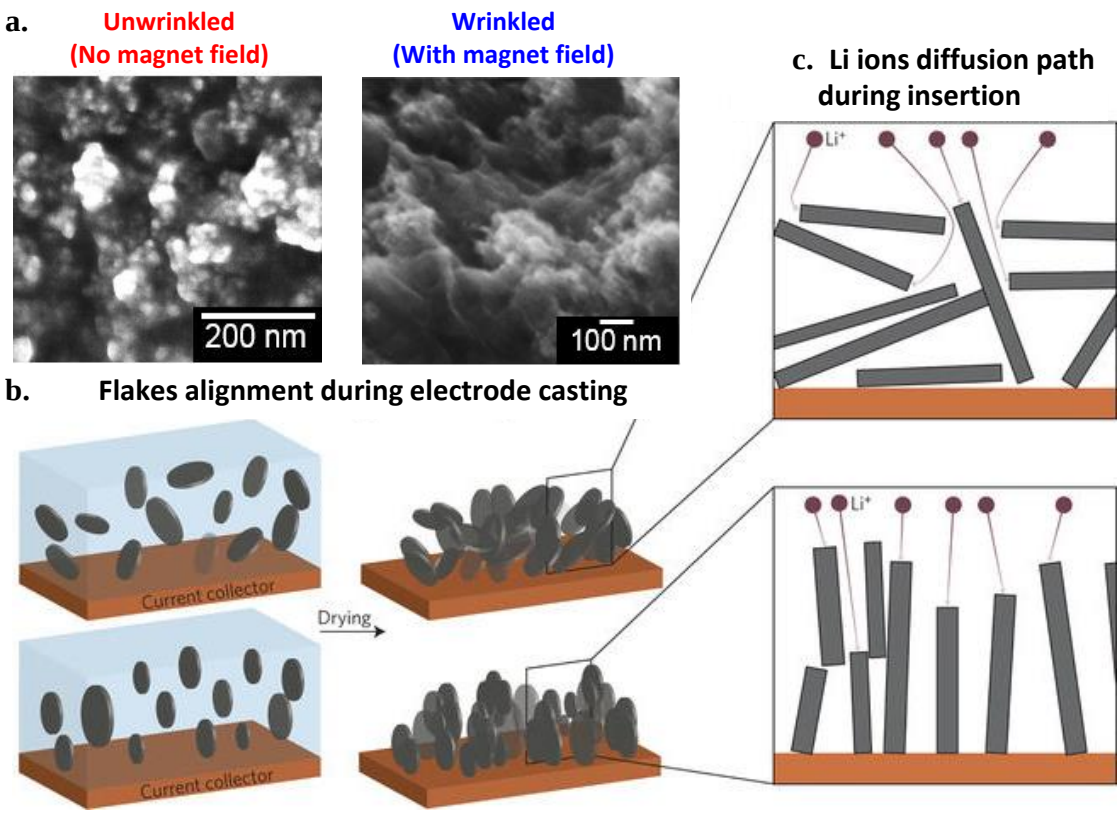

Figure 3.2 Reduced diffusion distance for Li ions in align/wrinkle Fe_3O_4/RGO nanosheets[134]. Reformed by permission from J. Billaud, F. Bouville, T. Magrini, C. Villevieille, A. R. Studart, *Nature Energy*, 2016, 1, 16097. Copyright 2016 Springer Nature.

3.3.2 Chemical Characterization of Fe_3O_4/RGO

The structure and phase purity of the synthesized Fe_3O_4/RGO nanocomposites were characterized by XRD. Figure 3.3a shows XRD patterns of Fe_3O_4/RGO nanocomposites, RGO, and pure Fe_3O_4 nanoparticles. The profile for RGO shows a broad peak around 2θ degrees of 20–30° that is attributed to defects in RGO[135]. Also, the absence of the typical (002) peak of GO ~12.3° in the XRD profile of RGO[136] is a strong evidence of the successful reduction of GO to RGO *via* thermal treatment. The XRD profile of the as-prepared Fe_3O_4 nanoparticles is well indexed to magnetite or face-centered cubic Fe_3O_4 (JCPDS no. 63-3107), suggesting the absence of other phases. In particular, all of the identified XRD peaks of Fe_3O_4/RGO obtained after annealing treatment can be indexed to

fcc Fe_3O_4 and RGO components. The crystallite size, calculated from the (311) reflection using the Debye–Scherrer formula, is 10.5 nm. The Raman spectra in Figure 3.3b show the characteristic peaks of carbonaceous materials at 1601 cm^{-1} (G-band), 1350 cm^{-1} (D-band), and the modulated bump ~2700 cm^{-1} (2D region). The G-band is associated with graphite in-plane stretching vibrations of sp^2 carbon atoms with E_{2g} symmetry while the D-band is assigned to the A_{1g} mode of sp^3 carbon atoms in disordered graphite. The integrated intensity ratio of the D- and G-bands (I_D/I_G = 1.25) of RGO is higher than that of GO (I_D/I_G = 0.81). This demonstrates restoration of sp^2 carbon, as well as an increase in the number of smaller graphene domains, edge planes, and disorder upon reduction of GO[137, 138]. The inset in Figure 3.3b shows a weak Raman signal of Fe_3O_4 at ~688 cm^{-1}. The Raman results are consistent with the XRD profiles and provide evidence of the successful synthesis of Fe_3O_4/RGO.

The synthesized Fe_3O_4/RGO nanocomposites were further characterized by XPS, TGA and EDS, to determine their chemical composition. The EDS spectrum of Fe_3O_4/RGO (Figure 3.4) has three main peaks that indicate the presence of C, Fe, and O, and two small peaks that are attributed to N and Cu. The XPS survey scan in Figure 3.3c corroborates the presence of C 1s, O 1s, and Fe 2p peaks with Fe/C atomic ratio of 0.46, estimated from C 1s and Fe 2p peaks for Fe_3O_4/RGO; the detailed elemental compositions are also presented in Table 3.1. From the TGA profile in Figure 3.3d, the weight percentage of Fe_3O_4 in Fe_3O_4/RGO nanocomposite is determined to be 85.9 wt%. The initial weight loss below 200 °C is most likely associated with the removal of moisture and volatile organics. However, the actual weight percentage of Fe_3O_4 in Fe_3O_4/RGO (83.03 wt%) was used in the calculation of specific capacity. The slightly weight gain (2.87 %) is due to the oxidation process of Fe_3O_4 to Fe_2O_3 during TGA analysis in air[139, 140].

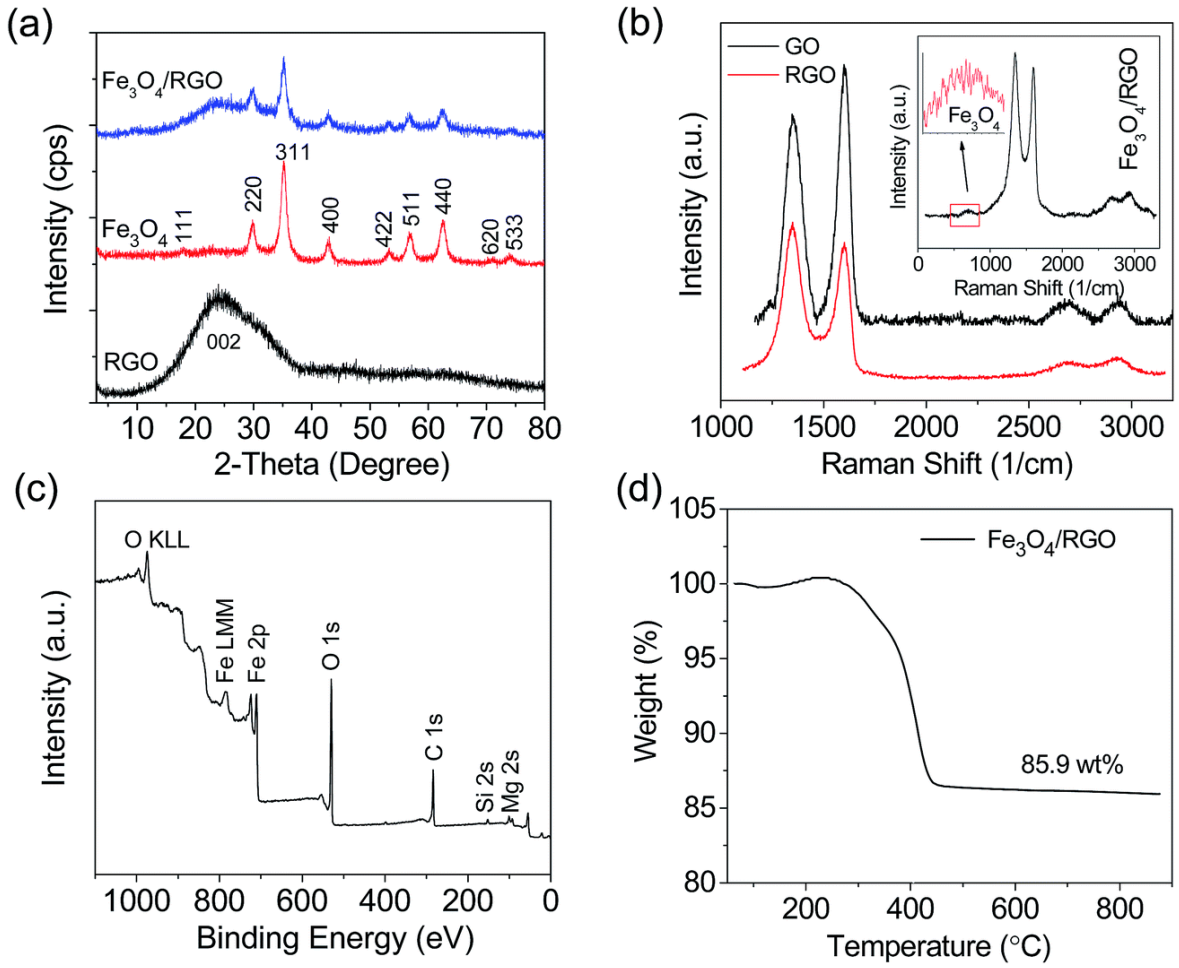

Figure 3.3 (a) XRD patterns of RGO, pure Fe_3O_4 nanoparticles, and as-synthesized Fe_3O_4/RGO nanocomposite. (b) Raman spectra of GO, RGO and Fe_3O_4/RGO nanocomposite. (c) XPS survey scan of Fe_3O_4–RGO nanocomposite. (d) TGA curve of Fe_3O_4/RGO nanocomposite under airflow at a temperature ramp of 5 °C min^{-1}.

Table 3.1 Atomic concentrations of aligned and unaligned Fe_3O_4/RGO nanocomposite from XPS survey scans.

Element	Atomic Concentration (%)	Atomic Concentration (%)
O 1s	24.861	30.124
C 1s	44.069	32.671
N 1s	0.861	0.688
Co 2p	1.455	0
Fe 2p	7.948	14.996
Si 2p	9.040	9.350
Mg 2s	11.766	12.170
	Aligned sample	Unaligned sample

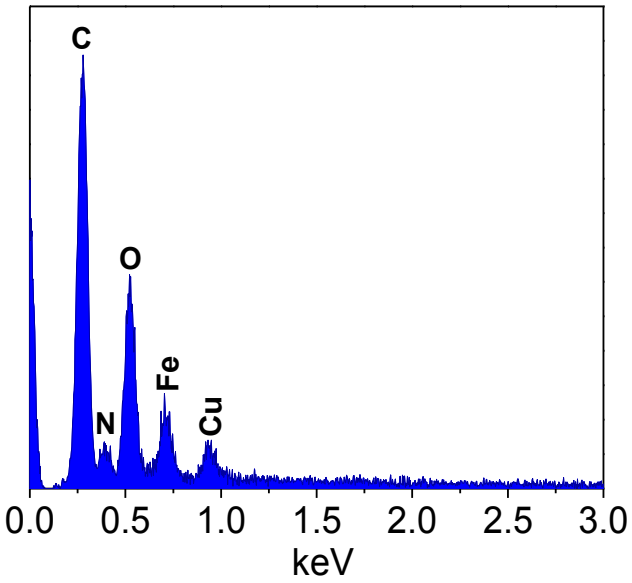

Figure 3.4 Energy dispersive X-ray pattern of Fe_3O_4/RGO nanocomposite.

The high-resolution XPS spectra for Fe 2p and C 1s for wrinkled and unwrinkled samples are shown in Figure 3.5. The Fe $2p_{3/2}$ and $2p_{1/2}$ are positioned at binding energies of 711.3 and 724.9 eV, respectively; the broadening of these peaks is evidence of the presence of a Fe^{2+} and Fe^{3+} or Fe_3O_4, which is a mixed state of FeO and Fe_2O_3 and confirms that Fe in the synthesized nanocomposite exist in Fe_3O_4 state. We note that the satellite peak of Fe $2p_{3/2}$ is used to identify the different oxidation states; Fe^{2+} and Fe^{3+} have satellite peaks at 715 and 719 eV, respectively[138]. There is a small peak at ~719 eV for both the wrinkled and unwrinkled samples (Figure 3.5a), indicating the existence of small amount of Fe_2O_3 in our samples. The deconvolution of the C 1s peak (Figure 3.5b) reveals the presence of three types of carbon species: C–C (284.5 eV), C–O (286.8 eV), and C=O (287.7 eV). The C–C peak is attributed to the carbonaceous species from RGO while the oxygen-containing species, C–O and C=O (carbonyl), are features that are associated with GO and Fe–RGO linkages. The respective carbon atomic compositions of C–C, C–O, and C=O for W-Fe_3O_4/RGO are 41.1, 39.3, and 19.7 at% while the compositions for the U-Fe_3O_4/RGO are 40.8, 37.7, and 21.4 at%, respectively.

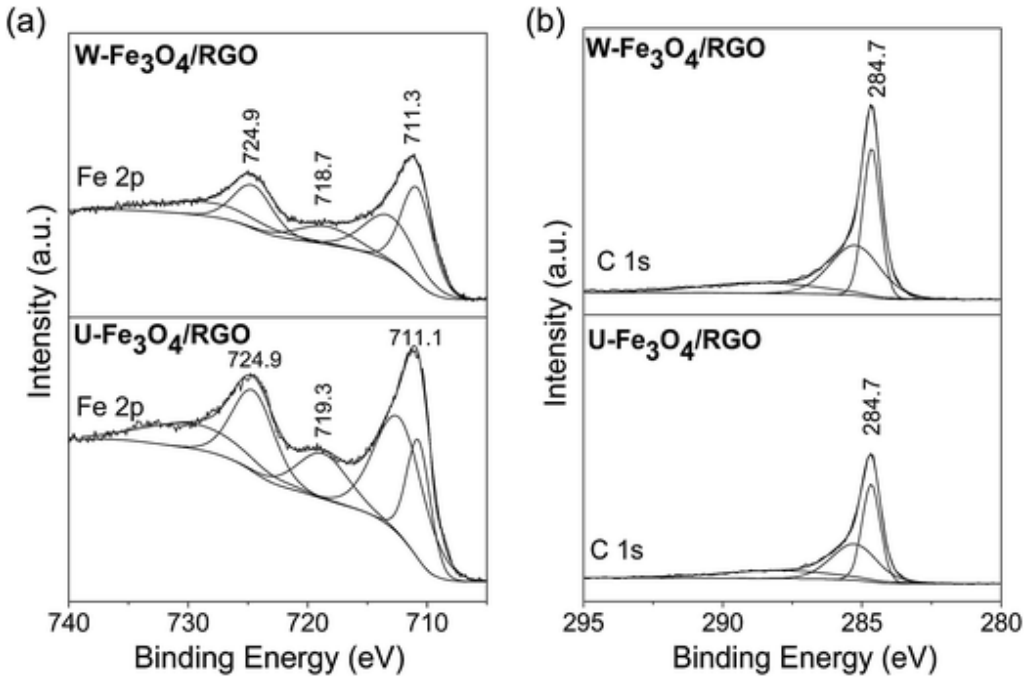

Figure 3.5 High-resolution XPS spectra of Fe 2p (a) and C 1s (b) for wrinkled and unwrinkled Fe_3O_4/RGO anodes and their related curve fitted components.

3.3.3 Morphology of Fe_3O_4/RGO Anode

The morphology of the as-synthesized Fe_3O_4/RGO anodes was examined using a FESEM. Panels a and b in Figure 3.6 are low and high magnification FESEM images of U-Fe_3O_4/RGO electrode, respectively. This sample was synthesized without exposure to a magnetic field. The images show Fe_3O_4 nanoparticles, with average diameter of 10 nm, forming a relatively smooth and unaligned morphology on RGO structures. In some areas, the RGO sheets are observed partially covering the Fe_3O_4 nanoparticles (see red lines in Figure 3.6, panel a). The representative high magnification image in panel b shows that the Fe_3O_4 nanoparticles experience severe aggregation during the fabrication process without the magnetic field treatment. The aggregation of electrode nanoparticles has been shown to induce capacity fading and loss of electrical contact between electrodes and current collectors[141, 142]. A common approach for preventing aggregation in nanocomposites is the addition of a dispersant or coating with graphene or carbon layers[143, 144], which

usually require careful control and extensive optimization of the fabrication steps. In contrast to the unwrinkled samples prepared without magnetic treatment, Figure 3.6 shows low (panels c and e) and high magnification (panels d and f) images of W-Fe_3O_4/RGO electrodes exposed to a strong magnetic field during the synthesis process. Because of the drag-up force along magnetic field lines, W-Fe_3O_4/RGO show curled and wrinkled morphologies with Fe_3O_4 nanoparticles decorated on ridged RGO sheets. The zoomed-in images in Figure 3.6 (panels d and f) show that the Fe_3O_4 nanoparticles are well dispersed on the wrinkled RGO sheets. The W-Fe_3O_4/RGO nanocomposites are characterized by a nanoporous structure with randomly organized pores and a non-agglomerated morphology, and are well adapted to facilitate the lithium insertion and extraction kinetics due to the reduced diffusion distance[47], as well as accommodate the strain caused by the severe volume expansion of Fe_3O_4 nanoparticles. Therefore, our highly porous and wrinkled Fe_3O_4/RGO anode is well suited for supplying rapid transport pathways for both lithium ions and electrons, thus enhancing the rate capability.

Figure 3.6 also reveal that the centrifugation conditions of the Fe_3O_4–citric acid/GO ethanol solution affected the formation of the wrinkled Fe_3O_4/RGO structures on the copper substrate. The two W-Fe_3O_4/RGO samples shown in panels c and d (Sample-1) and e and f (Sample-2) are compared. Both samples were synthesized using the same procedure except that Sample-1 was subjected to centrifugation at 6000 rpm (~2414*g* force) for 15 min while Sample-2 was not. The vertical folding/orientation of RGO sheets in panels e and f (Sample-2) is higher than the sheets in Sample-1. The difference in wrinkles can be observed more clearly in the zoomed-in images in panels d and f. We hypothesize that the well-dispersed Fe_3O_4–citric acid/GO sheets may be experiencing re-aggregation under high-speed centrifugation, which could impede the folding/orientation of Fe_3O_4–citric acid/GO sheets. Our findings show that the use of Fe_3O_4–citric acid/GO ethanol solution that has

not been subjected to centrifugation yields highly wrinkled Fe_3O_4/RGO anodes, as further verified by high magnification FESEM (see images presented in Figure 3.7).

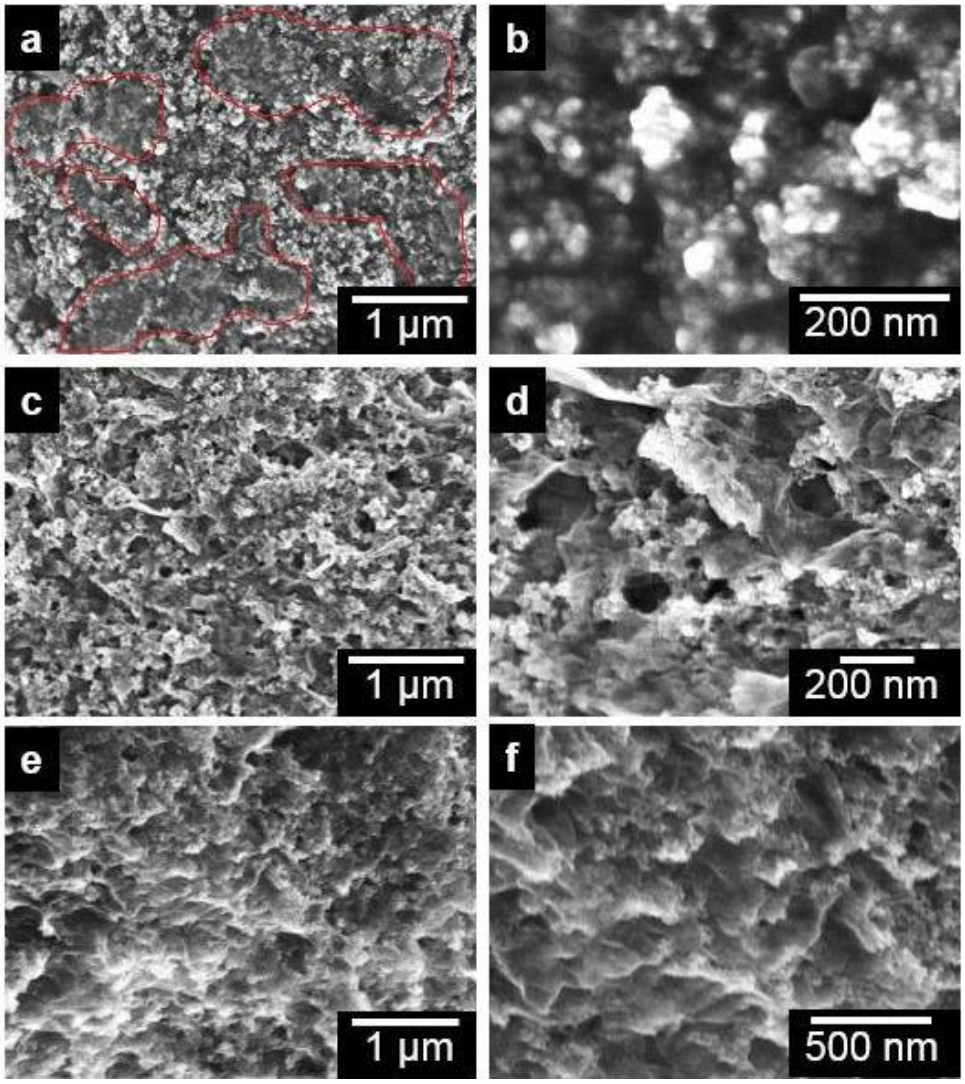

Figure 3.6 SEM images of wrinkled and unwrinkled Fe_3O_4/RGO anodes. (a and b) Low- and high- magnification images of U-Fe_3O_4/RGO anodes synthesized without magnetic field treatment. (c and d) Low- and high- magnification images of W-Fe_3O_4/RGO anodes subjected to magnetic field and centrifugation treatments during synthesis (centrifugation at 6000 rpm for 15 min). (e and f) Low- and high- magnification images of W-Fe_3O_4/RGO anodes exposed to magnetic field without centrifugation.

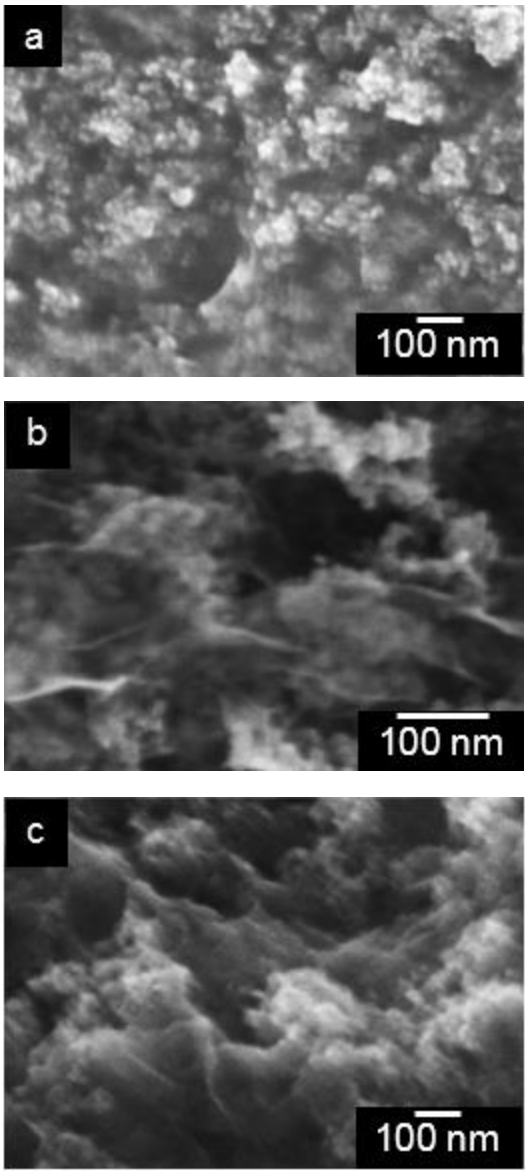

Figure 3.7 SEM images of Fe_3O_4/RGO anode materials: (a) synthesized without exposure to magnetic field; (b) synthesized with exposure to magnetic field and centrifugation treatment; and (c) synthesized with exposure to magnetic field without centrifugation treatment.

Further evaluation of the morphology of the as-synthesized Fe_3O_4–RGO was carried out by TEM (Figure 3.8). The Fe_3O_4nanoparticles are non-agglomerated and highly uniform in size (panel a). Evidence of Fe_3O_4 nanoparticles in contact with RGO sheets is shown in panel b. From the TEM images, the average size of Fe_3O_4 nanoparticles is about 10 nm, which is consistent with the calculated

value from XRD using the Debye–Scherrer equation. The zoomed-in high-resolution TEM image of panel c (panel d) shows well-resolved lattice fringes with an interlayer distance of 0.25, corresponding to the (311) plane of Fe_3O_4.

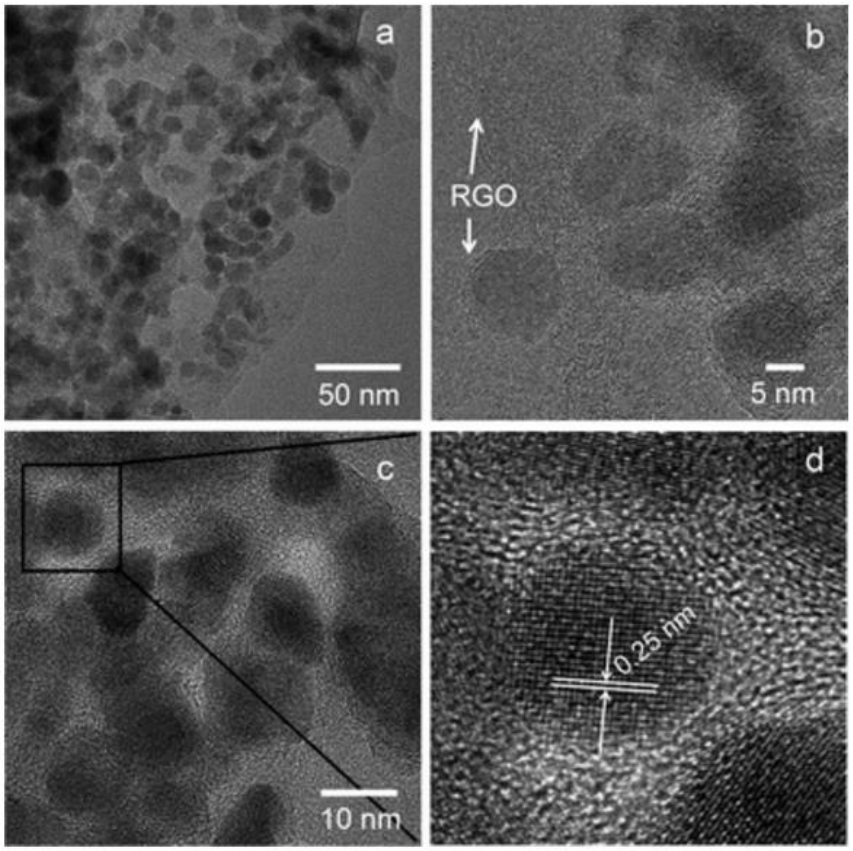

Figure 3.8 TEM images of Fe_3O_4/RGO. (a) Low-magnification image showing Fe_3O_4 nanoparticles. (b) Fe_3O_4 nanoparticles in contact with RGO, (c and d) High-resolution images of Fe_3O_4 nanoparticles.

3.3.4 Electrochemical Characterization of Fe_3O_4/RGO Anodes

The W-Fe_3O_4/RGO electrode material was first evaluated by cyclic voltammograms (CV) between 0.001 and 3.0 V at a scan rate of 0.1 mV s^{-1}. Figure 3.9a shows the reduction and oxidation peaks in the first four complete scans. In general, the CV results for the W-Fe_3O_4/RGO electrode are consistent with previously reported results for Fe_3O_4-based electrodes[35, 126]. In the first cathodic scan,

two well-defined peaks are observed at 0.60 and 0.02 V, which are attributed to the reduction of Fe_3O_4 to Fe^0 (by the reaction: $Fe_3O_4 + 8Li^+ + 8e^- \leftrightarrow 3Fe^0 + 4Li_2O$) and lithium ions insertion in the RGO sheets, respectively. Meanwhile, the anodic peaks between 1.6 and 2.0 V correspond to the reversible oxidation of Fe^0 to Fe^{2+} and Fe^{3+}. In subsequent CV scans, the anodic curves were very similar to the first anodic curve whereas the subsequent cathodic curves are quite distinguishable from the first scan. The cathodic peaks shifted from 0.60 to 0.78 V, revealing structural modifications during the first scan. Moreover, the decreased intensity of the cathodic peaks compared to the 0.60 V peak in the first cathodic scan and the appearance of new peaks at 1.5 V, indicate the occurrence of some irreversible reactions with formation of an SEI layer. It should be emphasized that the cathodic and anodic profiles seem to overlap after the second scan, which indicates the high stability of the W-Fe_3O_4/RGO anodes during cycling.

Figure 3.9b shows representative discharge/charge voltage profiles of W-Fe_3O_4/RGO electrode at a current density of 0.2C (157 mA g^{-1}) between 0.001 and 3.00 V. The calculated theoretical specific capacity of the synthesized Fe_3O_4/RGO nanocomposite is 830 mA h g^{-1} using the respective weight ratios of Fe_3O_4 (83 wt%) and RGO (17 wt%) obtained from TGA analysis, and the assumption that the theoretical specific capacity of Fe_3O_4 is 924 mA h g^{-1} and that of RGO is 372 mA h g^{-1}. The first discharge voltage profile presents a steep voltage drop from 2.22 to 0.75 V and a voltage plateau at 0.75 V; these features are related to the cathodic peak at 0.6 V in the first CV scan (Figure 3.9a). The second discharge curve shows a different voltage plateau at 0.88 V, which agrees well with the positive shift and decreased intensity of cathodic peaks in the second CV scan, suggesting that irreversible reactions and polarization of the electrode material occurred in the first cycle[145].

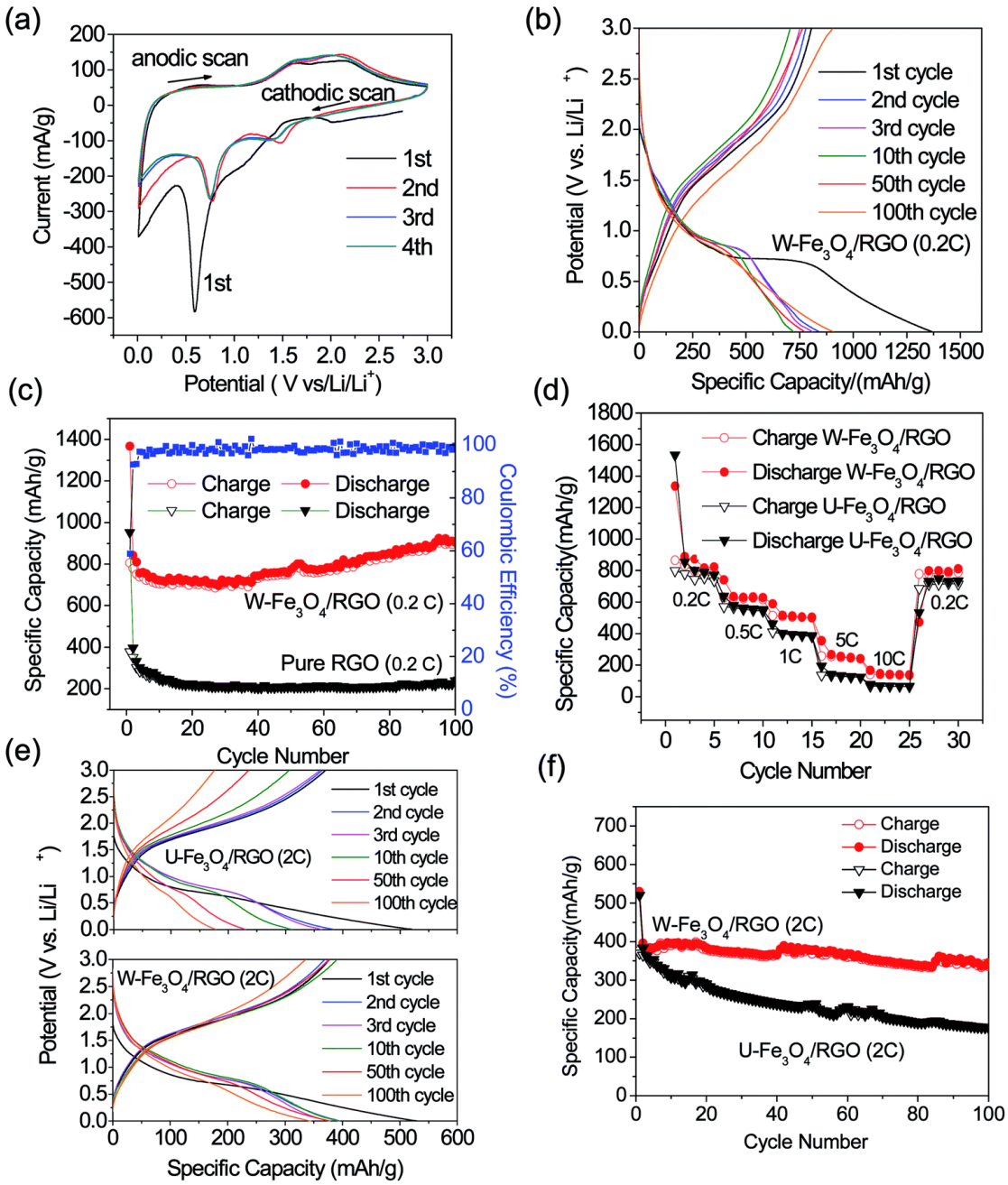

Figure 3.9 (a) Cyclic voltammograms for the first 4 cycles of W-Fe_3O_4/RGO anode at a scan rate of 0.1 mV s−1 in the potential window of 3.0–0.001 V (vs. Li/Li^+). (b) Selected discharge–charge profiles (1st, 2nd, 3rd, 50th, and 100th cycle) of W-Fe_3O_4/RGO anode at a cycling rate of 0.2C. (c) Cycling performances of RGO and W-Fe_3O_4/RGO anodes at 0.2C. The coulombic efficiency of W-Fe_3O_4/RGO anode is also displayed (blue curve). (d) Cycling performance of W-Fe_3O_4/RGO and U-Fe_3O_4/RGO anodes at different cycling rates of 0.2C, 0.5C, 1C, 5C and 10C with a cutoff voltage window of 3.0–0.001 V. (e) Selected discharge–charge profiles (1st, 2nd, 3rd, 50th, and 100th cycle) of W-Fe_3O_4/RGO and U-Fe_3O_4/RGO anodes at a cycling rate of 2C. (f) Cycling performance of W-Fe_3O_4/RGO and U-Fe_3O_4/RGO anodes at a cycling rate of 2C with a cutoff voltage window of 3.0–0.001 V.

The cycling performance of pure RGO and W-Fe_3O_4/RGO electrodes evaluated between 0.001 and 3.0 V at a current rate of 0.2C (157 mA g^{-1}) up to 100 cycles is presented in Figure 3.9c. The W-Fe_3O_4/RGO anode shows a discharge and charge specific capacity of about 710 mA h g^{-1} in the first 40 cycles, and thereafter gradually increases to 903 mA h g^{-1} at the 100th cycle. For comparison, the specific capacity of RGO electrode, cycled at the same current density, is only a quarter of the capacity observed for the W-Fe_3O_4/RGO electrode. The continuous increase in capacity with cycle number (in our case, between the 40th and 100th cycle) has been observed in studies involving CuO–graphene[146], CoO[147], and Fe_3O_4–graphene[148-150]. This phenomenon is attributed to a number of factors including increased contact of anode components with increasing cycle number due to structural rearrangement, reversible growth of a polymeric gel-like film following kinetically activated electrolyte degradation, and the nanosized iron particles in the composite may enhance surface electrochemical reactivity and anode conductivity[147, 148]. Furthermore, a coulombic efficiency of about 99% is achieved after only three cycles, demonstrating the efficient insertion and extraction of lithium ions during cycling.

Figure 3.9d shows a comparison of the rate capability of wrinkled and unwrinkled Fe_3O_4/RGO electrodes at various current densities from 157 mA g^{-1} (0.2C) to 7.85 A g^{-1} (10C). Even at high current densities of 3.93 A g^{-1} (5C) and 7.85 A g^{-1} (10C), the W-Fe_3O_4/RGO electrode can still deliver stable reversible specific capacities of 250 and 150 mA h g^{-1}, respectively. It is noteworthy that when the current density returns to the initial 0.2C after 25 cycles, a reversible specific capacity of 790 mA h g^{-1} can still be recovered. In general, the difference in specific capacities between the wrinkled and unwrinkled electrodes is magnified at higher C-rates (1C, 5C and 10C) than at lower C-rates (0.2C and 0.5C). The comparison of the specific capacities of W-Fe_3O_4/RGO and Fe_3O_4/C microrods (synthesized by a similar magnetic field-induced method) at

different current densities is presented in Table 3.2. The results indicate that W-Fe_3O_4/RGO composite anode is well equipped to deal with the high Li-ion flux at high current densities across the material interface and exhibits rate capability that is comparable to Fe_3O_4/C anode reported in ref. 130.

Table 3.2 Comparison of cycling performance of Fe_3O_4/nanocarbon anodes synthesized by a magnetic field induced method.

Ref. 130		**Our work**	
Fe_3O_4/C microrods		W-Fe_3O_4/RGO	
92 wt% Fe_3O_4, 8% carbon		83 wt% Fe_3O_4, 17% RGO	
Current densities (mA g^{-1})	Specific capacities (mA h g^{-1})	Current densities (mA g^{-1})	Specific capacities (mA h g^{-1})
200	650	157	800
400	500	393	620
600	430	785	510
800	390	3925	250
1000	380	7850	150

To highlight the cycling stability of the W-Fe_3O_4/RGO electrode at high current density, we investigated the cycling performance of W-Fe_3O_4/RGO electrode at a current density of 1.57 A g^{-1} (2C) as shown in Figure 3.9e and f. For comparison, the U-Fe_3O_4/RGO electrode was also investigated under similar conditions. The first reversible specific capacity for the U-Fe_3O_4/RGO electrode is as high as 383 mA h g^{-1}. However, due to the structural degradation or volume expansion of bare Fe_3O_4nanoparticles upon lithiation, the reversible capacity quickly fades to 176 mA h g^{-1} at the 100th cycle, exhibiting only 46% capacity retention. The rapid capacity fading observed in the U-Fe_3O_4/RGO electrode is attributed to the severe aggregation of the Fe_3O_4 nanoparticles as confirmed by the FESEM images in Figure 3.6, panels a and b. In contrast, the reversible capacity of W-Fe_3O_4/RGO electrode remains relatively constant at 345 mA h g^{-1} for the 100th cycle with a capacity

loss of only 10%. We attribute the improved performance of the W-Fe_3O_4/RGO to the unique properties that are induced by the vertical folding or alignment of the RGO sheets. First, the wrinkled RGO sheets provide buffer space for the expansion of Fe_3O_4 nanoparticles. Second, the wrinkled structure of Fe_3O_4/RGO increases the surface area of active materials. Third, folding or alignment along magnetic lines facilitates the mobility of electrons and ions. The outstanding rate capability and high durability exhibited by W-Fe_3O_4/RGO electrode during cycling makes it particularly well adapted for high-performance LIBs.

3.4 Conclusion

We have developed a novel approach to fabricate W-Fe_3O_4/RGO electrodes *via* application of a strong magnetic field. The W-Fe_3O_4/RGO electrodes are characterized by a nanoporous and non-agglomerated morphology with Fe_3O_4 nanoparticles well dispersed on the curled RGO sheets. When evaluated as an anode for LIBs, W-Fe_3O_4/RGO shows outstanding LIB performance with a high specific capacity of 903 mA h g^{-1} at a current density of 157 mA g^{-1}, and a high rate capability that delivers a capacity of 353 mA h g^{-1} at a current density of 1.57 A g^{-1}. In addition, W-Fe_3O_4/RGO is characterized by a high capacity retention upon extensive cycling with the specific capacity staying fairly constant after 60 cycles at a current density of 1.57 A g^{-1}. The superior capacity retention and overall enhancement in LIB performance of W-Fe_3O_4/RGO electrode at high current density is attributed to the magnetic field-induced alignment and folding of the RGO sheets, which provides the elastic buffer region for Fe_3O_4nanoparticles and a shorter pathway for Li ion diffusion. The magnetic field-induced fabrication strategy presented here can be extended to other nanocarbon composites involving magnetic nanoparticles.

Chapter 4 - PMAA-Induced Self-Assembly of Mesoporous Fe_3O_4@Graphene and Its Application in Lithium-Ion Batteries

4.1 Introduction

Smart polymers or stimuli-responsive polymers are suitable to construct a morphology controllable network due to their conformation and structural change in response to applied external stimulus, such as pH, temperature, light, and electrical or magnetic field[151-153]. Slight external triggers can induce significant changes in structure and properties of smart polymers, including the change of degree of cross-linking, expansion or shrinkage of polymer volume or the detachment of polymer functional groups. Poly(methacrylic acid) (PMAA), a common pH-responsive polymer, has already attracted intense attention due to its interesting dependence of charge density on solution pH[154-156]. PMAA contains a large number of ionizable carboxyl groups, which makes it a type of water-soluble weak polyelectrolytes with a pKa value of 4.9 [157]. The dissociation degree of carboxyl groups is largely influenced by the environmental pH; PMAA chains can undergo reversibly transitions between tightly coiled conformations at low pH and highly extended conformations at high pH[158].

Previous zeta-potential analyses[159, 160] indicate that graphene oxide (GO) sheets were negatively charged in aqueous media over a wide pH range of 1 to11. The charge density of GO varies with pH, enabling the GO sheets to also be considered a pH-responsive material. Recently, some pH-sensitive GO-based materials have been prepared by grafting of PMAA polymer via covalent or noncovalent interactions[161, 162]. These studies mainly focused on the pH responsive properties of the polymer chains in biomedical engineering application[152, 153], while applications in energy storage, especially lithium ion batteries, is yet to be reported.

Fe_3O_4 has a high theoretical capacity of 926 mAh g^{-1}, and is widely used for lithium ion batteries anodes[126, 163, 164]. Fe_3O_4 nanoparticles of controlled size distribution can be deposited onto GO sheets via in situ aqueous reaction, resulting in coordination bonds between Fe atoms and COOH groups on GO surface[163]. However, the concentration of Fe_3O_4@GO aqueous suspension is usually very low (< 0.6 mg/ml) due to the reduced number of the repelling functional groups after the depositing Fe_3O_4 onto GO surface. The use of PMAA as a stabilizer can result in a higher concentration of Fe_3O_4@GO suspension in water. More importantly, it is possible to control the dispersion state of PMAA stabilized Fe_3O_4@GO sheets in water by changing the pH due to the high pH response of PMAA; this simple strategy can be employed in the design of high-performance electrode materials for LIB application. Previous studies of developing desired Fe_3O_4@graphene electrode mainly focused on seeking novel synthesis reactions of Fe_3O_4@graphene nanocomposite[148, 165-167], the size control of Fe_3O_4 nanoparticles[168-170], and the structural design mostly by sacrificial template methods[123, 126, 171]. However, self-assembly of Fe_3O_4@graphene has received little attention, especially using of pH-responsive polymer as the assembly agent. As mentioned above, in spite of the immense potential of pH-responsive polymers in LIB application, there are currently limited publications on the subject. As a common pH-responsive polymer, PMAA is worthwhile to investigate in terms of designing a desired Fe_3O_4@GO structure for high-performance anodes materials. Furthermore, the underlying mechanism of self-assembly behavior of Fe_3O_4@GO sheets using PMAA is poorly understood and will benefit from further examination.

Herein, we report a highly porous Fe_3O_4@RGO anodes material prepared by adjusting pH values of aqueous media. Fe_3O_4@GO sheets form a network, and PMAA acts as a stabilizer, a cross-linking agent and a driving force for structural change. The Fe_3O_4@GO-PMAA sheets

demonstrate phase transfer behavior at different pH since PMAA is a weak polyanion, exhibiting a negative and neutral charge at high and low pH, respectively[154-156].

The focus of this work is to evaluate the effectiveness of PMAA in dispersing Fe_3O_4@GO in water and understand the pH-responsive behavior of the stabilized suspensions. Various techniques (rheology measurement, UV-Vis, microscopy and electrophoretic light scattering) were used to characterize the dispersion of Fe_3O_4@GO. The results indicate that PMAA is influential in controlling the dispersion state of Fe_3O_4@GO in water and resulting porosity of Fe_3O_4@RGO after drying and annealing. Furthermore, lower weight ratio of PMAA to Fe_3O_4@GO shows different degree of stabilization of Fe_3O_4@GO in comparison to the same sample in the same solution pH, but with a higher weight ratio. Based on the results, a stabilizing mechanism is proposed to explain the pH-responsive self-assembly of Fe_3O_4@GO sheets in water. This work expands the scope of Chapter 3 and provides fresh insights into the dispersion and stabilization of Fe_3O_4@GO in water using weak polyelectrolytes.

4.2 Experimental Section

4.2.1 Synthesis of PMAA

150 ml of ethanol, 67 g of PMAA agent and 0.7g of 2, 2′-azobis (2-methylpropionamidine) dihydrochloride (AIBA) were added to a 500 ml flask equipped with thermocouple for monitoring the temperature and a mechanical stirring device. The reaction mixture was purged with argon at ambient temperature for 30 min under stirring. The temperature was then raised to 65 °C, and the mixture was kept at 65 °C for 6 h. The reaction mixture was then cooled to 25 °C, and the sample was dried and stored for further analysis. The solid content (or percentage of PMAA) was 35 wt% in the solvent.

4.2.2 Preparation of Fe_3O_4@GO-PMAA Aqueous Solution

The method for decoration of Fe_3O_4 nanoparticles on GO sheets is presented in Chapter 3 (Section 3.3.3). 259.6 mg $FeCl_2 \cdot 4H_2O$ and 708.4 mg $FeCl_3 \cdot 4H_2O$ were added to GO dispersion (50 mL of 1 mg mL^{-1}) at 80 °C under N_2 atmosphere.

For lower weight ratio of PMAA to Fe_3O_4@GO composite, 12 mg of PMAA was mixed with 20 mg Fe_3O_4@GO in 10 ml water, and sonicated at room temperature for 1 h to form coordinate bonds between Fe_3O_4 and PMAA while for the sample with a higher ratio, 48 mg of PMAA was added in the dispersion. Ammonia and HCl solutions were used to adjust pH between 1 and 9 for the Fe_3O_4@GO-PMAA dispersed in water dispersion.

In comparison, Fe_3O_4@GO-citric acid dispersion was also prepared following the steps in Section 3.3.3 of Chapter 3.

4.2.3 Self-Assembly of Porous Fe_3O_4@RGO Anodes

The as-prepared Fe_3O_4@GO-PMAA dispersion (~2 mL) was drop cast on the copper current collector (9 μm thick) and dried at 40 °C in the vacuum oven. Thereafter, the dried Fe_3O_4/GO was annealed at 600 °C for 3 h in argon atmosphere to reduce GO to RGO. The synthesis steps for porous Fe_3O_4@RGO anodes are illustrated in Figure 4.1. PMAA is able to stabilize Fe_3O_4@GO in water and facilitate the formation of a concentrated Fe_3O_4@GO dispersion (~2 mg/ml). Thereafter, by changing pH of the solution from basic to acidic, crumpled Fe_3O_4@GO sheets were formed. Fe_3O_4@RGO anode stabilized via critic acid treatment was also prepared for the purpose of comparison.

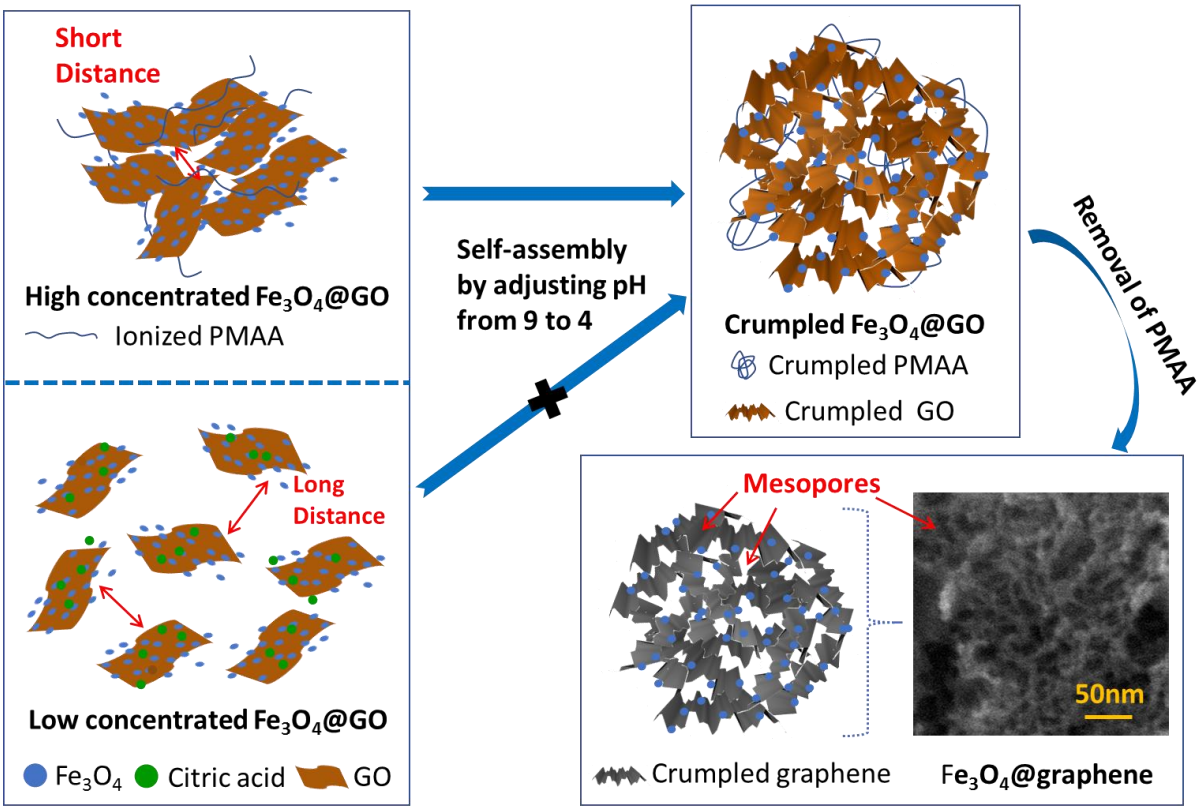

Figure 4.1 Illustration of self-assembly of crumpled Fe_3O_4/RGO anodes via adjusting pH of dispersion.

4.2.4 Materials Characterization

The XRD patterns were collected on a Rigaku Miniflex II X-ray diffractometer with Cu Kα radiation (λ = 1.5418 Å) at 40 kV and 40 mA. The morphological characterization of the samples was conducted using a field emission scanning electron microscope (FESEM, Hitachi S5200) and a transmission electron microscope (TEM, FEI Talos). For TEM imaging, a small amount of Fe_3O_4/RGO sample was dispersed in isopropanol *via* ultrasonication; a drop of the homogeneous suspension was deposited on a holey carbon TEM grid and examined by TEM at 120 and 200 kV. Thermogravimetric analysis (TGA) was performed on a Q500 TGA analyzer (TA Instruments) with a temperature ramp of 5 °C min^{-1} from room temperature to 900 °C under a stream of air flow and 600°C under nitrogen flow for Fe_3O_4@RGO and PMAA, respectively. UV-Vis measurements were

made with a UV-2600 spectrometer (Shimadzu) using plastic cuvettes. Suspensions were diluted to a suitable value for UV-vis measurements. Viscosity of the suspensions as function of shear rate was measured using a Brookfield rheometer equipped with a 40 mm parallel plate geometry. The annealing treatment was performed in a CVD system by heating at 600 °C for 3 h in argon flow. Brunauer-Emmet-Teller (BET) specific surface area was determined from N_2 adsorption using a Quantachrome (Autosorb-1) instrument at liquid nitrogen temperature. Raman spectra were measured using a Horiba 550 Raman spectrometer with a laser wavelength of 532 nm. The zeta potentials were measured on a Brookhaven zeta potential analyzer. The pH dependence of zeta potential for Fe_3O_4@GO-PMAA aqueous suspension at 23 °C was measured at different pH.

4.2.5 Electrochemical Measurements

The half-cell assembly was carried out in an argon-filled glovebox with concentrations of moisture and oxygen below 5 ppm. The as-prepared Fe_3O_4@RGO nanocomposite on the Cu foil current collector was used as anodes for cells. The separator was a microporous polypropylene membrane, and the counter electrode was Li foil. The electrolyte was prepared by dissolving 1 M $LiPF_6$ in an ethylene carbonate (EC)/dimethyl carbonate (DMC)/diethyl carbonate (DEC) mixture (1 : 1 : 1, in wt %). Galvanostatic cycling experiments of the cells were performed on a Maccor 4300 battery test system in the voltage range of 0.001–3.00 V *versus* Li^+/Li at room temperature.

4.3 Results and Discussions

4.3.1 pH-response of Fe_3O_4@GO-PMAA in Aqueous Dispersion

Figure 4.2 shows the molecular structures of citric acid and PMAA. The COOH groups on both molecules can form coordination bonds with Fe_3O_4, and thus can be used as stabilizers for Fe_3O_4@GO dispersion. However, citric acid is a much smaller molecule than the long chain PMAA polymer, which makes citric acid a type of non pH-sensitive electrolytes. The FTIR spectra

(Figure A.5) suggests PMAA has a high number of COOH groups in a single chain. Figure 4.3 exhibits a scheme of the conformational changes the PMAA chain undergoes as a function of pH. PMAA is a type of weak polyacid with isoelectric point at pH ~2[172]. Therefore PMAA can form a transparent and homogeneous water solution (1.2 mg/ml and 4.8 mg/ml) at any pH higher than 1.0 due to ionization of COOH associated with negative zeta potential values[172]. At high pH (> 5), the PMAA chains are in ionized state and behave as randomly coiled or extended configuration. The high negative charge density along the polymer backbone causes the polymer chain to repel itself, and thus further stabilize the attached Fe_3O_4@GO sheets. At low pH (< 4), PMAA exhibits significant intramolecular hydrogen bonding, resulting in a more crumpled or globular-like conformation. A previous study[155] confirmed that sudden conformational change of PMAA occurs from a collapsed conformation to a random coil in the range of pH 4 – 6.

PMAA can generally stabilize Fe_3O_4@GO sheets in water media at pH between 5 and 9, as shown in Table 4.1 and Figure 4.4. Two PMAA aqueous solutions with 1.2 mg/ml and 4.8 mg/ml were used for this study. The black Fe_3O_4@GO suspensions were stable even after storing for a long time (>1 month). However, at pH < 4 or > 9, the Fe_3O_4@GO sheets are highly aggregated. Note at specific pH (pH 5, 7 and 9), there are differences in the degree of dispersion for Fe_3O_4@GO stabilized by 1.2 mg/ml PMAA and 4.8 mg/ml PMAA. The stability of Fe_3O_4@GO dispersion with 4.8 mg/ml PMAA decreases from “highly dispersed” to “moderately dispersed” and then to “slightly dispersed” with the increase of pH from 5 to 7 and then to 9, respectively. In particular, at pH 9, some particles can be observed at the bottom of the container after one-month storage while for Fe_3O_4@GO dispersion with 1.2 mg/ml PMAA, the best stability was achieved at pH 7, and two similar moderate stabilities occurred at pH 5 and 9. To

rationalize the differences in the stability of the dispersions at pH 5, 7 and 9, zeta potential, UV-vis spectroscopic and viscosity measurements were carried out.

Zeta potential represents the equilibrium electric potential at an imaginary surface (shear plane) of particles in the liquid. Typically, the more positive or negative zeta potentials correspond to higher stability of dispersed particles. Table 4.2 shows zeta-potential for Fe_3O_4@GO-PMAA aqueous suspensions with 1.2 mg/ml and 4.8 mg/ml PMAA at pH 5, 7, and 9. The zeta potential exhibits an increasing trend as the pH increases from 5 to 9, regardless of the concentration of PMAA; this is mainly attributed to the increasing amount of COOH groups ionized from PMAA as pH increases. Besides, at the same pH, 4.8 mg/ml PMAA stabilized Fe_3O_4@GO suspensions show higher zeta potentials than those with 1.2 mg/ml PMAA in general. Interestingly, even the most negative zeta potential occurs at pH 9 for the Fe_3O_4@GO-PMAA suspensions with different concentrations, the highest stabilities were observed at much lower pH (pH 5 for 4.8 mg/ml PMAA-stabilized Fe_3O_4@GO and pH 7 for 1.2 mg/ml PMAA-stabilized Fe_3O_4@GO). This "paradox" has been explained by UV-Vis spectroscopic and particle size data presented in following section.

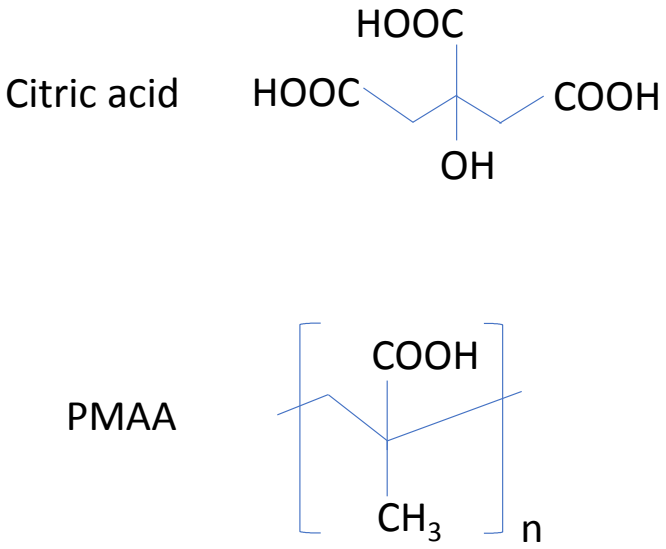

Figure 4.2 Structural difference between citric acid and PMAA.

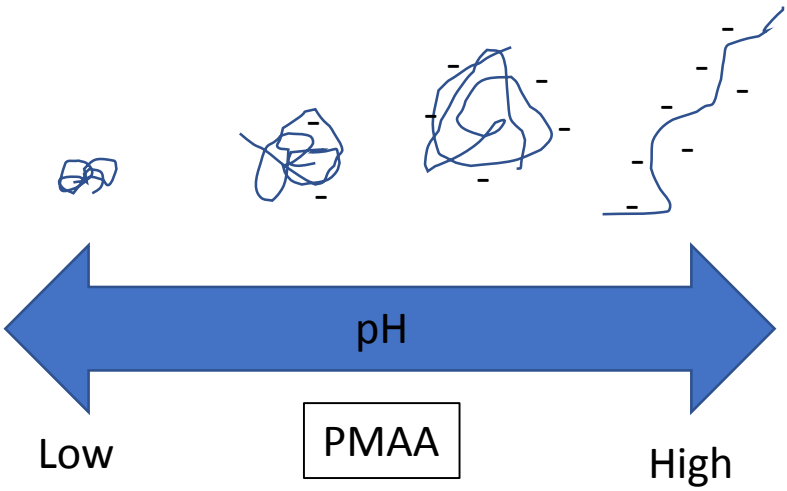

Figure 4.3 Schematic illustration of the effect of pH on the chain conformations of PMAA.

Table 4.1 Dispersion state of PMAA aqueous solution and Fe_3O_4@GO-PMAA aqueous suspensions with 1.2 mg/ml and 4.8 mg/ml PMAA at varying pH levels.

pH	PMAA dispersion state	Fe_3O_4@GO-PMAA dispersion state (1.2 mg/ml)	Fe_3O_4@GO-PMAA dispersion state (4.8 mg/ml)
1	Crumpled	Precipitated suspension	Precipitated suspension
2			
3		Slightly dispersed suspension	Slightly dispersed suspension
5	Mostly coiled	Moderately dispersed suspension	Highly dispersed suspension
7		Highly dispersed suspension	Moderately dispersed suspension
9	Mostly extended	Moderately dispersed suspension	Slightly dispersed suspension
11		Precipitated suspension	Precipitated suspension

Table 4.2 Zeta potential of Fe_3O_4@GO-PMAA aqueous suspensions with 1.2 mg/ml and 4.8 mg/ml PMAA at varying pH levels (*concentration was diluted to one-half of original concentration for testing).

pH	Zeta potential (mV)	Zeta potential (mV)
5	-21.4	-36.5
7	-26.9	-48.5
9	-51.1	-52.9
T=23 °C	1.2 mg/ml *	4.8 mg/ml *

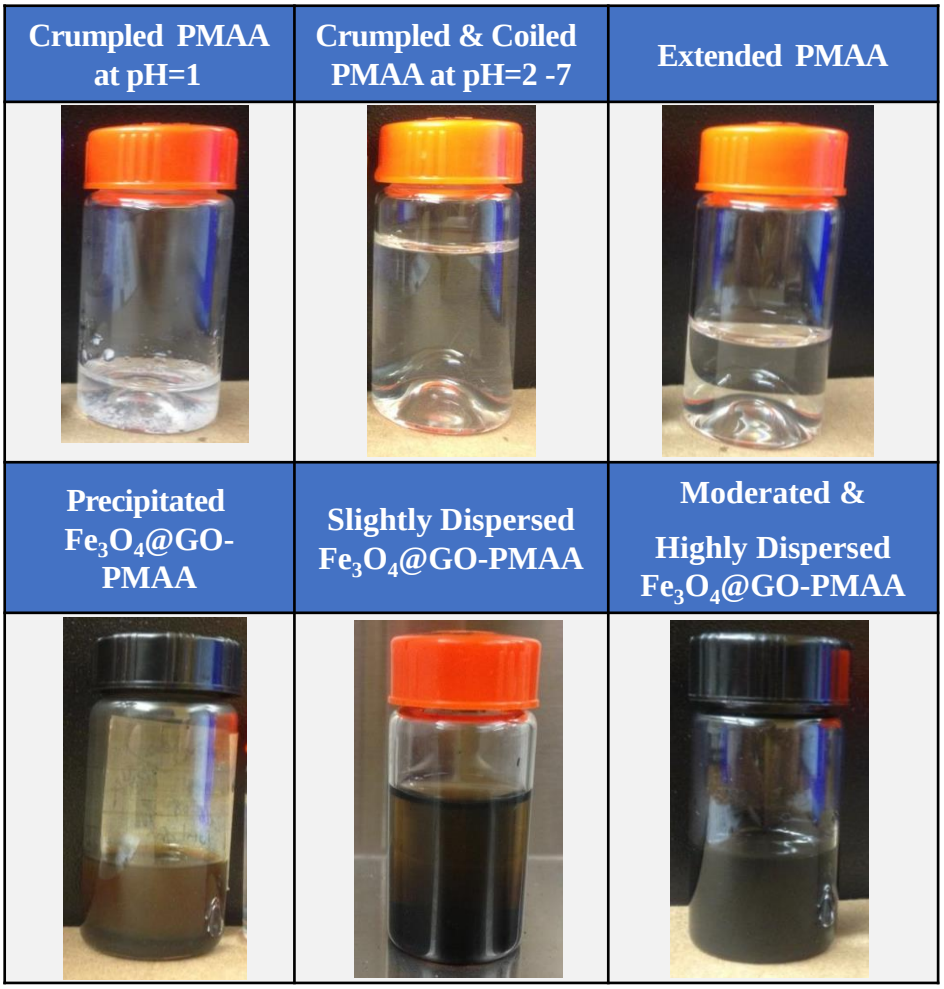

Figure 4.4 Pictures of PMAA aqueous solution and Fe_3O_4@GO-PMAA aqueous suspensions with 1.2 mg/ml and 4.8 mg/ml PMAA at different pH levels.

UV-Vis spectroscopic analysis was used to determine the optimum pH for stabilizing Fe_3O_4@GO (Figure 4.5). The stability of 2 mg/ml Fe_3O_4@GO with 1.2 mg/ml PMAA and 4.8 mg/ml PMAA dispersions were systematically studied at different pH. It has been reported that suspensions containing more dispersed particles have higher UV absorbance compared to suspensions containing agglomerated ones[158, 173]. 1.2 mg/ml PMAA stabilized Fe_3O_4@GO at pH 7 shows the highest UV-Vis adsorption, while for 4.8 mg/ml PMAA stabilized Fe_3O_4@GO, highest UV-Vis absorption occurs at a pH of 5. Since pure PMAA (1.2 and 4.8 mg/ml) shows almost zero UV-Vis absorbance, the above mentioned difference is mainly attributed to the presence of more COO^- on 4.8 mg/ml PMAA

stabilized Fe_3O_4@GO sheets than that of on 1.2 mg/ml PMAA stabilized Fe_3O_4@GO, which has been identified by the zeta potential data in Table 4.2. So, for 4.8 mg/ml PMAA-stabilized Fe_3O_4@GO, at relatively lower pH of 5, there is enough negative charge density (-36.5 mV of zeta potential) along GO sheet for repulsing other neighboring GO sheets, even though PMAA are still in coiled conformation at that acidic pH. In comparison, for 1.2 mg/ml PMAA-stabilized Fe_3O_4@GO, enough charge density can be achieved at pH 7 (-26.9 mV of zeta potential) instead of at pH 5 (-21.4 mV of zeta potential).

As pH increases from 5 to 9, more COO^- groups emerge, which results in fully extended configuration of PMAA chains formed eventually. Note that it is highly possible that one extended PMAA chain attaches to more than one surrounding GO sheet via bonding with Fe_3O_4; as a result, the GO sheets can be pulled much closer resulting in restacking. Andre Ditsch, et.al.[174] have also reported a similar phenomenon for the poly acrylic acid (PAA) stabilized Fe_3O_4, demonstrating that one PAA chain can link to multiple Fe_3O_4 particles and then form "bridging" between those Fe_3O_4 particles. For 4.8 mg/ml PMAA stabilized Fe_3O_4@GO, UV-vis absorption decrease as pH increase from 5 to 9. This result well supports the "bridging" induced restacking hypothesis at high pH range. Interestingly, for 1.2 mg/ml PMAA stabilized Fe_3O_4@GO, UV-Vis absorption trend shows somewhat difference. Enough charge density of PMAA cannot be achieved at pH 5 but at pH 7 and thus the highest absorption occurs at pH 7; while at pH 9, the restacking of GO sheets also occurs but insignificantly compared to that of 4.8 mg/ml PMAA stabilized Fe_3O_4@GO at pH 9.

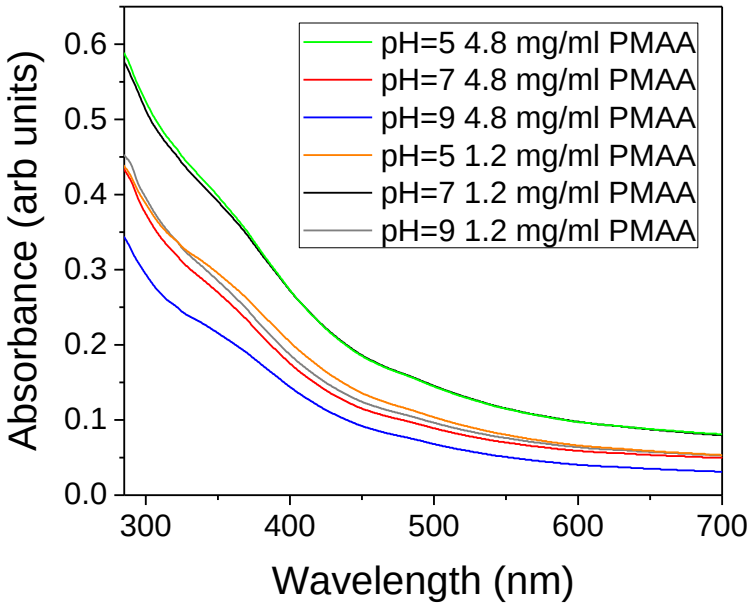

Figure 4.5 UV-Vis spectra of Fe_3O_4@GO-PMAA aqueous suspensions with 1.2 mg/ml and 4.8 mg/ml PMAA at varying pH levels.

Size of Fe_3O_4@GO-PMAA in the Figure 4.6 supports the "bridging" phenomena observed in UV-Vis data. Smallest effective particle diameter was achieved at pH 7 for the 1.2 mg/ml PMAA stabilized Fe_3O_4@GO, which suggest the optimum dispersion state in that condition, while the particle size increases at pH 5 due to the lower charge density on Fe_3O_4@GO sheets. At pH 9, even the charge density reaches a high value (-51.1 mV of zeta potential), the stability of suspension decreases because of the "bridging" between neighboring Fe_3O_4@GO sheets. In comparison, for the 4.8 mg/ml PMAA-stabilized Fe_3O_4@GO, effective particle diameters keep increasing as pH increases from 5 to 9. The most severe "bridging" occurs at pH 9, which results in a slightly dispersed suspension, as observed in Figure 4.4. Therefore, based on the UV-Vis and particle size results, we conclude that in general, Fe_3O_4@GO suspensions show better stability at pH 5 or 7 than at pH 9 and "bridging" occurring point is related to the concentration of PMAA (or the weight ratio of PMAA to Fe_3O_4@GO).

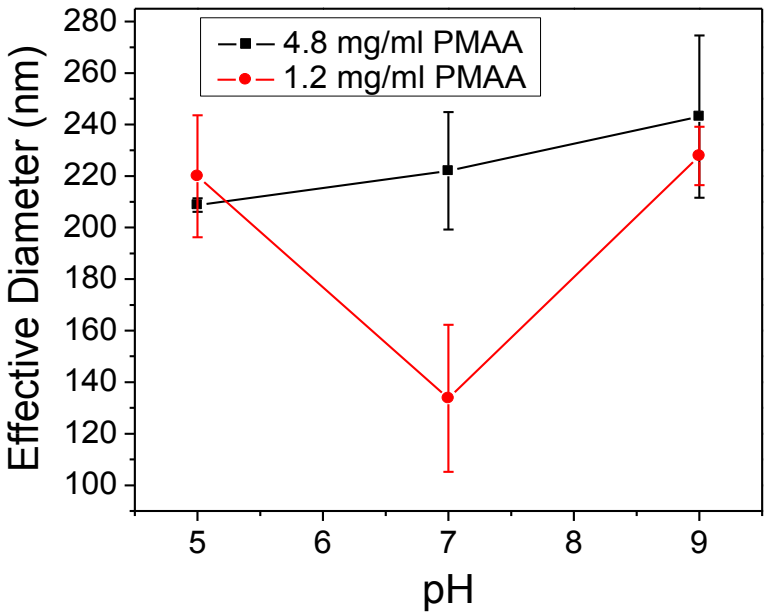

Figure 4.6 Particle effective diameter of Fe_3O_4@GO-PMAA aqueous suspensions with 1.2 mg/ml and 4.8 mg/ml PMAA at different pH levels.

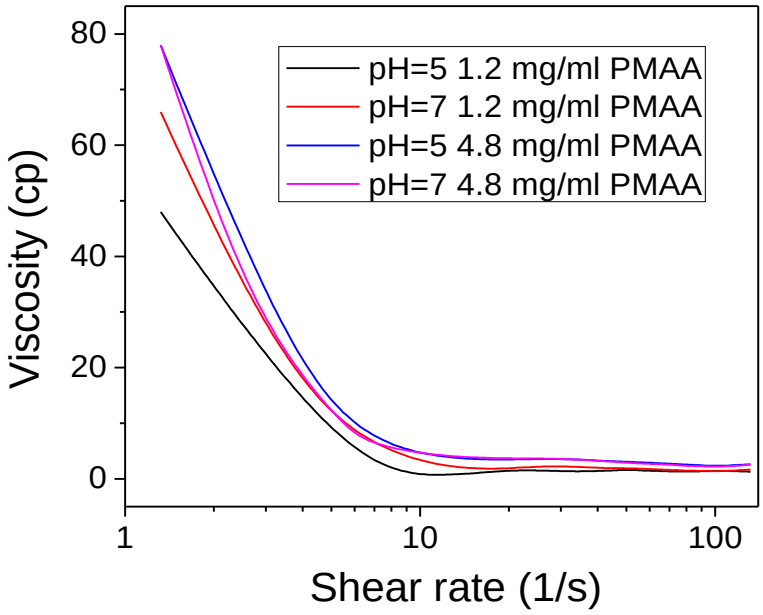

Figure 4.7 Viscosity as a function of shear rate for Fe_3O_4@GO-PMAA aqueous suspensions with 1.2 mg/ml and 4.8 mg/ml PMAA at different pH levels.

Suspensions with well-dispersed GO sheets are known to show higher viscosities compared to those that have agglomerated sheets[175]. Furthermore, it was shown that below the critical concentration of 90 mg/ml, PMAA-water solution does not show shear thinning or thickening behavior with increase of shear rate[176]. The observed shear-thinning behavior in Fe_3O_4@GO-PMMA suspensions suggest the presence of highly dispersed Fe_3O_4@GO sheets. In an effort to investigate this pH-dependent behavior, viscosity measurements were obtained for 1.2 mg/ml and 4.8 mg/ml PMAA-stabilized Fe_3O_4@GO aqueous suspensions (Figure 4.7) at pH 5 and 7. The concentration of PMAA polymer denominates the viscosity of suspension due to the sticky nature of polymer. In general, 4.8 mg/ml PMAA-stabilized Fe_3O_4@GO suspensions show higher viscosity compared to those of 1.2 mg/ml PMAA-stabilized Fe_3O_4@GO suspensions. The similar viscosities at pH 5 and 7 for 4.8 mg/ml PMAA-stabilized Fe_3O_4@GO also reveals the bigger influence of PMMA concentration on viscosity, although dispersion state at pH 5 is better than pH 7 based on the UV-Vis absorption results. After comparing all the viscosity profiles in Figure 4.5, we conclude again that 1.2 mg/ml PMAA-stabilized Fe_3O_4@GO at pH 7 and 4.8 mg/ml PMAA-stabilized Fe_3O_4@GO at pH 5 are two conditions for the highest dispersion due to their high viscosities.

4.3.2 Chemical and Structure Characterization of Fe_3O_4@RGO Anode

As shown in Figure 4.1, Fe_3O_4@RGO anode materials are produced after annealing the Fe_3O_4@GO-PMAA sheets at 600 °C for 3 h. For anode preparation, we used 1.2 mg/ml PMAA-stabilized Fe_3O_4@GO since the PMAA has about 7% amorphous carbon left after annealing treatment (TGA, Figure A.6). The porous structure of Fe_3O_4@RGO was designed by adjusting pH of suspension from 9 to 4. Fe_3O_4@GO sheets were first stabilized by PMAA at pH 9, and in this condition, PMAA chains are completely extended and behave like connecting “bridges” by

linking neighboring Fe_3O_4@GO sheets. Therefore, the distance among GO sheets decreased a lot compared to that of citric acid-stabilized GO sheets. After decreasing pH from 9 to 4, the PMAA chains shrink to highly coil structure and the attached Fe_3O_4@GO sheets are forced to crumple at the same time.

The as-synthesized Fe_3O_4@RGO anode material was analyzed by XRD first (Figure 4.8). Diffraction peaks at $2\theta = 28.9°$, 34.9°, 42.4°, 57.8° and 62.0° are assigned to the (220), (311), (400), (511) and (440) planes of face-centered cubic Fe_3O_4 (JCPDS no. 63-3107), respectively. Remarkably, RGO diffraction peak (002) could be identified at 20-30°, indicating that the crumple state and partially stacking of graphene layers after adjusting pH from 9 to 4. The Raman spectrum of the Fe_3O_4@RGO (Figure 4.9) shows a typical peak of magnetite around 680 cm^{-1} and characteristic peaks of the D- and G-bands from graphene at around 1338 and 1600 cm^{-1}. As shown in Figure 4.10, morphology of Fe_3O_4@RGO anode was studied by SEM; the image in Figure 4.10a reveals a rough surface for PMMA-induced Fe_3O_4@RGO materials. For comparison, the citric acid-stabilized Fe_3O_4@RGO was analyzed under similar conditions and a clear contrast was observed, revealing a relatively smoother surface (Figure 4.10b). Panels c and d of Figure 4.10 clearly exhibit the porosity difference between PMAA-induced and citric acid-stabilized Fe_3O_4@RGO anodes; the former shows more mesopores (~10-40 nm) than the latter. Furthermore, for PMAA-induced Fe_3O_4@RGO, there are few agglomerated Fe_3O_4 nanoparticles as mainly existing in the citric acid-stabilized Fe_3O_4@RGO material. Additional SEM images of PMAA-induced Fe_3O_4@RGO materials are presented in the Figure A.7.

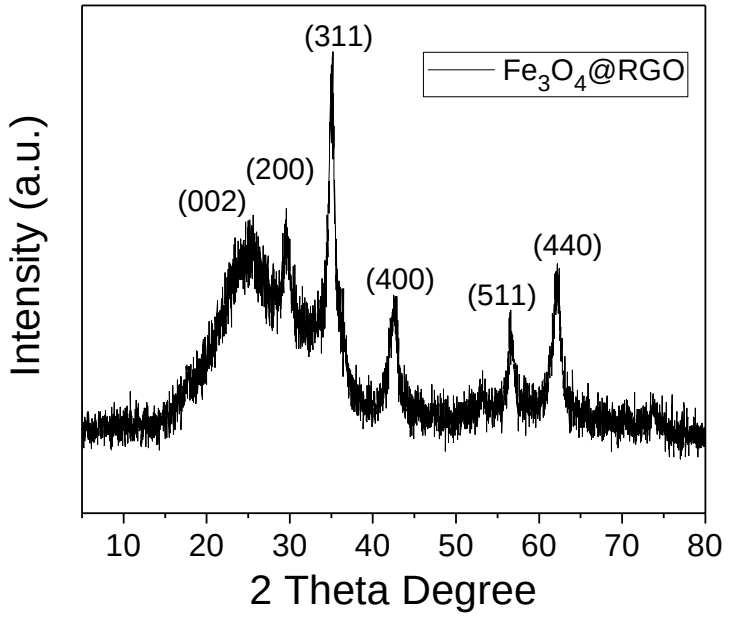

Figure 4.8 XRD pattern of Fe_3O_4@RGO.

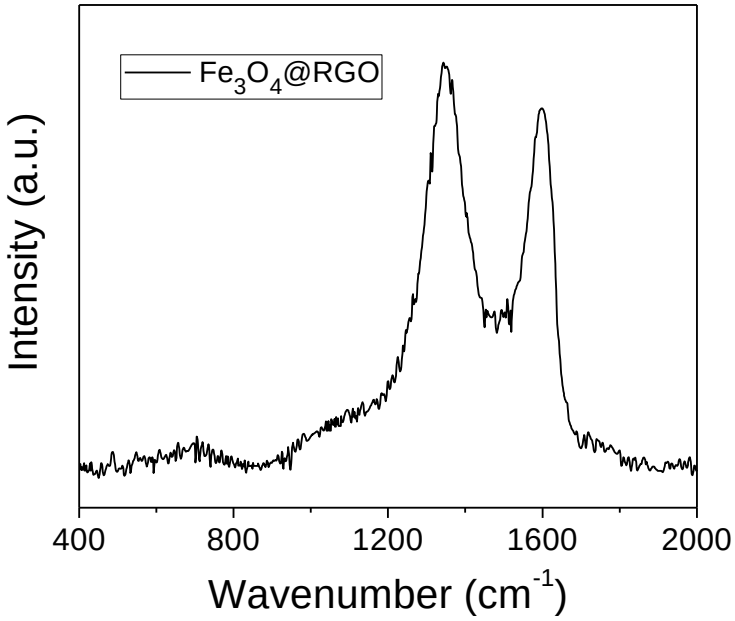

Figure 4.9 Raman spectrum of Fe_3O_4@RGO.

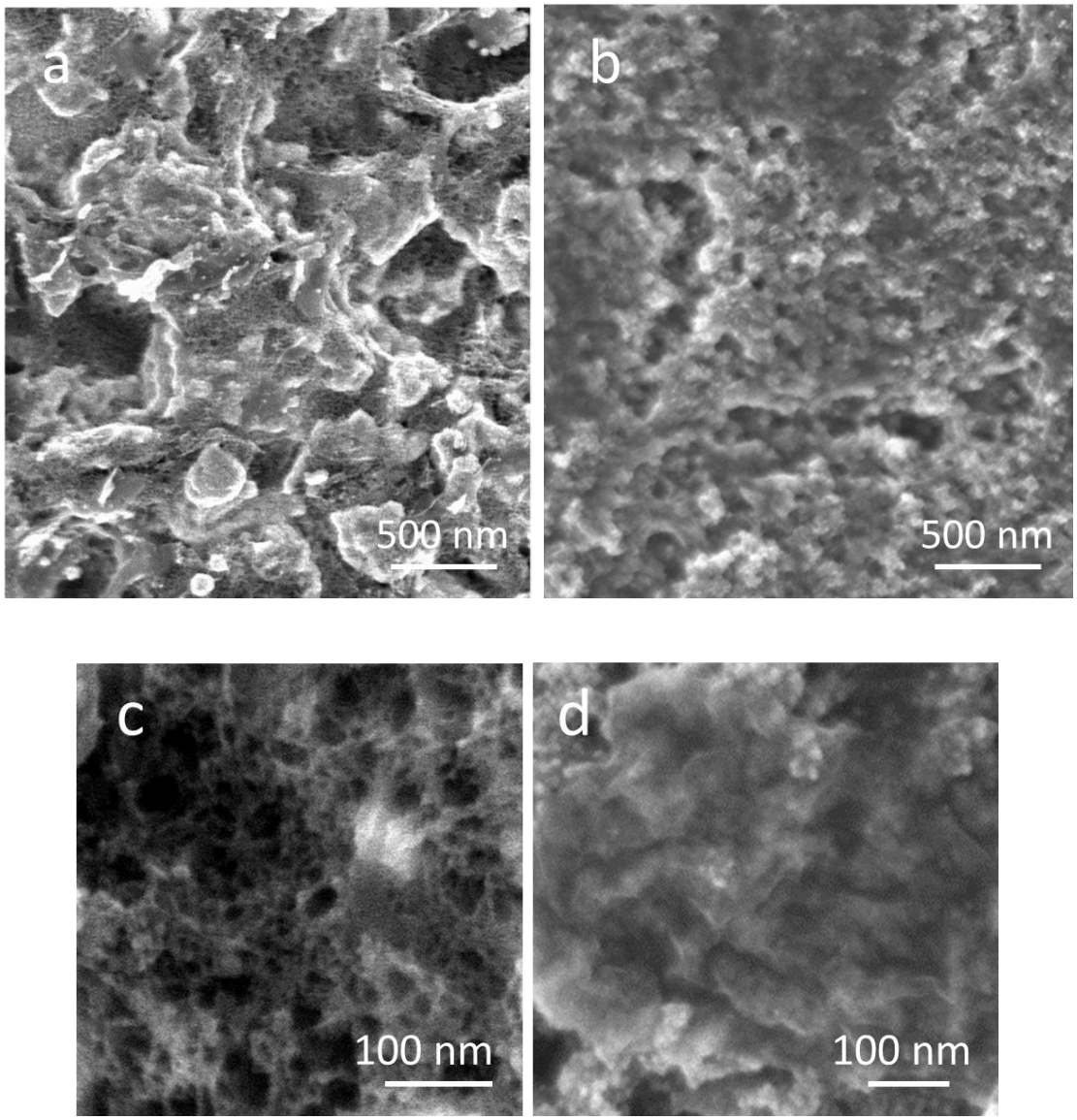

Figure 4.10 SEM images of (a) and (c) PMAA-induced porous Fe_3O_4@RGO; (b) and (d) citric acid-assisted stacked Fe_3O_4@RGO.

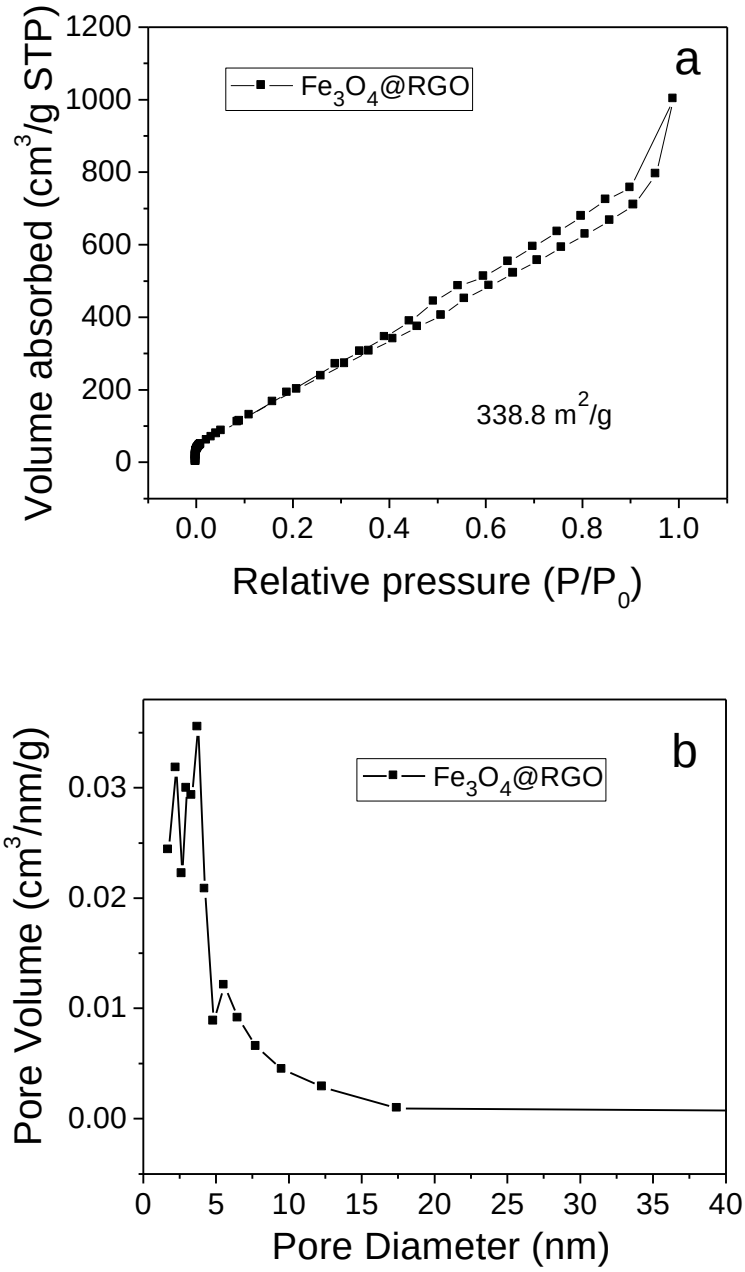

Figure 4.11 Nitrogen adsorption-desorption isotherms (a) and pore size distribution (b) of PMAA induced porous Fe_3O_4@RGO.

To further investigate the porous structure and surface area of PMAA-induced Fe_3O_4@RGO material, N_2 adsorption-desorption isotherms were obtained, as shown in Figure 4.11a. The adsorption-desorption profile is close to Type IV with an evident hysteresis loop in the 0.4-1.0 range of relative pressure, indicating the mesoporous structure of the Fe_3O_4@RGO

composites. In addition, Figure 4.11b shows the pore size distribution (BJH model) for PMAA-induced Fe_3O_4@RGO, in which most pore diameters are below ~10nm. Therefore, it can be concluded that PMAA-induced Fe_3O_4@RGO possesses a hierarchical porous structure that is composed of micropores and mesopores. Furthermore, the specific surface area of the composite is ~338.8 m^2/g, which is clearly higher than many other Fe_3O_4@RGO anodes reported in the literature (Table A.1) [159, 177-180]. To conclude, our porous structure of Fe_3O_4@RGO material does not only offer buffering rooms for huge volume expansion of Fe_3O_4 during the charge/discharge cycles, but also facilitates the transport of lithium ions and electrolyte molecules, which makes active sites accessible and eventually results in enhanced performance as an anode in LIBs.

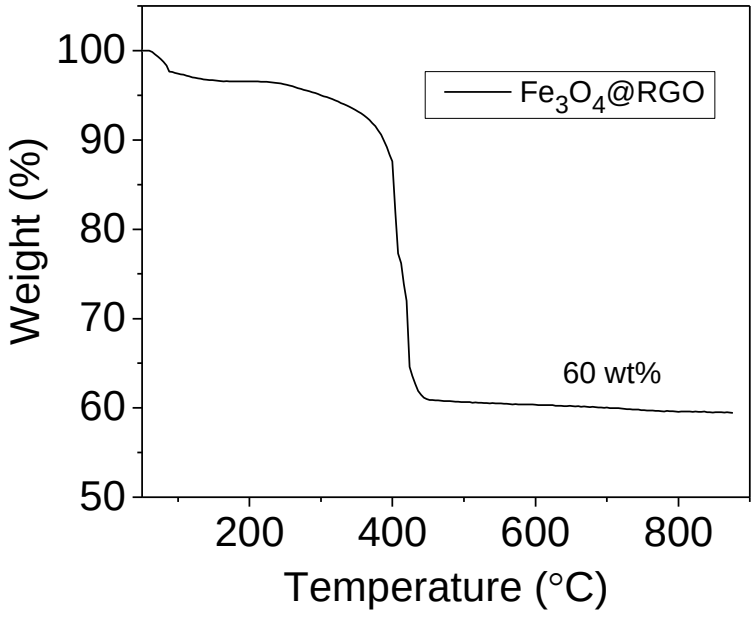

Figure 4.12 TGA curve of Fe_3O_4@RGO acquired with a temperature ramp of 5 °C min^{-1}.

4.3.3 Electrochemical Performance of Fe_3O_4@RGO Anode

From the TGA data (Figure 4.12), the composition of Fe_3O_4@RGO is 60 wt%. Based on this weight ratio, Fe_3O_4@RGO anode shows a theoretical capacity of ~703 mA h/g (924 mAh/g

× 60% + 372 mAh/g × 40%). Figure 4.13a shows the first four and the 200th discharge-charge curves of PMAA-induced Fe_3O_4@RGO half-cell at a current density of 2 A g^{-1}, with a voltage window of 0.002-3.0 V. The first discharge capacity is about 1470 mAh/g, while the second specific capacity decreases to 770 mAh/g. The irreversible capacity loss is related to formation of the solid-electrolyte interphase (SEI) film. After 200 cycles, the capacity stabilizes at 480 mAh/g. For comparison, citric acid-stabilized Fe_3O_4@RGO is also tested at the same conditions (Figure 4.13b). It is obvious that the specific capacity of citric acid-stabilized Fe_3O_4@RGO decreases faster than that of PMAA-induced Fe_3O_4@RGO. The capacity gradually fades to 200 mAh/g during 200 discharge/charge cycles.

The rate capability of PMAA-induced Fe_3O_4@RGO was studied at different current rates, from 0.5 to 10 A g^{-1}, shown in the Figure 4.13c. A specific charge capacity of 740 mAh g^{-1} is obtained at 0.5 A g^{-1}, and even at a high current density of 10 A g^{-1}, it still delivers 200 mAh g^{-1}. In contrast, the capacity of citric acid-stabilized Fe_3O_4@RGO fades dramatically to 70 mAh g^{-1} at 10 A g^{-1} (Figure 4.13d). The improved stability and rate performance of the PMAA-induced Fe_3O_4@RGO are attributed to its hierarchical porous structure, fast Li^+ diffusion, and an effective electron transport during the charge/discharge cycles.

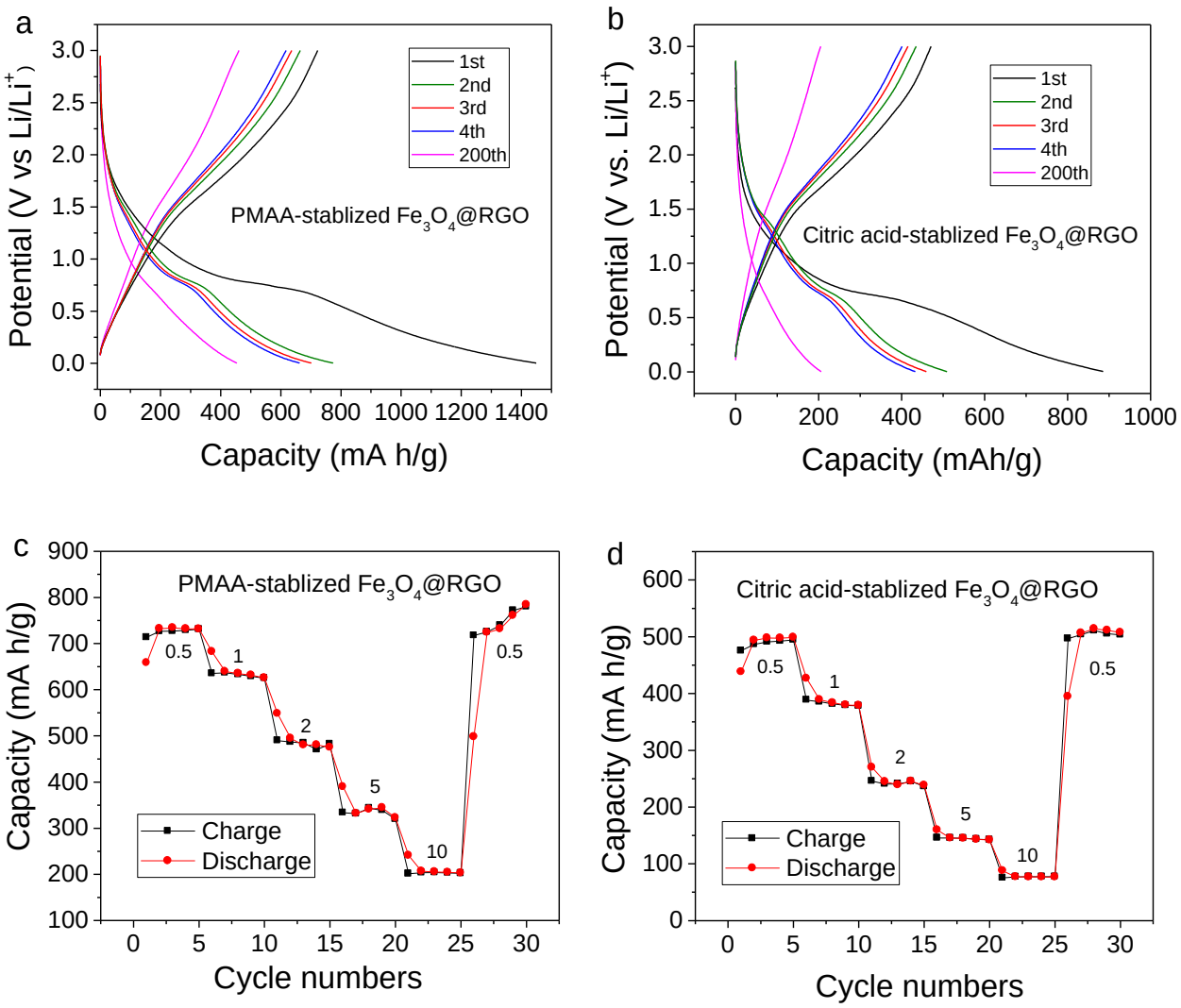

Figure 4.13 (a) Selected discharge–charge profiles (1st, 2nd, 3rd, 4th, and 200th cycles) of PMAA-stablized Fe_3O_4/RGO anode, (b) citric acid-stabilized Fe_3O_4@RGO anode at a current density of 2 A/g in the potential window of 3.0–0.002 V (*vs.* Li/Li^+), (c) Cycling performance of PMAA induced Fe_3O_4/RGO anode and (d) citric acid stabilized Fe_3O_4@RGO anode at different cycling rates of 0.5 A/g, 1 A/g, 2 A/g, 5 A/g and 10 A/g with a cutoff voltage window of 3.0–0.002 V.

4.4 Conclusions

To summarize, our results provide a guidance for the relationship between the media pH and material structure, in terms of the dispersion state of Fe_3O_4@GO and the porosity of Fe_3O_4@RGO. By adjusting media pH, configuration and charge density of PMAA chains change, which largely determine the stability of Fe_3O_4@GO in water. The concentration ratio of PMAA and Fe_3O_4@GO plays another important role on the stability of Fe_3O_4@GO due to the "bridging" phenomenon dominating at different pH values. PMAA-induced self-assembly method is facile and simple for designing an enhanced Fe_3O_4@RGO anode material. The large amounts of mesopores improved the porosity of materials and provide buffer-space for Fe_3O_4 particles, as well as accommodate the huge volume expansion during long-term discharge/charge cycles.

Chapter 5 - Concluding Remarks

In this thesis, three 3D graphene-based anodes have been designed utilizing unique approaches, involving the sacrifice of polymer templates, application of strong magnetic field, and the self-assembly induced by pH-sensitive polymer agent. The main conclusions are listed below:

- In Chapter 2, a swellable and shrinkable polymer template results in a macro and mesoporous RGO anode. The volume of the polymer template was controlled by switching solvents between "good solvent" and "poor solvent". The large amount of RGO wrinkles were formed as a consequence of changing the volume of polymer template. Our resulting RGO anode materials provided favorable transport kinetics for both Li ions and electrons due to the high surface area and more active insertion sites for Li ions. This templated method has the potential of enabling future design of graphene-based electrodes that need highly wrinkled graphene sheet structure.
- A folded and aligned Fe_3O_4/RGO anode was designed *via* application of a strong magnetic field. The alignment of RGO sheets that are parallel to the ion and electron transport direction can largely enhance capacities and rate capabilities of anodes materials. Moreover, RGO sheets provide the elastic buffer region for Fe_3O_4 nanoparticles, which accommodates the huge volume expansion during long-term charging and discharging process. The magnetic field-induced fabrication strategy presented in Chapter 3 can be extended to other nanocarbon composites involving magnetic nanoparticles.
- A pH-sensitive polymer (PMAA) was first used in Chapter 4 to design a super mesoporous Fe_3O_4@RGO anode. By tuning the media pH, we can adjust PMAA structure, dispersion state of Fe_3O_4@GO and porosity of Fe_3O_4@RGO based on our

demand. In particular, the study demonstrates, for the first time, that the "bridging" phenomenon exists between Fe_3O_4@GO and PMMA agent.

Regardless of the extensive studies on 3D graphene-based anodes, there are still some challenges to be addressed. First, a precise control of pore-size of graphene anodes is not satisfactory. Many works focus on improving porosity without considering the negative effect of the increase of surface area. For example, the surface area of SEI layer can increase as the porosity of anode materials increase, which will result in a large irreversible capacity during the first cycle. Also, in view of commercialization, because of the large void space that exist in 3D anodes, there is a trade off in volumetric capacity when compared to densely packed anodes. Second, stacking of graphene layers is still very difficult to deal with during common anode fabrication processes, although some methods, such as CVD, ball milling, and thermal-explosion, are used to obtain crystalline graphene with a single layer or few layers. The high cost of graphene is also a challenge that has to be addressed for large-scale applications to become commonplace. Third, with regard to electrochemical performance, the fabrication of graphene-based materials into free-standing anodes without using polymer binders and metallic current collectors need to be further studied in order to improve the overall gravimetric energy capacity. Moreover, from a practical consideration, flexible electronics or implantable devices need free-standing elastic structure. The improvement for tunable resilience and mechanical strength of graphene-based anodes remains a gap between academic studies to real industrial productions. To conclude, with rational and careful design, 3D graphene-based anodes will become a top candidate for next-generation LIBs.

References

[1] Tarascon, J.-M., and Armand, M. (2001) Issues and challenges facing rechargeable lithium batteries, *Nature 414*, 359-367.

[2] Mukherjee, R., Krishnan, R., Lu, T.-M., and Koratkar, N. (2012) Nanostructured electrodes for high-power lithium ion batteries, *Nano Energy 1*, 518-533.

[3] Ji, L., Lin, Z., Alcoutlabi, M., and Zhang, X. (2011) Recent developments in nanostructured anode materials for rechargeable lithium-ion batteries, *Energy & Environmental Science 4*, 2682-2699.

[4] Young, A. (2013) Market for Lithium-Ion batteries Seen Doubling Through 2016 to over $22 Billion, *International Business Times 22*.

[5] Prosini, P. P., Lisi, M., Zane, D., and Pasquali, M. (2002) Determination of the chemical diffusion coefficient of lithium in LiFePO 4, *Solid State Ionics 148*, 45-51.

[6] Shi, S., Liu, L., Ouyang, C., Wang, D.-s., Wang, Z., Chen, L., and Huang, X. (2003) Enhancement of electronic conductivity of LiFePO 4 by Cr doping and its identification by first-principles calculations, *Physical Review B 68*, 195108.

[7] Pan, A., Choi, D., Zhang, J.-G., Liang, S., Cao, G., Nie, Z., Arey, B. W., and Liu, J. (2011) High-rate cathodes based on Li 3 V 2 (PO 4) 3 nanobelts prepared via surfactant-assisted fabrication, *Journal of Power Sources 196*, 3646-3649.

[8] Winter, M., Besenhard, J. O., Spahr, M. E., and Novák, P. (1998) Insertion electrode materials for rechargeable lithium batteries, *Advanced materials 10*, 725-763.

[9] Larcher, D., Beattie, S., Morcrette, M., Edstroem, K., Jumas, J.-C., and Tarascon, J.-M. (2007) Recent findings and prospects in the field of pure metals as negative electrodes for Li-ion batteries, *Journal of Materials Chemistry 17*, 3759-3772.

[10] Winter, M., and Besenhard, J. O. (1999) Electrochemical lithiation of tin and tin-based intermetallics and composites, *Electrochimica Acta 45*, 31-50.

[11] Poizot, P., Laruelle, S., Grugeon, S., Dupont, L., and Tarascon, J. (2000) Nano-sized transition-metal oxides as negative-electrode materials for lithium-ion batteries, *Nature 407*, 496-499.

[12] Novoselov, K. S., Geim, A. K., Morozov, S. V., Jiang, D., Zhang, Y., Dubonos, S. V., Grigorieva, I. V., and Firsov, A. A. (2004) Electric field effect in atomically thin carbon films, *science 306*, 666-669.

[13] Obrovac, M., and Christensen, L. (2004) Structural changes in silicon anodes during lithium insertion/extraction, *Electrochemical and Solid-State Letters 7*, A93-A96.

[14] Zhang, W.-J. (2011) Lithium insertion/extraction mechanism in alloy anodes for lithium-ion batteries, *Journal of Power Sources 196*, 877-885.

[15] Ohzuku, T., and Brodd, R. J. (2007) An overview of positive-electrode materials for advanced lithium-ion batteries, *Journal of Power Sources 174*, 449-456.

[16] Landi, B. J., Ganter, M. J., Cress, C. D., DiLeo, R. A., and Raffaelle, R. P. (2009) Carbon nanotubes for lithium ion batteries, *Energy & Environmental Science 2*, 638-654.

[17] Zhang, W.-J. (2011) A review of the electrochemical performance of alloy anodes for lithium-ion batteries, *Journal of Power Sources 196*, 13-24.

[18] Broussely, M., Biensan, P., and Simon, B. (1999) Lithium insertion into host materials: the key to success for Li ion batteries, *Electrochimica Acta 45*, 3-22.

[19] De las Casas, C., and Li, W. (2012) A review of application of carbon nanotubes for lithium ion battery anode material, *Journal of Power Sources 208*, 74-85.

[20] Long, J. W., Dunn, B., Rolison, D. R., and White, H. S. (2004) Three-dimensional battery architectures, *Chemical Reviews 104*, 4463-4492.

[21] Kim, S.-S., Kadoma, Y., Ikuta, H., Uchimoto, Y., and Wakihara, M. (2001) Electrochemical performance of natural graphite by surface modification using aluminum, *Electrochemical and Solid-State Letters 4*, A109-A112.

[22] Arthur, T. S., Bates, D. J., Cirigliano, N., Johnson, D. C., Malati, P., Mosby, J. M., Perre, E., Rawls, M. T., Prieto, A. L., and Dunn, B. (2011) Three-dimensional electrodes and battery architectures, *Mrs Bulletin 36*, 523-531.

[23] Candelaria, S. L., Shao, Y., Zhou, W., Li, X., Xiao, J., Zhang, J.-G., Wang, Y., Liu, J., Li, J., and Cao, G. (2012) Nanostructured carbon for energy storage and conversion, *Nano Energy 1*, 195-220.

[24] Rolison, D. R., Long, J. W., Lytle, J. C., Fischer, A. E., Rhodes, C. P., McEvoy, T. M., Bourg, M. E., and Lubers, A. M. (2009) Multifunctional 3D nanoarchitectures for energy storage and conversion, *Chemical Society Reviews 38*, 226-252.

[25] Hayner, C. M., Zhao, X., and Kung, H. H. (2012) Materials for rechargeable lithium-ion batteries, *Annual review of chemical and biomolecular engineering 3*, 445-471.

[26] Zhang, H., Yu, X., and Braun, P. V. (2011) Three-dimensional bicontinuous ultrafast-charge and-discharge bulk battery electrodes, *Nature nanotechnology 6*, 277-281.

[27] Roberts, M., Johns, P., Owen, J., Brandell, D., Edstrom, K., El Enany, G., Guery, C., Golodnitsky, D., Lacey, M., and Lecoeur, C. (2011) 3D lithium ion batteries—from fundamentals to fabrication, *Journal of Materials Chemistry 21*, 9876-9890.

[28] Dong, X.-C., Xu, H., Wang, X.-W., Huang, Y.-X., Chan-Park, M. B., Zhang, H., Wang, L.-H., Huang, W., and Chen, P. (2012) 3D graphene–cobalt oxide electrode for high-performance supercapacitor and enzymeless glucose detection, *ACS nano 6*, 3206-3213.

[29] Dunn, B., Long, J. W., and Ronson, D. R. (2008) Rethinking multifunction in three dimensions for miniaturizing electrical energy storage, *The Electrochemical Society Interface 17*, 49.

[30] Jiang, H., Lee, P. S., and Li, C. (2013) 3D carbon based nanostructures for advanced supercapacitors, *Energy & Environmental Science 6*, 41-53.

[31] Luo, J., Liu, J., Zeng, Z., Ng, C. F., Ma, L., Zhang, H., Lin, J., Shen, Z., and Fan, H. J. (2013) Three-dimensional graphene foam supported Fe3O4 lithium battery anodes with long cycle life and high rate capability, *Nano letters 13*, 6136-6143.

[32] Wang, G., Wang, B., Wang, X., Park, J., Dou, S., Ahn, H., and Kim, K. (2009) Sn/graphene nanocomposite with 3D architecture for enhanced reversible lithium storage in lithium ion batteries, *Journal of Materials Chemistry 19*, 8378-8384.

[33] Rai, A. K., Gim, J., Anh, L. T., and Kim, J. (2013) Partially reduced Co 3 O 4/graphene nanocomposite as an anode material for secondary lithium ion battery, *Electrochimica Acta 100*, 63-71.

[34] Avouris, P., and Dimitrakopoulos, C. (2012) Graphene: synthesis and applications, *Materials Today 15*, 86-97.

[35] Lian, P., Zhu, X., Xiang, H., Li, Z., Yang, W., and Wang, H. (2010) Enhanced cycling performance of Fe 3 O 4–graphene nanocomposite as an anode material for lithium-ion batteries, *Electrochimica Acta 56*, 834-840.

[36] Lian, P., Zhu, X., Liang, S., Li, Z., Yang, W., and Wang, H. (2010) Large reversible capacity of high quality graphene sheets as an anode material for lithium-ion batteries, *Electrochimica Acta 55*, 3909-3914.

[37] Pan, D., Wang, S., Zhao, B., Wu, M., Zhang, H., Wang, Y., and Jiao, Z. (2009) Li storage properties of disordered graphene nanosheets, *Chemistry of Materials 21*, 3136-3142.

[38] Omichi, K., Ramos-Sanchez, G., Rao, R., Pierce, N., Chen, G., Balbuena, P., and Harutyunyan, A. (2015) Origin of excess irreversible capacity in lithium-ion batteries based on carbon nanostructures, *Journal of The Electrochemical Society 162*, A2106-A2115.

[39] Lu, W., Chen, Z., Joachin, H., Prakash, J., Liu, J., and Amine, K. (2007) Thermal and electrochemical characterization of MCMB/LiNi1/3Co1/3Mn1/3O2 using LiBoB as an electrolyte additive, *Journal of power sources 163*, 1074-1079.

[40] Libich, J., Vondrak, J., Sedlarikova, M., Maca, J., and Frk, M. (2013) Suppressing of Irreversible Capacity in Lithium-ion Batteries, *Portugaliae Electrochimica Acta 31*, 297-306.

[41] Mukai, S. R., Hasegawa, T., Takagi, M., and Tamon, H. (2004) Reduction of irreversible capacities of amorphous carbon materials for lithium ion battery anodes by Li2CO3 addition, *Carbon 42*, 837-842.

[42] Cao, H., Zhou, X., Deng, W., and Liu, Z. (2016) A compressible and hierarchical porous graphene/Co composite aerogel for lithium-ion batteries with high gravimetric/volumetric capacity, *Journal of Materials Chemistry A 4*, 6021-6028.

[43] Wang, X., Lv, L., Cheng, Z., Gao, J., Dong, L., Hu, C., and Qu, L. (2016) High‐Density Monolith of N‐Doped Holey Graphene for Ultrahigh Volumetric Capacity of Li‐Ion Batteries, *Advanced Energy Materials 6*.

[44] Landi, B. J., Cress, C. D., and Raffaelle, R. P. (2010) High energy density lithium-ion batteries with carbon nanotube anodes, *Journal of Materials Research 25*, 1636-1644.

[45] Huang, G., Chen, T., Wang, Z., Chang, K., and Chen, W. (2013) Synthesis and electrochemical performances of cobalt sulfides/graphene nanocomposite as anode material of Li-ion battery, *Journal of Power Sources 235*, 122-128.

[46] Cao, K., Jiao, L., Liu, H., Liu, Y., Wang, Y., Guo, Z., and Yuan, H. (2015) 3D Hierarchical Porous α‐Fe2O3 Nanosheets for High‐Performance Lithium‐Ion Batteries, *Advanced Energy Materials 5*.

[47] Xiao, X., Liu, P., Wang, J. S., Verbrugge, M., and Balogh, M. P. (2011) Vertically aligned graphene electrode for lithium ion battery with high rate capability, *Electrochemistry Communications 13*, 209-212.

[48] Li, N., Jin, S., Liao, Q., Cui, H., and Wang, C. (2014) Encapsulated within graphene shell silicon nanoparticles anchored on vertically aligned graphene trees as lithium ion battery anodes, *Nano energy 5*, 105-115.

[49] Li, N., Song, H., Cui, H., and Wang, C. (2014) Sn@ graphene grown on vertically aligned graphene for high-capacity, high-rate, and long-life lithium storage, *Nano Energy 3*, 102-112.

[50] Liu, Y., Wang, W., Gu, L., Wang, Y., Ying, Y., Mao, Y., Sun, L., and Peng, X. (2013) Flexible CuO nanosheets/reduced-graphene oxide composite paper: binder-free anode for

high-performance lithium-ion batteries, *ACS applied materials & interfaces 5*, 9850-9855.

[51] Kim, H.-J., Lee, S. E., Lee, J., Jung, J.-Y., Lee, E.-S., Choi, J.-H., Jung, J.-H., Oh, M., Hyun, S., and Choi, D.-G. (2014) Gold-coated silicon nanowire–graphene core–shell composite film as a polymer binder-free anode for rechargeable lithium-ion batteries, *Physica E: Low-dimensional Systems and Nanostructures 61*, 204-209.

[52] Du, Y., Zhu, X., Zhou, X., Hu, L., Dai, Z., and Bao, J. (2015) Co 3 S 4 porous nanosheets embedded in graphene sheets as high-performance anode materials for lithium and sodium storage, *Journal of Materials Chemistry A 3*, 6787-6791.

[53] Wu, P., Wang, H., Tang, Y., Zhou, Y., and Lu, T. (2014) Three-dimensional interconnected network of graphene-wrapped porous silicon spheres: in situ magnesiothermic-reduction synthesis and enhanced lithium-storage capabilities, *ACS applied materials & interfaces 6*, 3546-3552.

[54] Ji, J., Ji, H., Zhang, L. L., Zhao, X., Bai, X., Fan, X., Zhang, F., and Ruoff, R. S. (2013) Graphene‐Encapsulated Si on Ultrathin‐Graphite Foam as Anode for High Capacity Lithium‐Ion Batteries, *Advanced Materials 25*, 4673-4677.

[55] Zhu, Y., Liu, W., Zhang, X., He, J., Chen, J., Wang, Y., and Cao, T. (2013) Directing silicon–graphene self-assembly as a core/shell anode for high-performance lithium-ion batteries, *Langmuir 29*, 744-749.

[56] Li, X., Zhang, Y., Li, T., Zhong, Q., Li, H., and Huang, J. (2014) Graphene nanoscrolls encapsulated TiO 2 (B) nanowires for lithium storage, *Journal of Power Sources 268*, 372-378.

[57] Zeng, F., Kuang, Y., Wang, Y., Huang, Z., Fu, C., and Zhou, H. (2011) Facile Preparation of High‐Quality Graphene Scrolls from Graphite Oxide by a Microexplosion Method, *Advanced Materials 23*, 4929-4932.

[58] Zeng, F., Kuang, Y., Liu, G., Liu, R., Huang, Z., Fu, C., and Zhou, H. (2012) Supercapacitors based on high-quality graphene scrolls, *Nanoscale 4*, 3997-4001.

[59] Wang, R., Xu, C., Sun, J., Gao, L., and Lin, C. (2013) Flexible free-standing hollow Fe 3 O 4/graphene hybrid films for lithium-ion batteries, *Journal of Materials Chemistry A 1*, 1794-1800.

[60] Luo, J., Jang, H. D., Sun, T., Xiao, L., He, Z., Katsoulidis, A. P., Kanatzidis, M. G., Gibson, J. M., and Huang, J. (2011) Compression and aggregation-resistant particles of crumpled soft sheets, *Acs Nano 5*, 8943-8949.

[61] Luo, J., Jang, H. D., and Huang, J. (2013) Effect of sheet morphology on the scalability of graphene-based ultracapacitors, *ACS nano 7*, 1464-1471.

[62] Gong, Y., Yang, S., Liu, Z., Ma, L., Vajtai, R., and Ajayan, P. M. (2013) Graphene‐Network‐Backboned Architectures for High‐Performance Lithium Storage, *Advanced Materials 25*, 3979-3984.

[63] Zhang, H., Xie, A., Wang, C., Wang, H., Shen, Y., and Tian, X. (2013) Novel rGO/α-Fe 2 O 3 composite hydrogel: synthesis, characterization and high performance of electromagnetic wave absorption, *Journal of Materials Chemistry A 1*, 8547-8552.

[64] Zhang, Z., Xiao, F., Guo, Y., Wang, S., and Liu, Y. (2013) One-pot self-assembled three-dimensional TiO2-graphene hydrogel with improved adsorption capacities and photocatalytic and electrochemical activities, *ACS applied materials & interfaces 5*, 2227-2233.

[65] Qiu, B., Xing, M., and Zhang, J. (2014) Mesoporous TiO2 nanocrystals grown in situ on graphene aerogels for high photocatalysis and lithium-ion batteries, *Journal of the American Chemical Society 136*, 5852-5855.

[66] Huang, Z. X., Wang, Y., Zhu, Y. G., Shi, Y., Wong, J. I., and Yang, H. Y. (2014) 3D graphene supported MoO 2 for high performance binder-free lithium ion battery, *Nanoscale 6*, 9839-9845.

[67] Wang, R., Xu, C., Sun, J., Gao, L., and Yao, H. (2014) Solvothermal-induced 3D macroscopic SnO2/nitrogen-doped graphene aerogels for high capacity and long-life lithium storage, *ACS applied materials & interfaces 6*, 3427-3436.

[68] Li, X., Geng, D., Zhang, Y., Meng, X., Li, R., and Sun, X. (2011) Superior cycle stability of nitrogen-doped graphene nanosheets as anodes for lithium ion batteries, *Electrochemistry Communications 13*, 822-825.

[69] Wu, Z.-S., Ren, W., Xu, L., Li, F., and Cheng, H.-M. (2011) Doped graphene sheets as anode materials with superhigh rate and large capacity for lithium ion batteries, *ACS nano 5*, 5463-5471.

[70] Sahoo, M., Sreena, K., Vinayan, B., and Ramaprabhu, S. (2015) Green synthesis of boron doped graphene and its application as high performance anode material in Li ion battery, *Materials Research Bulletin 61*, 383-390.

[71] Reddy, A. L. M., Srivastava, A., Gowda, S. R., Gullapalli, H., Dubey, M., and Ajayan, P. M. (2010) Synthesis of nitrogen-doped graphene films for lithium battery application, *ACS nano 4*, 6337-6342.

[72] Wang, X., Cao, X., Bourgeois, L., Guan, H., Chen, S., Zhong, Y., Tang, D. M., Li, H., Zhai, T., and Li, L. (2012) N‐Doped Graphene‐SnO2 Sandwich Paper for High‐Performance Lithium‐Ion Batteries, *Advanced Functional Materials 22*, 2682-2690.

[73] Chang, Y., Li, J., Wang, B., Luo, H., He, H., Song, Q., and Zhi, L. (2013) Synthesis of 3D nitrogen-doped graphene/Fe 3 O 4 by a metal ion induced self-assembly process for high-performance Li-ion batteries, *Journal of Materials Chemistry A 1*, 14658-14665.

[74] Zhang, K., Han, P., Gu, L., Zhang, L., Liu, Z., Kong, Q., Zhang, C., Dong, S., Zhang, Z., and Yao, J. (2012) Synthesis of nitrogen-doped MnO/graphene nanosheets hybrid material for lithium ion batteries, *ACS applied materials & interfaces 4*, 658-664.

[75] Meng, Y. S., and Arroyo-de Dompablo, M. E. (2009) First principles computational materials design for energy storage materials in lithium ion batteries, *Energy & Environmental Science 2*, 589-609.

[76] Zhang, T., Li, D., Tao, Z., and Chen, J. (2013) Understanding electrode materials of rechargeable lithium batteries via DFT calculations, *Progress in Natural Science: Materials International 23*, 256-272.

[77] Yamakawa, N., Jiang, M., Key, B., and Grey, C. P. (2009) Identifying the local structures formed during lithiation of the conversion material, iron fluoride, in a Li ion battery: a solid-state NMR, X-ray diffraction, and pair distribution function analysis study, *Journal of the American Chemical Society 131*, 10525-10536.

[78] Park, S., and Ruoff, R. S. (2009) Chemical methods for the production of graphenes, *Nature nanotechnology 4*, 217-224.

[79] Yoo, E., Kim, J., Hosono, E., Zhou, H.-s., Kudo, T., and Honma, I. (2008) Large reversible Li storage of graphene nanosheet families for use in rechargeable lithium ion batteries, *Nano letters 8*, 2277-2282.

[80] Cai, D., Ding, L., Wang, S., Li, Z., Zhu, M., and Wang, H. (2014) Facile synthesis of ultrathin-shell graphene hollow spheres for high-performance lithium-ion batteries, *Electrochimica Acta 139*, 96-103.

[81] Choi, B. G., Yang, M., Hong, W. H., Choi, J. W., and Huh, Y. S. (2012) 3D macroporous graphene frameworks for supercapacitors with high energy and power densities, *ACS nano 6*, 4020-4028.

[82] Park, S.-H., Kim, H.-K., Yoon, S.-B., Lee, C.-W., Ahn, D., Lee, S.-I., Roh, K. C., and Kim, K.-B. (2015) Spray-assisted deep-frying process for the in situ spherical assembly of graphene for energy-storage devices, *Chemistry of Materials 27*, 457-465.

[83] Fan, Z., Yan, J., Ning, G., Wei, T., Zhi, L., and Wei, F. (2013) Porous graphene networks as high performance anode materials for lithium ion batteries, *Carbon 60*, 558-561.

[84] Vickery, J. L., Patil, A. J., and Mann, S. (2009) Fabrication of Graphene‐Polymer Nanocomposites With Higher‐Order Three‐Dimensional Architectures, *Advanced Materials 21*, 2180-2184.

[85] Yang, S., Feng, X., Zhi, L., Cao, Q., Maier, J., and Müllen, K. (2010) Nanographene‐constructed hollow carbon spheres and their favorable electroactivity with respect to lithium storage, *Advanced Materials 22*, 838-842.

[86] Yin, S., Zhang, Y., Kong, J., Zou, C., Li, C. M., Lu, X., Ma, J., Boey, F. Y. C., and Chen, X. (2011) Assembly of graphene sheets into hierarchical structures for high-performance energy storage, *Acs Nano 5*, 3831-3838.

[87] Stankovich, S., Dikin, D. A., Dommett, G. H., Kohlhaas, K. M., Zimney, E. J., Stach, E. A., Piner, R. D., Nguyen, S. T., and Ruoff, R. S. (2006) Graphene-based composite materials, *nature 442*, 282-286.

[88] Singhal, A., Dubey, K., Bhardwaj, Y., Jain, D., Choudhury, S., and Tyagi, A. (2013) UV-shielding transparent PMMA/In 2 O 3 nanocomposite films based on In 2 O 3 nanoparticles, *RSC Advances 3*, 20913-20921.

[89] Guo, Z., Henry, L. L., Palshin, V., and Podlaha, E. J. (2006) Synthesis of poly (methyl methacrylate) stabilized colloidal zero-valence metallic nanoparticles, *Journal of Materials Chemistry 16*, 1772-1777.

[90] Safiullah, S. M., Wasi, K. A., and Basha, K. A. (2015) Synthesis of poly (glycidyl methacrylate)–copper nanocomposite beads by in-situ suspension polymerization and deposition method–A comparative study, *Polymer 66*, 29-37.

[91] Wu, X., and Shi, G. (2005) Synthesis of a carboxyl-containing conducting oligomer and non-covalent sidewall functionalization of single-walled carbon nanotubes, *Journal of Materials Chemistry 15*, 1833-1837.

[92] Xiao, W., Zhao, P., Deng, S., and Zhang, N. (2015) Anchoring H 3 PW 12 O 40 on 3-aminopropyltriethoxysilane modified graphene oxide: enhanced adsorption capacity and photocatalytic activity toward methyl orange, *New Journal of Chemistry 39*, 3719-3727.

[93] Li, W., Tang, X.-Z., Zhang, H.-B., Jiang, Z.-G., Yu, Z.-Z., Du, X.-S., and Mai, Y.-W. (2011) Simultaneous surface functionalization and reduction of graphene oxide with octadecylamine for electrically conductive polystyrene composites, *Carbon 49*, 4724-4730.

[94] Petit, C. (2012) *Factors Affecting the Removal of Ammonia from Air on Carbonaceous Materials: Investigation of Reactive Adsorption Mechanism*, Springer Science & Business Media.

[95] Chakraborty, S., Saha, S., Dhanak, V., Biswas, K., Barbezat, M., Terrasi, G. P., and Chakraborty, A. K. (2016) High yield synthesis of amine functionalized graphene oxide and its surface properties, *RSC Advances 6*, 67916-67924.

[96] Jin, M., Jeong, H.-K., Kim, T.-H., So, K. P., Cui, Y., Yu, W. J., Ra, E. J., and Lee, Y. H. (2010) Synthesis and systematic characterization of functionalized graphene sheets generated by thermal exfoliation at low temperature, *Journal of Physics D: Applied Physics 43*, 275402.

[97] He, H., Klinowski, J., Forster, M., and Lerf, A. (1998) A new structural model for graphite oxide, *Chemical physics letters 287*, 53-56.

[98] Dai, Y., Pang, H., Huang, J., Yang, Y., Huang, H., Wang, K., Ma, Z., and Liao, B. (2016) Tailoring of ammonia reduced graphene oxide into amine functionalized graphene quantum dots through a Hofmann rearrangement, *Rsc Advances 6*, 34514-34520.

[99] Baldovino, F., Quitain, A., Dugos, N. P., Roces, S. A., Koinuma, M., Yuasa, M., and Kida, T. (2016) Synthesis and characterization of nitrogen-functionalized graphene oxide in high-temperature and high-pressure ammonia, *RSC Advances 6*, 113924-113932.

[100] Zhu, Y., Murali, S., Cai, W., Li, X., Suk, J. W., Potts, J. R., and Ruoff, R. S. (2010) Graphene and graphene oxide: synthesis, properties, and applications, *Advanced materials 22*, 3906-3924.

[101] Zheng, C., Zhou, X., Cao, H., Wang, G., and Liu, Z. (2015) Nitrogen-doped porous graphene–activated carbon composite derived from “bucky gels” for supercapacitors, *RSC Advances 5*, 10739-10745.

[102] Xing, Z., Ju, Z., Zhao, Y., Wan, J., Zhu, Y., Qiang, Y., and Qian, Y. (2016) One-pot hydrothermal synthesis of Nitrogen-doped graphene as high-performance anode materials for lithium ion batteries, *Scientific reports 6*.

[103] Neimark, A. V. (1995) The method of indeterminate Lagrange multipliers in nonlocal density functional theory, *Langmuir 11*, 4183-4184.

[104] Xiang, F., Mukherjee, R., Zhong, J., Xia, Y., Gu, N., Yang, Z., and Koratkar, N. (2015) Scalable and rapid far infrared reduction of graphene oxide for high performance lithium ion batteries, *Energy Storage Materials 1*, 9-16.

[105] Xiang, F., Zhong, J., Gu, N., Mukherjee, R., Oh, I.-K., Koratkar, N., and Yang, Z. (2014) Far-infrared reduced graphene oxide as high performance electrodes for supercapacitors, *Carbon 75*, 201-208.

[106] Hu, T., Sun, X., Sun, H., Xin, G., Shao, D., Liu, C., and Lian, J. (2014) Rapid synthesis of nitrogen-doped graphene for a lithium ion battery anode with excellent rate performance and super-long cyclic stability, *Physical Chemistry Chemical Physics 16*, 1060-1066.

[107] Bi, H., Liu, Z., Xu, F., Tang, Y., Lin, T., and Huang, F. (2016) Three-dimensional porous graphene-like carbon cloth from cotton as a free-standing lithium-ion battery anode, *Journal of Materials Chemistry A 4*, 11762-11767.

[108] Sui, Z.-Y., Wang, C., Yang, Q.-S., Shu, K., Liu, Y.-W., Han, B.-H., and Wallace, G. G. (2015) A highly nitrogen-doped porous graphene–an anode material for lithium ion batteries, *Journal of Materials Chemistry A 3*, 18229-18237.

[109] Shu, K., Wang, C., Li, S., Zhao, C., Yang, Y., Liu, H., and Wallace, G. (2015) Flexible free-standing graphene paper with interconnected porous structure for energy storage, *Journal of Materials Chemistry A 3*, 4428-4434.

[110] Zhang, L., Zhang, M., Wang, Y., Zhang, Z., Kan, G., Wang, C., Zhong, Z., and Su, F. (2014) Graphitized porous carbon microspheres assembled with carbon black nanoparticles as improved anode materials in Li-ion batteries, *Journal of Materials Chemistry A 2*, 10161-10168.

[111] Li, D., Ding, L.-X., Chen, H., Wang, S., Li, Z., Zhu, M., and Wang, H. (2014) Novel nitrogen-rich porous carbon spheres as a high-performance anode material for lithium-ion batteries, *Journal of Materials Chemistry A 2*, 16617-16622.

[112] Liu, X., Zhang, J., Guo, S., and Pinna, N. (2016) Graphene/N-doped carbon sandwiched nanosheets with ultrahigh nitrogen doping for boosting lithium-ion batteries, *Journal of Materials Chemistry A 4*, 1423-1431.

[113] Liu, F., Song, S., Xue, D., and Zhang, H. (2012) Folded structured graphene paper for high performance electrode materials, *Advanced Materials 24*, 1089-1094.

[114] Zhao, X., Hayner, C. M., Kung, M. C., and Kung, H. H. (2011) Flexible holey graphene paper electrodes with enhanced rate capability for energy storage applications, *ACS nano 5*, 8739-8749.

[115] Fang, Y., Lv, Y., Che, R., Wu, H., Zhang, X., Gu, D., Zheng, G., and Zhao, D. (2013) Two-dimensional mesoporous carbon nanosheets and their derived graphene nanosheets: synthesis and efficient lithium ion storage, *Journal of the American Chemical Society 135*, 1524-1530.

[116] Fan, Z.-J., Yan, J., Wei, T., Ning, G.-Q., Zhi, L.-J., Liu, J.-C., Cao, D.-X., Wang, G.-L., and Wei, F. (2011) Nanographene-constructed carbon nanofibers grown on graphene sheets by chemical vapor deposition: high-performance anode materials for lithium ion batteries, *ACS nano 5*, 2787-2794.

[117] Adelhelm, P., Hu, Y. S., Chuenchom, L., Antonietti, M., Smarsly, B. M., and Maier, J. (2007) Generation of Hierarchical Meso‐and Macroporous Carbon from Mesophase Pitch by Spinodal Decomposition using Polymer Templates, *Advanced Materials 19*, 4012-4017.

[118] Wang, Z.-L., Xu, D., Wang, H.-G., Wu, Z., and Zhang, X.-B. (2013) In situ fabrication of porous graphene electrodes for high-performance energy storage, *ACS nano 7*, 2422-2430.

[119] Mukherjee, R., Thomas, A. V., Krishnamurthy, A., and Koratkar, N. (2012) Photothermally reduced graphene as high-power anodes for lithium-ion batteries, *Acs Nano 6*, 7867-7878.

[120] Chen, X., Kierzek, K., Jiang, Z., Chen, H., Tang, T., Wojtoniszak, M., Kalenczuk, R. J., Chu, P. K., and Borowiak-Palen, E. (2011) Synthesis, growth mechanism, and electrochemical properties of hollow mesoporous carbon spheres with controlled diameter, *The Journal of Physical Chemistry C 115*, 17717-17724.

[121] Yang, S., Feng, X., Wang, L., Tang, K., Maier, J., and Müllen, K. (2010) Graphene‐Based Nanosheets with a Sandwich Structure, *Angewandte Chemie International Edition 49*, 4795-4799.

[122] Yan, Y., Yin, Y.-X., Xin, S., Guo, Y.-G., and Wan, L.-J. (2012) Ionothermal synthesis of sulfur-doped porous carbons hybridized with graphene as superior anode materials for lithium-ion batteries, *Chemical Communications 48*, 10663-10665.

[123] Chen, D., Ji, G., Ma, Y., Lee, J. Y., and Lu, J. (2011) Graphene-encapsulated hollow Fe3O4 nanoparticle aggregates as a high-performance anode material for lithium ion batteries, *ACS applied materials & interfaces 3*, 3078-3083.

[124] Zhang, L., Wu, H. B., and Lou, X. W. D. (2014) Iron‐oxide‐based advanced anode materials for lithium‐ion batteries, *Advanced Energy Materials 4*.

[125] Yang, S., Sun, Y., Chen, L., Hernandez, Y., Feng, X., and Müllen, K. (2012) Porous iron oxide ribbons grown on graphene for high-performance lithium storage, *Scientific reports 2*.

[126] He, C., Wu, S., Zhao, N., Shi, C., Liu, E., and Li, J. (2013) Carbon-encapsulated Fe3O4 nanoparticles as a high-rate lithium ion battery anode material, *ACS nano 7*, 4459-4469.

[127] Zhang, Q., Shi, Z., Deng, Y., Zheng, J., Liu, G., and Chen, G. (2012) Hollow Fe3O4/C spheres as superior lithium storage materials, *Journal of power sources 197*, 305-309.

[128] Zhang, W. M., Wu, X. L., Hu, J. S., Guo, Y. G., and Wan, L. J. (2008) Carbon Coated Fe3O4 Nanospindles as a Superior Anode Material for Lithium‐Ion Batteries, *Advanced Functional Materials 18*, 3941-3946.

[129] Li, B., Cao, H., Shao, J., Qu, M., and Warner, J. H. (2011) Superparamagnetic Fe 3 O 4 nanocrystals@ graphene composites for energy storage devices, *Journal of Materials Chemistry 21*, 5069-5075.

[130] Wang, Y., Zhang, L., Gao, X., Mao, L., Hu, Y., and Lou, X. W. D. (2014) One‐Pot Magnetic Field Induced Formation of Fe3O4/C Composite Microrods with Enhanced Lithium Storage Capability, *Small 10*, 2815-2819.

[131] Yang, S., Cao, C., Li, G., Sun, Y., Huang, P., Wei, F., and Song, W. (2015) Improving the electrochemical performance of Fe 3 O 4 nanoparticles via a double protection strategy through carbon nanotube decoration and graphene networks, *Nano Research 8*, 1339-1347.

[132] Zhang, K., Zhao, W., Lee, J.-T., Jang, G., Shi, X., and Park, J. H. (2014) A magnetic field assisted self-assembly strategy towards strongly coupled Fe 3 O 4 nanocrystal/rGO paper for high-performance lithium ion batteries, *Journal of Materials Chemistry A 2*, 9636-9644.

[133] Wu, Z.-S., Ren, W., Gao, L., Liu, B., Jiang, C., and Cheng, H.-M. (2009) Synthesis of high-quality graphene with a pre-determined number of layers, *Carbon 47*, 493-499.

[134] Billaud, J., Bouville, F., Magrini, T., Villevieille, C., and Studart, A. R. (2016) Magnetically aligned graphite electrodes for high-rate performance Li-ion batteries, *Nature Energy 1*, 16097.

[135] Cui, P., Lee, J., Hwang, E., and Lee, H. (2011) One-pot reduction of graphene oxide at subzero temperatures, *Chemical Communications 47*, 12370-12372.

[136] Lv, W., Tang, D.-M., He, Y.-B., You, C.-H., Shi, Z.-Q., Chen, X.-C., Chen, C.-M., Hou, P.-X., Liu, C., and Yang, Q.-H. (2009) Low-temperature exfoliated graphenes: vacuum-promoted exfoliation and electrochemical energy storage, *ACS nano 3*, 3730-3736.

[137] Gupta, A., Singh, A. P., Varshney, S., Agrawal, N., Sambyal, P., Pandey, Y., Singh, B. P., Singh, V., Gupta, B. K., and Dhawan, S. (2014) New insight into the shape-controlled

synthesis and microwave shielding properties of iron oxide covered with reduced graphene oxide, *Rsc Advances 4*, 62413-62422.

[138] Bhuvaneswari, S., Pratheeksha, P. M., Anandan, S., Rangappa, D., Gopalan, R., and Rao, T. N. (2014) Efficient reduced graphene oxide grafted porous Fe 3 O 4 composite as a high performance anode material for Li-ion batteries, *Physical Chemistry Chemical Physics 16*, 5284-5294.

[139] Deng, H., Li, X., Peng, Q., Wang, X., Chen, J., and Li, Y. (2005) Monodisperse magnetic single‐crystal ferrite microspheres, *Angewandte Chemie 117*, 2842-2845.

[140] Zhu, T., Chen, J. S., and Lou, X. W. (2011) Glucose-assisted one-pot synthesis of FeOOH nanorods and their transformation to Fe3O4@ carbon nanorods for application in lithium ion batteries, *The Journal of Physical Chemistry C 115*, 9814-9820.

[141] Kwon, Y., Kim, H., Doo, S.-G., and Cho, J. (2007) Sn0. 9Si0. 1/carbon core-shell nanoparticles for high-density lithium storage materials, *Chemistry of materials 19*, 982-986.

[142] Kim, H., Seo, M., Park, M. H., and Cho, J. (2010) A critical size of silicon nano‐anodes for lithium rechargeable batteries, *Angewandte Chemie International Edition 49*, 2146-2149.

[143] Chen, Y., He, L., Shang, P., Tang, Q., Liu, Z., Liu, H., and Zhou, L. (2011) Micro-sized and nano-sized Fe3O4 particles as anode materials for lithium-ion batteries, *Journal of Materials Science & Technology 27*, 41-45.

[144] Li, H., Shi, L., Lu, W., Huang, X., and Chen, L. (2001) Studies on capacity loss and capacity fading of nanosized SnSb alloy anode for Li-ion batteries, *Journal of The Electrochemical Society 148*, A915-A922.

[145] Taberna, P.-L., Mitra, S., Poizot, P., Simon, P., and Tarascon, J.-M. (2006) High rate capabilities Fe3O4-based Cu nano-architectured electrodes for lithium-ion battery applications, *Nature materials 5*, 567-573.

[146] Zhou, J., Ma, L., Song, H., Wu, B., and Chen, X. (2011) Durable high-rate performance of CuO hollow nanoparticles/graphene-nanosheet composite anode material for lithium-ion batteries, *Electrochemistry Communications 13*, 1357-1360.

[147] Do, J.-S., and Weng, C.-H. (2005) Preparation and characterization of CoO used as anodic material of lithium battery, *Journal of Power Sources 146*, 482-486.

[148] Zhang, M., and Jia, M. (2013) High rate capability and long cycle stability Fe 3 O 4–graphene nanocomposite as anode material for lithium ion batteries, *Journal of Alloys and Compounds 551*, 53-60.

[149] Zhou, J., Song, H., Ma, L., and Chen, X. (2011) Magnetite/graphene nanosheet composites: interfacial interaction and its impact on the durable high-rate performance in lithium-ion batteries, *Rsc Advances 1*, 782-791.

[150] Zhang, W., Li, X., Liang, J., Tang, K., Zhu, Y., and Qian, Y. (2016) One-step thermolysis synthesis of two-dimensional ultrafine Fe 3 O 4 particles/carbon nanonetworks for high-performance lithium-ion batteries, *Nanoscale 8*, 4733-4741.

[151] Zhai, L. (2013) Stimuli-responsive polymer films, *Chemical Society Reviews 42*, 7148-7160.

[152] Qiu, L., Liu, D., Wang, Y., Cheng, C., Zhou, K., Ding, J., Truong, V. T., and Li, D. (2014) Mechanically Robust, Electrically Conductive and Stimuli‐Responsive Binary Network Hydrogels Enabled by Superelastic Graphene Aerogels, *Advanced Materials 26*, 3333-3337.

[153] De las Heras Alarcón, C., Pennadam, S., and Alexander, C. (2005) Stimuli responsive polymers for biomedical applications, *Chemical Society Reviews 34*, 276-285.

[154] Mendenhall, G. D., Geng, Y., and Hwang, J. (1996) Optimization of long-term stability of magnetic fluids from magnetite and synthetic polyelectrolytes, *Journal of colloid and interface science 184*, 519-526.

[155] Wang, X., Ye, X., and Zhang, G. (2015) Investigation of pH-induced conformational change and hydration of poly (methacrylic acid) by analytical ultracentrifugation, *Soft Matter 11*, 5381-5388.

[156] Zhang, J., and Peppas, N. A. (2000) Synthesis and characterization of pH-and temperature-sensitive poly (methacrylic acid)/poly (N-isopropylacrylamide) interpenetrating polymeric networks, *Macromolecules 33*, 102-107.

[157] de Moura, M. R., Aouada, F. A., and Mattoso, L. H. (2008) Preparation of chitosan nanoparticles using methacrylic acid, *Journal of Colloid and Interface Science 321*, 477-483.

[158] Etika, K. C., Cox, M. A., and Grunlan, J. C. (2010) Tailored dispersion of carbon nanotubes in water with pH-responsive polymers, *Polymer 51*, 1761-1770.

[159] Wei, W., Yang, S., Zhou, H., Lieberwirth, I., Feng, X., and Müllen, K. (2013) 3D Graphene Foams Cross‐linked with Pre‐encapsulated Fe3O4 Nanospheres for Enhanced Lithium Storage, *Advanced materials 25*, 2909-2914.

[160] Wei, H., Yang, W., Xi, Q., and Chen, X. (2012) Preparation of Fe3O4@ graphene oxide core–shell magnetic particles for use in protein adsorption, *Materials Letters 82*, 224-226.

[161] Zhao, X., Yang, L., Li, X., Jia, X., Liu, L., Zeng, J., Guo, J., and Liu, P. (2015) Functionalized graphene oxide nanoparticles for cancer cell-specific delivery of antitumor drug, *Bioconjugate chemistry 26*, 128-136.

[162] Gao, T., Ye, Q., Pei, X., Xia, Y., and Zhou, F. (2013) Grafting polymer brushes on graphene oxide for controlling surface charge states and templated synthesis of metal nanoparticles, *Journal of Applied Polymer Science 127*, 3074-3083.

[163] Wang, H., Xie, J., Follette, M., Back, T. C., and Amama, P. B. (2016) Magnetic field-induced fabrication of Fe 3 O 4/graphene nanocomposites for enhanced electrode performance in lithium-ion batteries, *RSC Advances 6*, 83117-83125.

[164] Wang, H., Li, X., Baker-Fales, M., and Amama, P. B. (2016) 3D graphene-based anode materials for Li-ion batteries, *Current Opinion in Chemical Engineering 13*, 124-132.

[165] Li, L., Kovalchuk, A., Fei, H., Peng, Z., Li, Y., Kim, N. D., Xiang, C., Yang, Y., Ruan, G., and Tour, J. M. (2015) Enhanced Cycling Stability of Lithium‐Ion Batteries Using Graphene‐Wrapped Fe3O4‐Graphene Nanoribbons as Anode Materials, *Advanced Energy Materials 5*.

[166] Zhao, L., Gao, M., Yue, W., Jiang, Y., Wang, Y., Ren, Y., and Hu, F. (2015) Sandwich-structured graphene-Fe3O4@ carbon nanocomposites for high-performance lithium-ion batteries, *ACS applied materials & interfaces 7*, 9709-9715.

[167] Fan, X., Li, S., Zhou, H., and Lu, L. (2015) One-pot high temperature hydrothermal synthesis of Fe3O4@ C/graphene nanocomposite as anode for high rate lithium ion battery, *Electrochimica Acta 180*, 1041-1049.

[168] Ren, M., Yang, M., Liu, W., Li, M., Su, L., Qiao, C., Wu, X., and Ma, H. (2016) Ultra-small Fe3O4 nanocrystals decorated on 2D graphene nanosheets with excellent cycling stability as anode materials for lithium ion batteries, *Electrochimica Acta 194*, 219-227.

[169] Chen, Y., Song, B., Lu, L., and Xue, J. (2013) Ultra-small Fe 3 O 4 nanoparticle decorated graphene nanosheets with superior cyclic performance and rate capability, *Nanoscale 5*, 6797-6803.

[170] Li, L., Gao, P., Gai, S., He, F., Chen, Y., Zhang, M., and Yang, P. (2016) Ultra small and highly dispersed Fe3O4 nanoparticles anchored on reduced graphene for supercapacitor application, *Electrochimica Acta 190*, 566-573.

[171] Choi, S. H., and Kang, Y. C. (2014) Fe3O4-decorated hollow graphene balls prepared by spray pyrolysis process for ultrafast and long cycle-life lithium ion batteries, *Carbon 79*, 58-66.

[172] Yu, S., and Chow, G. M. (2004) Carboxyl group (–CO 2 H) functionalized ferrimagnetic iron oxide nanoparticles for potential bio-applications, *Journal of Materials Chemistry 14*, 2781-2786.

[173] Grunlan, J. C., Liu, L., and Regev, O. (2008) Weak polyelectrolyte control of carbon nanotube dispersion in water, *Journal of colloid and interface science 317*, 346-349.

[174] Ditsch, A., Laibinis, P. E., Wang, D. I., and Hatton, T. A. (2005) Controlled clustering and enhanced stability of polymer-coated magnetic nanoparticles, *Langmuir 21*, 6006-6018.

[175] Xiao, J., Tan, Y., Song, Y., and Zheng, Q. (2016) Simultaneous regulation of morphology, crystallization, thermal stability and adsorbability of electrospun polyamide 6 nanofibers via graphene oxide and chemically reduced graphene oxide, *RSC Advances 6*, 41392-41403.

[176] Robin, C., Lorthioir, C., Amiel, C., Fall, A., Ovarlez, G., and Le Cœur, C. (2017) Unexpected rheological behavior of concentrated poly (methacrylic acid) aqueous solutions, *Macromolecules 50*, 700-710.

[177] Zubir, N. A., Yacou, C., Motuzas, J., Zhang, X., and Da Costa, J. C. D. (2014) Structural and functional investigation of graphene oxide–Fe 3 O 4 nanocomposites for the heterogeneous Fenton-like reaction, *Scientific reports 4*, 4594.

[178] Su, J., Cao, M., Ren, L., and Hu, C. (2011) Fe3O4–graphene nanocomposites with improved lithium storage and magnetism properties, *The Journal of Physical Chemistry C 115*, 14469-14477.

[179] Li, X., Huang, X., Liu, D., Wang, X., Song, S., Zhou, L., and Zhang, H. (2011) Synthesis of 3D hierarchical Fe3O4/graphene composites with high lithium storage capacity and for controlled drug delivery, *The Journal of Physical Chemistry C 115*, 21567-21573.

[180] Wu, Z.-S., Yang, S., Sun, Y., Parvez, K., Feng, X., and Müllen, K. (2012) 3D nitrogen-doped graphene aerogel-supported Fe3O4 nanoparticles as efficient electrocatalysts for the oxygen reduction reaction, *Journal of the American Chemical Society 134*, 9082-9085.

Appendix A - Supporting Results

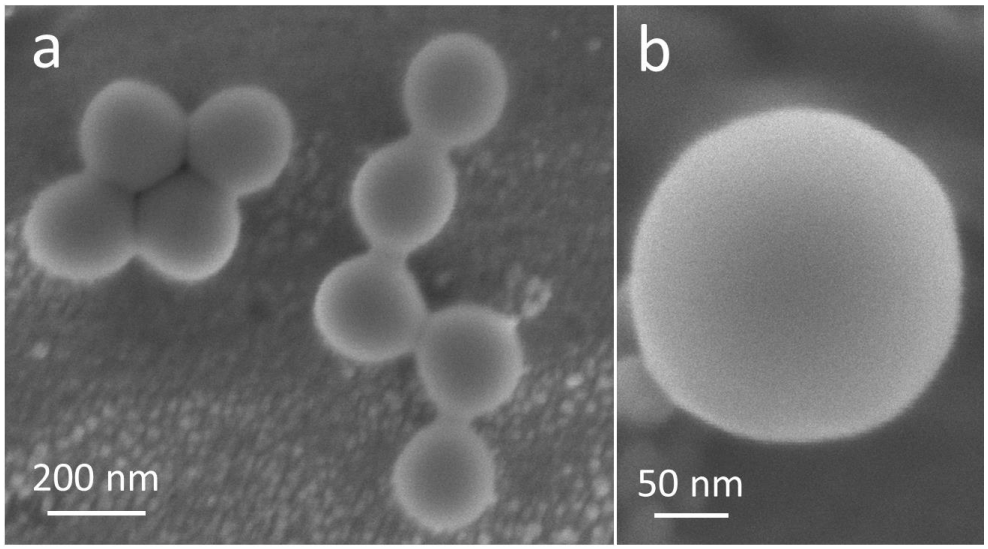

Figure A.1 (a) and (b) SEM images of as-synthesized PS (0.1wt% DVB).

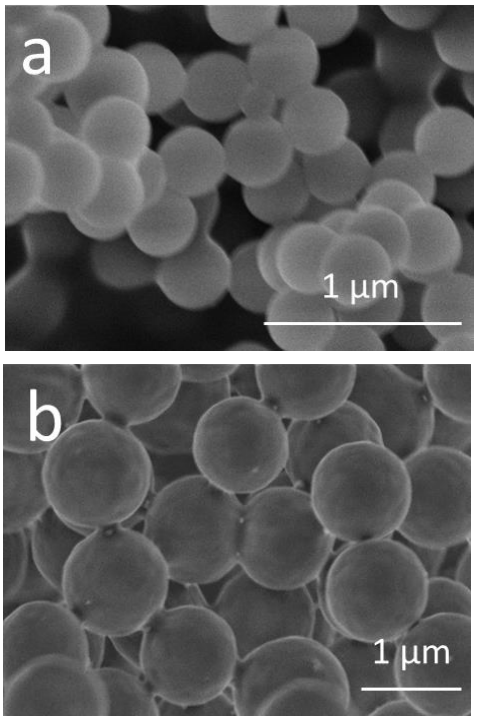

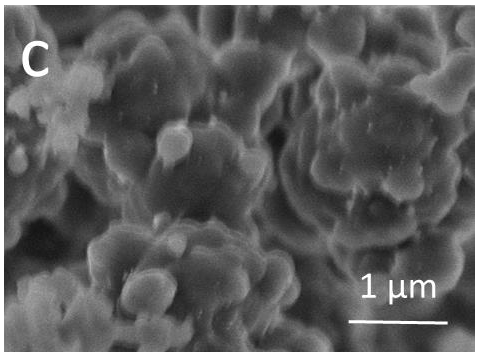

Figure A.2 SEM images of polymer spheres of different sizes adjusted by (a) 0.012, (b) 0.002 and (c) 0.0003 g/ml NaCl, respectively.

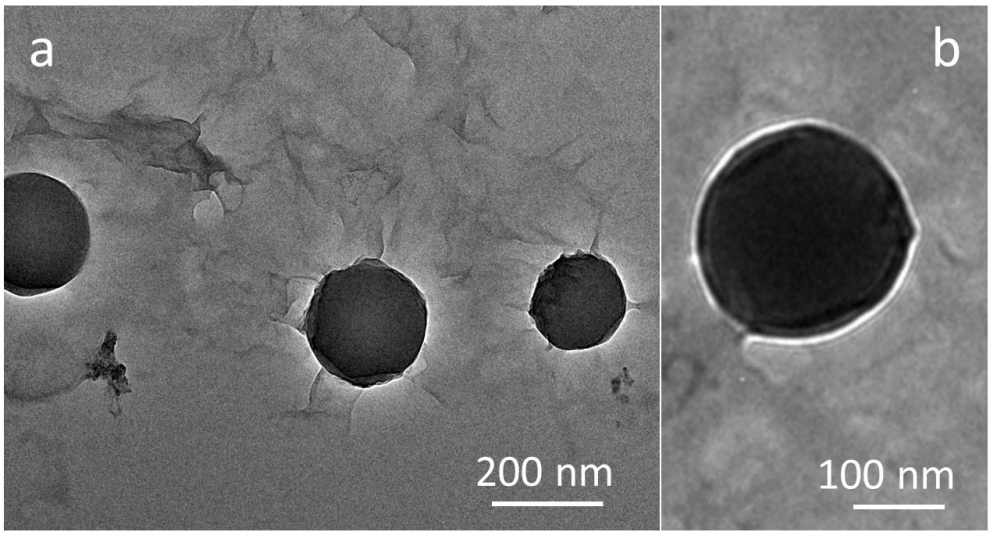

Figure A.3 (a) and (b) TEM images of GO wrapped as-synthesized PS (0.1wt% DVB) with smooth GO surfaces.

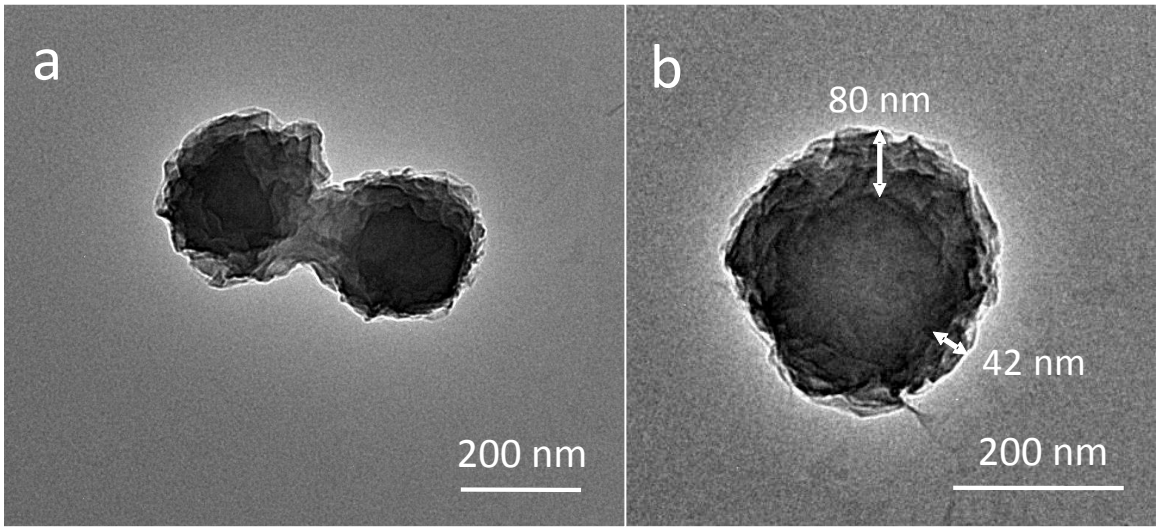

Figure A.4 (a) and (b) TEM images of wrinkled GO@shrunk PS with wrinkled GO surfaces.

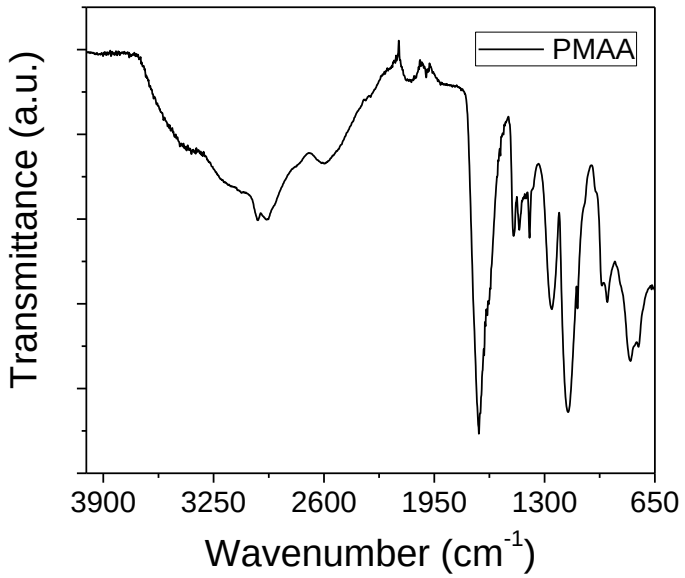

Figure A.5 FTIR spectra of as-synthesized PMAA.

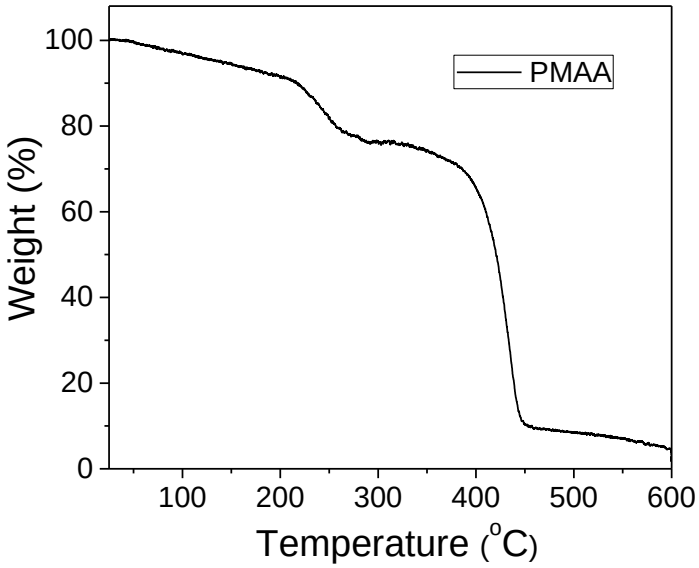

Figure A.6 TGA curve of PMAA under N_2 flow at a temperature ramp of 5 °C min^{-1}.

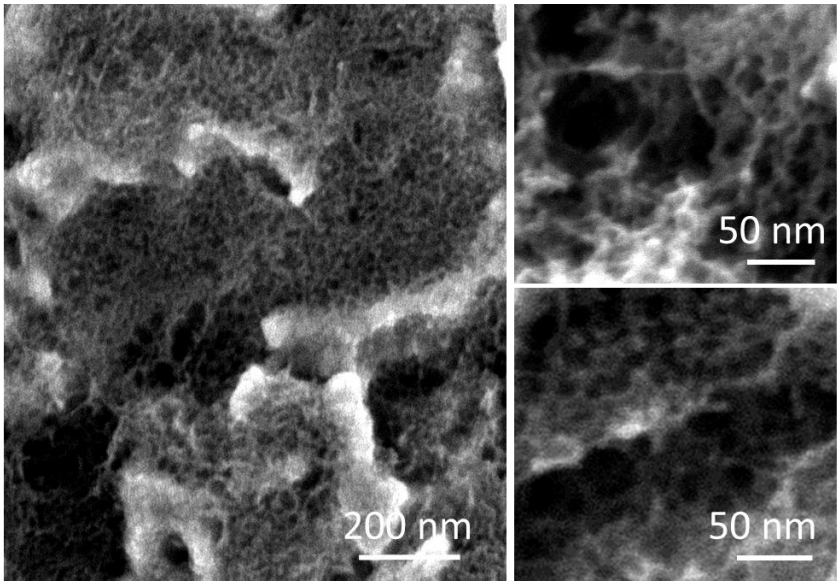

Figure A.7 SEM images of porous Fe_3O_4@RGO anodes.

Table A.1 Comparison of surface area of Fe_3O_4@RGO composites.

Ratio of Fe_3O_4 (wt %)	Surface Area (m^2/g)	Ref.
84	114.5	159
75	262	177
70	221	178
60	52.84	179
46	110	180
60	338.8	This work